EXPERIMENTAL INVESTIGATION OF FIRST- AND SECOND-SOUND SHOCK WAVES IN LIQUID HELIUM II

Thesis by

Jack LeRoy Wise

In Partial Fulfillment of the Requirements

For the Degree of

Doctor of Philosophy

California Institute of Technology

Pasadena, California

1979

(Submitted April 27, 1979)

ACKNOWLEDGMENTS

This project has been supported by the Air Force Office of Scientific Research.

Completion of the work reported in this document has not been achieved on a solely individual basis. To say the very least, I got by with a little help from my friends. I thank all of you.

The support, advice, and patience of Professor Hans W. Liepmann are greatly appreciated. He was right--the equipment really did stop resisting; in fact, some of it went superconducting! I am also indebted to Professor Bradford Sturtevant for his help and suggestions.

The GALCIT staff has contributed significantly to this effort. In particular, Mr. Earl Dahl, with his mechanical skills and good-natured way, has been instrumental in overcoming problems with the experimental apparatus. Mrs. Betty Wood and Mr. Harry Hamaguchi have devoted considerable time to the preparation of the figures for this thesis. Special thanks go to Mrs. Jackie Beard for years of encouragement and, more recently, for her efforts in typing the manuscript.

Dr. Harris Notarys of the Low Temperature Physics group has freely provided invaluable time, assistance, and advice at crucial stages of the research. Thanks, Harris!

A great deal of credit also goes to my parents-in-law, Mr. and Mrs. Walter Pollock, who have helped in many ways--both at home and in the laboratory--to ease the stresses of difficult times.

Finally, I thank my wife, Sandy, for six years of shared toil and, more importantly, for those special moments of laughter and understanding.

EXPERIMENTAL INVESTIGATION OF FIRST- AND SECOND-SOUND SHOCK WAVES IN LIQUID HELIUM II

ABSTRACT

The cryogenic shock tube is used to generate a gasdynamic shock which propagates through saturated helium vapor and subsequently reflects from the upper surface of a column of LHeII. Superconducting thin-film detectors, produced by evaporation of aluminum in an oxygen atmosphere, yield highly repeatable arrival time data for the incident gasdynamic shock and the resultant first- and second-sound shocks in the liquid. Accurate x-t diagrams of the shock trajectories have been constructed for initial liquid temperatures of T_0 = 1.522, 1.665, 1.751, 1.832, 1.989, 2.031, and 2.095°K. Consistent discrepancies are observed between experimental and theoretical wave trajectories.

The detector signals qualitatively verify theoretical predictions that the temperature decreases through the pressure shock and increases through the temperature shock. Amplitude measurements based on static detector calibrations indicate that the magnitude of the temperature jump across the pressure shock agrees approximately with the theoretical calculation. Temperature jump measurements for the coupled second-sound shock imply shock-induced relative velocities, $w = v_n - v_s$, on the order of 2.5 m/sec.

For initial conditions close to the λ-transition (e.g., $T_0 = 2.095^{o}K$), the pressure jump across the first-sound shock is sufficient to cause a change in phase from LHeII to LHeI. This change is experimentally evidenced by detector outputs indicating the absence of the temperature shock in the wake of a sufficiently strong pressure shock.

TABLE OF CONTENTS

TABLE OF CONTENTS (continued)

TABLE OF CONTENTS (continued)

LIST OF TABLES

LIST OF TABLES (continued)

LIST OF FIGURES

LIST OF FIGURES (continued)

I. INTRODUCTION

I.A Theoretical Formulation of Superfluid Hydrodynamics

I.A.1 The Landau Two-Fluid Equations

The structural symmetry, both nuclear and electronic, of the ^{4}He atom results in extremely weak interatomic attractive forces. Consequently, the condensation of helium into the liquid or solid state is possible only at very low temperatures where the disruptive thermal energy is significantly reduced. For temperatures approaching absolute zero, the thermal energy is vanishingly small and the total energy of a system of helium atoms is the sum of the potential energy and the quantum mechanical ground state, or zero-point, energy which is no longer negligible. As a result of the contribution of the zero-point energy, the liquid is the stable phase of ^{4}He for temperatures approaching absolute zero (at pressures not exceeding 25 Atm.). The low temperatures associated with this liquid permit the manifestation of certain quantum effects which have a profound influence on the hydrodynamics.

The phase diagram for ^{4}He is shown in Figure 1. The critical point occurs at $T = 5.20^{\circ}K$ and $p = 2.264$ Atm., and the normal boiling point (for $p = 1$ Atm.) is at $4.21^{\circ}K$. There is no triple point at which gas, liquid, and solid are in equilibrium. The solid can be produced even at the lowest temperatures only by application of pressures in excess of 25 Atm. At lower pressures, the liquid state is preferred.

As indicated by the phase diagram, there are two liquid phases--referred to as liquid helium I (LHeI) and liquid helium II (LHeII). The transition from LHeI to LHeII is called the "λ-transition" and involves no latent heat and no discontinuous change in density. LHeI is a classical fluid which exhibits some properties which are liquid-like and others, such as viscosity and thermal conductivity, which are more gas-like. On the other hand, LHeII exhibits behavior which differs dramatically from that of a classical fluid --behavior which in fact is dominated by macroscopic quantum effects.

To account for the unique behavior of LHeII, a theory known as the two-fluid model has been developed. This theory postulates that LHeII may be viewed as a mixture of two interpenetrating liquids--one being referred to as "superfluid" and the other as "normal fluid". The ^{4}He atom has no net spin, either nuclear or electronic; therefore, Bose-Einstein statistics govern an assembly of ^{4}He atoms, permitting unlimited occupation of any energy level. The superfluid, then, corresponds to that fraction of the liquid which has actually dropped into the ground state, having undergone a Bose-Einstein "condensation" in momentum space (London, 1938a,b). The normal fluid corresponds to particles in excited energy levels. The superfluid has no entropy and its motion is inviscid; the normal fluid has nonvanishing entropy

and exhibits viscous effects.

The hydrodynamic behavior of LHeII on a macroscopic scale is described by the two-fluid equations (Landau, 1941; Landau and Lifshitz, 1959). In this model, the total density of the liquid, ρ, is taken to be the sum of the normal fluid density, ρ_n, and superfluid density, ρ_s:

$$\rho = \rho_s + \rho_n \ .$$

For temperatures approaching absolute zero, $\rho_s/\rho \to 1$; conversely, $\rho_s/\rho \to 0$ at the λ-transition where the liquid reverts completely to normal fluid. The superfluid and normal fluid have separate velocity fields, $\vec{v}_s$ and $\vec{v}_n$, respectively, and their relative velocity is denoted by $\vec{w} = \vec{v}_n - \vec{v}_s$. The two fluids can move relative to one another without exchange of energy or momentum as long as the magnitude of the relative velocity does not exceed a critical value, w_c. The net mass flux (or momentum density) of the liquid is given by

$$\vec{J} = \rho\vec{v} = \rho_s\vec{v}_s + \rho_n\vec{v}_n,$$

where $\vec{v}$ is the effective bulk fluid, or center-of-mass, velocity.

On the basis of the above definitions, and considering only nondissipative processes, the equations of mass, momentum, and entropy conservation are:

MASS $$\frac{\partial \rho}{\partial t} + \nabla \cdot \rho \vec{v} = 0$$

MOMENTUM $$\frac{\partial J_i}{\partial t} + \frac{\partial P_{ij}}{\partial x_j} = 0$$

ENTROPY $$\frac{\partial \rho s}{\partial t} + \nabla \cdot (\rho s \vec{v}_n) = 0$$

where $P_{ij} = p\delta_{ij} + \rho_s v_{s_i} v_{s_j} + \rho_n v_{n_i} v_{n_j}$ = momentum flux

p = pressure

s = entropy/unit mass.

This system of equations is closed by an equation of motion for the superfluid. Landau postulates that the superfluid flow is irrotational ($\nabla \times \vec{v}_s = 0$) and that it is driven by gradients in the chemical potential. The resulting equation of motion for the superfluid is

$$\frac{D\vec{v}_s}{Dt} = \frac{\partial \vec{v}_s}{\partial t} + (\vec{v}_s \cdot \nabla)\vec{v}_s = - \nabla \mu ,$$

or equivalently,

SUPERFLUID $$\frac{\partial \vec{v}_s}{\partial t} + \nabla\left(\frac{v_s^2}{2} + \mu\right) = 0 ,$$

where μ is the chemical potential per unit mass. The above equations are the Landau two-fluid equations. These eight equations in eight independent variables (two thermodynamic variables and six velocity components) yield a complete description of the hydrodynamics for nondissipative processes when supplemented by equations of state for the remaining thermodynamic variables. The state equations are complicated

by the fact that quantities such as ρ, s, and μ are functions of the two independent thermodynamic variables and the relative velocity, $\vec{w}$.

The law of energy conservation is a consequence of the two-fluid equations and is given by

$$\frac{\partial E}{\partial t} + \nabla \cdot \vec{Q} = 0 \ ,$$

where

$$E = E_o + \vec{v}_s \cdot (\vec{J} - \rho \vec{v}_s) + \tfrac{1}{2}\rho v_s^2 = \text{total energy density (kinetic plus internal)}$$

$$E_o = \text{Galilean invariant energy density}$$

$$\vec{Q} = (\mu + \tfrac{1}{2}v_s^2)\vec{J} + \rho s T \vec{v}_n = \rho_n \vec{v}_n (\vec{v}_n \cdot (\vec{v}_n - \vec{v}_s)) = \text{energy flux.}$$

The boundary conditions on the above hydrodynamic equations require that the normal component of $\vec{J}$ and the tangential component of $\vec{v}_n$ must vanish at a solid surface. In addition, the normal component of the heat flux, $\vec{q} = \rho s T \vec{v}_n$, must be continuous across the interface.

I.A.2 Propagation of Sound in Liquid Helium II

Weak disturbances propagate at two characteristic velocities in LHeII. Pressure disturbances, known as "first" sound, travel at the classical isentropic sound speed, which in this case is on the order of 220 m/sec. In addition, weak temperature disturbances, referred to as "second" sound, travel at a separate characteristic velocity which is typically on the order of 0-20 m/sec.

Landau (1941) has theoretically investigated the propagation of sound in LHeII by linearizing the hydrodynamic equations. The equations are linearized by (i) assuming that v and w are small for sound waves, and (ii) considering small perturbations of p, ρ, T, and s about their equilibrium values. By neglecting terms that are quadratic in small quantities, the system of equations for sound waves becomes

$$\frac{\partial \rho}{\partial t} + \nabla \cdot \vec{J} = 0$$

$$\frac{\partial \vec{J}}{\partial t} + \nabla p = 0$$

$$\frac{\partial (\rho s)}{\partial t} + \rho s (\nabla \cdot \vec{v}_n) = 0$$

$$\frac{\partial \vec{v}_s}{\partial t} + \nabla \mu = 0 \ .$$

Making use of the thermodynamic identity $d\mu = -sdT + \frac{1}{\rho}dp$, the linearized equations can be reduced to two wave equations:

$$\frac{\partial^2 \rho}{\partial t^2} = \nabla^2 p$$

$$\frac{\partial^2 s}{\partial t^2} = \frac{\rho_s}{\rho_n} s^2 \nabla^2 T \ .$$

This pair of equations governs the propagation of sound in LHeII, and it follows that there will be two characteristic wave speeds.

Expanding p, ρ, T, and s in terms of equilibrium $()_o$ and perturbation $()'$ quantities yields

$$p = p_o + p' \qquad T = T_o + T'$$

$$\rho = \rho_o + \rho' \qquad s = s_o + s' \ ,$$

and, for small perturbations,

$$s' = \frac{\partial s}{\partial T} T' + \frac{\partial s}{\partial p} p'$$

$$\rho' = \frac{\partial \rho}{\partial T} T' + \frac{\partial \rho}{\partial p} p' \ .$$

Using the above relations, the wave equations may be written as

$$\left(\frac{\partial \rho}{\partial p}\right) \frac{\partial^2 p'}{\partial t^2} + \left(\frac{\partial \rho}{\partial T}\right) \frac{\partial^2 T'}{\partial t^2} = \nabla^2 p'$$

$$\left(\frac{\partial s}{\partial p}\right) \frac{\partial^2 p'}{\partial t^2} + \left(\frac{\partial s}{\partial T}\right) \frac{\partial^2 T'}{\partial t^2} = \frac{\rho_s}{\rho_n} s^2 \nabla^2 T' \ .$$

Assuming a plane wave solution in which p' and T' are proportional to $e^{-i\omega(t-x/C)}$ where C is the wave speed, a nontrivial solution for p' and T' will exist only if the following condition is satisfied:

$$C^4 - C^2 \left[\left(\frac{\partial p}{\partial \rho}\right)_s + \frac{\rho_s}{\rho_n} \frac{s^2 T}{C_v} \right] + \frac{\rho_s}{\rho_n} \frac{s^2 T}{C_v} \left(\frac{\partial p}{\partial \rho}\right)_T = 0 \ ,$$

where C_v is the specific heat per unit mass at constant volume.

In general, $\left(\frac{\partial p}{\partial \rho}\right)_s$ and $\left(\frac{\partial p}{\partial \rho}\right)_T$ are related by the thermodynamic identity

$$\left(\frac{\partial p}{\partial \rho}\right)_s = \frac{C_p}{C_v} \left(\frac{\partial p}{\partial \rho}\right)_T = \gamma \left(\frac{\partial p}{\partial \rho}\right)_T \ ,$$

where C_p is the specific heat per unit mass at constant pressure and $\gamma = C_p/C_v$. By defining the quantities a_{10} and a_{20} as

$$a_{10} = \left(\frac{\partial p}{\partial \rho}\right)_s^{\frac{1}{2}}$$

$$a_{20} = \left(\frac{\rho_s}{\rho_n} \frac{s^2 T}{C_v}\right)^{\frac{1}{2}} ,$$

the condition on the characteristic wave speeds becomes

$$\left(\frac{C^2}{a_{10}^2} - 1\right)\left(\frac{C^2}{a_{20}^2} - 1\right) = 1 - \frac{C_v}{C_p} .$$

For LHeII at low pressures and low temperatures, the specific heats at constant volume and constant pressure are nearly equal, $C_p \doteq C_v$ (e.g. at $T = 1.80^{\circ}K$ and s.v.p., $\gamma = 1.0016$). Under such circumstances the term $(1 - C_v/C_p)$ is negligible, and the two characteristic wave speeds are given by

$$C_{10} = a_{10} = \left(\frac{\partial p}{\partial \rho}\right)_s^{\frac{1}{2}}$$

$$C_{20} = a_{20} = \left(\frac{\rho_s}{\rho_n} \frac{s^2 T}{C_v}\right)^{\frac{1}{2}} .$$

Disturbances propagating with speed C_{10} are referred to as "first" sound and are analogous to ordinary acoustic waves. Disturbances which travel at speed C_{20} are referred to as "second" sound and are unique to LHeII--the expression for C_{20} indicates that $C_{20} \to 0$ at the λ-transition since $\rho_s \to 0$. In Figures 2 and 3, C_{10} and C_{20} are plotted, respectively, as functions of temperature at constant pressure.

As pointed out by Putterman (1974, p.47), the difference between C_p and C_v is not always negligible for LHeII,

particularly for conditions near the λ-transition and at high pressures. For example, at $T = 1.80^{\circ}K$ and $p = 20$ Atm., $\gamma = 1.0935$; at $T = 1.85^{\circ}K$ and $p = 25$ Atm., $\gamma = 1.397$ (Maynard, 1976). In such cases the term $(1 - C_v/C_p)$ must be retained. Keeping terms to first order in $(1 - C_v/C_p)$, the first- and second-sound wave speeds are given by

$$C_{1_0}^2 = a_{1_0}^2 + \frac{a_{1_0}^2 \, a_{2_0}^2}{a_{1_0}^2 - a_{2_0}^2} \left(1 - \frac{C_v}{C_p}\right)$$

$$C_{2_0}^2 = a_{2_0}^2 - \frac{a_{1_0}^2 \, a_{2_0}^2}{a_{1_0}^2 - a_{2_0}^2} \left(1 - \frac{C_v}{C_p}\right) \quad .$$

By recognizing the non-zero difference between C_p and C_v, additional insight into the physical nature of first and second sound may be achieved (Lifshitz, 1944; Landau and Lifshitz, 1959). From the thermodynamic identity

$$1 - \frac{C_v}{C_p} = \frac{C_v T}{C_p^2} \alpha^2 \left(\frac{\partial p}{\partial \rho}\right)_s \quad ,$$

where

$$\alpha = -\frac{1}{\rho}\left(\frac{\partial \rho}{\partial T}\right)_p = \text{thermal expansion coefficient,}$$

it is clear that keeping terms of order $(1 - C_v/C_p)$ is equivalent to keeping terms quadratic in αT. Working only to first order in αT, the following relations are found to apply to a <u>first-sound wave</u>:

$$\vec{v}_n = \vec{v}_s \left[1 + \frac{\alpha T s \rho}{C_h \rho_n} \frac{C_{1_0}^2}{(C_{1_0}^2 - C_{2_0}^2)}\right]$$

$$\Delta p = p' = v(\rho C_{1_0})\left[1 + \mathcal{O}(\alpha T)^2\right]$$

$$\Delta T = T' = v\left[\frac{\alpha T}{C_h}\,\frac{C_{1_0}^3}{(C_{1_0}^2 - C_{2_0}^2)}\right],$$

where $C_h \approx C_p \approx C_v$ since $C_p = C_v\left[1 + \mathcal{O}(\alpha T)^2\right]$. The equivalent relations for a <u>second-sound wave</u> are:

$$\vec{v}_n = -\vec{v}_s\left(\frac{\rho_s}{\rho_n}\right)\left[1 - \frac{\alpha T s}{C_h}\,\frac{p}{\rho_n}\,\frac{C_{1_0}^2}{(C_{1_0}^2 - C_{2_0}^2)}\right]$$

$$\Delta p = p' = -w(\rho_s C_{2_0})\left[\frac{\alpha T s}{C_h}\,\frac{C_{1_0}^2}{(C_{1_0}^2 - C_{2_0}^2)}\right]$$

$$\Delta T = T' = w\left(\frac{\rho_n C_{2_0}}{\rho s}\right)\left[1 + \frac{\alpha T s}{C_h}\,\frac{\rho_s}{\rho_n}\,\frac{C_{1_0}^2}{(C_{1_0}^2 - C_{2_0}^2)}\right].$$

Since αT is small, those quantities which have factors of αT are small compared to those which do not. For a first-sound wave, $\vec{v}_n \doteq \vec{v}_s \doteq \vec{v}$ so the superfluid and normal fluid move together in phase. For a second-sound wave, $\vec{v}_n \doteq -(\rho_s/\rho_n)\,\vec{v}_s$ so the superfluid and normal fluid move out of phase and to lowest order the net mass flux is zero ($\vec{J} = \rho_s\vec{v}_s + \rho_n\vec{v}_n \doteq 0$). First-sound waves are basically pressure disturbances which produce only higher-order temperature changes. On the other hand, second-sound waves are basically temperature disturbances which produce only higher-order pressure changes.

Examination of thermodynamic data reveals that the thermal expansion coefficient, α, of LHeII is negative (e.g. see Maynard, 1976). As a result, for a first-sound

wave the preceding analysis predicts that the temperature will decrease through a compression and increase through a rarefaction; in other words, the pressure and temperature fluctuations have opposite signs for first sound. In the case of a second-sound wave, the pressure and temperature fluctuations have the same sign.

I.A.3 Shock Waves in Liquid Helium II

The theoretical analysis of sound propagation in LHeII has been achieved by considering disturbances for which the induced velocities and perturbations in thermodynamic quantities are small enough to permit linearization of the hydrodynamic equations. For finite-amplitude disturbances, the velocities and changes in thermodynamic quantities are no longer negligible, and the full two-fluid equations must be used. The inherent nonlinearity of these equations results in a variation of wave velocity with amplitude and the subsequent development of shock waves for large amplitudes. Corresponding to the two possible types of weak wave propagation in LHeII, first- and second-sound shock waves may be generated by sufficiently strong disturbances. First-sound shocks produce large changes in pressure and only higher-order temperature changes; second-sound shocks produce large changes in temperature and only higher-order pressure changes.

The propagation of a one-dimensional discontinuity, or shock wave, in LHeII has been examined theoretically by Khalatnikov (1952, 1965). If the velocity, C , of the

discontinuity in the laboratory reference frame is constant, then the analysis is simplified by transforming to a frame of reference moving with the discontinuity (at velocity C in the lab frame). In the shock-fixed, or "steady", coordinates, the equations of mass, momentum, and energy conservation and the equation of motion for the superfluid result in the following set of jump conditions which relate the fluid properties on the two sides (1 and 2) of the shock:

$$\left[\rho v\right]_1^2 = 0$$

$$\left[p + \rho_s v_s^2 + \rho_n v_n^2\right]_1^2 = 0$$

$$\left[\rho s T\, v_n + \rho_n v_n^2 w\right]_1^2 = 0$$

$$\left[\mu + \frac{1}{2} v_s^2\right]_1^2 = 0 \quad .$$

Assuming that the fluid ahead of the shock wave is at rest ($v_n = v_s = 0$) in the laboratory reference frame, transformation of the jump conditions from the shock-fixed back to the lab-fixed reference frame yields

$$\rho_o C = \tilde{\rho}(C-v)$$

$$p_o + \rho_o C^2 = p + \tilde{\rho}(C-v)^2 + \frac{\rho_s \rho_n}{\tilde{\rho}} w^2$$

$$\rho_o s_o T_o C = \tilde{\rho}\tilde{s}T\left[C-v-\frac{\rho_s}{\tilde{\rho}} w\right] - \rho_n w \left[C-v-\frac{\rho_s}{\tilde{\rho}} w\right]^2$$

$$\mu_o + \frac{1}{2} C^2 = \tilde{\mu} + \frac{1}{2} \left[C - v + \frac{\rho_n}{\tilde{\rho}} w \right]^2 ,$$

where the subscripted variables $( )_o$ denote the undisturbed, equilibrium conditions ahead of the shock, and the notation $\tilde{}$ over a quantity indicates that it is a function of p, T, and w.

In principle, the above system of equations may be solved to find the shock velocity, C , and the magnitude of the jumps in the velocities and the thermodynamic variables across the shock. Such a solution is extremely difficult due to the complicated dependence of the thermodynamic variables on the relative velocity, w. However, by considering small discontinuities, Khalatnikov has solved the system of jump conditions by expanding the variables $\tilde{\mu}$, $\tilde{s}$, and $\tilde{\rho}$ to second order in w:

$$\tilde{\mu} (p,T,w) = \mu(p,T) - \frac{\rho_n}{\rho} \frac{w^2}{2}$$

$$\tilde{s} (p,T,w) = s(p,T) + \frac{w^2}{2} \frac{\partial}{\partial T} \left(\frac{\rho_n}{\rho} \right)$$

$$\tilde{\rho} (p,T,w) = \rho(p,T) + \frac{1}{2} \rho^2 w^2 \frac{\partial}{\partial p} \left(\frac{\rho_n}{\rho} \right) .$$

Defining $\Delta p = p - p_o$ and $\Delta T = T - T_o$, the analysis continues by expanding ρ, ρ_n, ρ_s, μ, and s in Taylor's series in Δp and ΔT (up to quadratic terms). Since the coefficient of thermal expansion, α , is small, additional simplification is achieved by neglecting the dependence of the

density, ρ , on the temperature (i.e., assume $\alpha = 0$).

For a first-sound shock wave of strength Δp , Khalatnikov's results show

$$C_1 = C_{10}\left[1 + \frac{\Delta p}{2}\frac{\partial}{\partial p}\ell n\ (\rho C_{10})\right]$$

$$v = \Delta p/\rho C_{10}$$

$$\frac{C_h \Delta T}{C_{10}^2} = O\left[\frac{\Delta p}{\rho C_{10}^2}\right]^3$$

$$\frac{w}{C_{10}} = O\left[\frac{\Delta p}{\rho C_{10}^2}\right]^3 ,$$

where C_1 is the first-sound shock velocity and C_{10} is the first-sound wave speed ahead of the shock. Since the factor $\frac{\partial}{\partial p}\ell n\ (\rho C_{10})$ is on the order of 5×10^{-2} Atm.$^{-1}$ for LHeII, pressure jumps Δp of only several atmospheres can lead to shock Mach numbers, C_1/C_{10}, appreciably greater than unity.

For a second-sound shock wave of strength ΔT , Khalatnikov's results are

$$C_2 = C_{20}\left[1 + \frac{\Delta T}{2}\frac{\partial}{\partial T}\ell n\left(C_{20}^3\frac{\partial s}{\partial T}\right)\right]$$

$$w = \Delta T\left[\frac{\rho}{\rho_n}\frac{s}{C_{20}}\right]$$

$$\frac{\Delta p}{\rho C_{20}^2} = -\frac{w^2}{C_{20}^2}\left[\frac{\rho_s \rho_n}{\rho^2} - \frac{1}{2}\rho C_{20}^2\frac{\partial}{\partial p}\left(\frac{\rho_n}{\rho}\right)\right]$$

and, using the acoustic approximation $\Delta p = \rho C_{10} v$,

$$\frac{v C_{10}}{C_{20}^2} = O\left[\frac{w}{C_{20}}\right]^2 \quad ,$$

where C_2 is the second-sound shock velocity and C_{20} is the second-sound wave speed ahead of the shock. The expression for the second-sound shock velocity may be rewritten as

$$\frac{C_2}{C_{20}} = 1 + \frac{\Delta T}{T}\left[\frac{T}{2}\frac{\partial}{\partial T}\ell n\left(C_{20}^3\frac{\partial s}{\partial T}\right)\right] .$$

Using the thermodynamic identity $\left(\frac{\partial s}{\partial T}\right)_p = \frac{C_h}{T}$ and the definition

$$C_{20}^2 = \frac{\rho_s}{\rho_n}\frac{s^2 T}{C_h} \quad ,$$

the coefficient of $\Delta T/T$ in the above equation may be evaluated as a function of temperature at the saturated vapor pressure using data given by Maynard (1976). The result is shown in Figure 4, and it is immediately apparent that the coefficient $\frac{T}{2}\frac{\partial}{\partial T}\ell n\left(C_{20}^3\frac{\partial s}{\partial T}\right)$ changes sign in the vicinity of $1.88^{\circ}K$. For regions where the coefficient is positive (e.g., $T < 0.5^{\circ}K$ and $0.95 < T < 1.88^{\circ}K$), those parts of a second-sound wave in which ΔT is positive will steepen. However, for regions where the coefficient is negative (e.g., $0.5 < T < 0.95^{\circ}K$ and $1.88 < T < 2.172^{\circ}K$), those parts of a second-sound wave in which ΔT is negative will steepen, and portions with positive ΔT will disperse.

I.B Previous Experimental Investigations of Shock Waves in LHeII

Both first- and second-sound shock waves have been generated and observed experimentally in LHeII. Because of the unique nature of second sound, the majority of experimental attention has historically been devoted to studies of second-sound shocks. However, the characteristics of first-sound shocks are also consequences of the properties of LHeII, and they offer additional insight into the two-fluid hydrodynamics.

As demonstrated by Lifshitz (1944), second sound is most efficiently excited by a nonsteady heat input. Accordingly, second-sound shocks have typically been produced by delivering pulsed electrical power to resistive elements (usually grids of fine wire or thin carbon or metallic films). The coupled first-sound waves produced by this technique are comparatively small in amplitude, and their effects have typically been neglected.

Using power inputs as high as 3.6 watts/cm^2, Osborne (1951) performed the first investigations of finite-amplitude second sound. Signals received by his phosphor bronze resistance thermometer indicated the distortion of pulses of large amplitude, showing the theoretically predicted steepening at either the leading or trailing edge of a pulse (depending on the temperature of the liquid). Dessler and Fairbank (1956) used small marker pulses superimposed on variable amplitude (up to 1.6 watts/cm^2) carrier pulses

to determine the amplitude dependence of the velocity of second sound. Their results showed a linear dependence of the velocity on pulse amplitude for values of $w/C_{20} \lesssim 10^{-2}$, and verified that the coefficient of $\Delta T/T$ in the amplitude-dependent expansion of C_2/C_{20} is $\frac{T}{2}\frac{\partial}{\partial T}\ell n\left(C_{20}^3\frac{\partial s}{\partial T}\right)$, as predicted by Khalatnikov.

Using Schlieren photography, Gulyaev (1967, 1970) observed both the second-sound shock and the coupled first-sound wave produced by a single pulse of Joule heat in a grid of thin strips of constantan ribbon. Gulyaev's experiments, which were conducted at the saturated vapor pressure, indicated that attempts to obtain high-amplitude second sound using heater pulses greater than 3-8 watts/cm^2 may produce boiling at the heater surface, resulting in the formation of a layer of vapor which can modify the shape and intensity of the second-sound wave packet. The Schlieren photographs also revealed aspects of the interaction of first- and second-sound waves with the liquid-vapor interface and the resultant generation of acoustic waves in the vapor.

Cummings, Schmidt, and Wagner (1978) and Rogers (1979) used superconducting, thin-film probes to study the waveform and velocity of second-sound shocks in LHeII at the saturated vapor pressure. In both cases, effects produced by changes in pulse power, pulse duration, and bath temperature were examined. Breakdown of the Khalatnikov linear theory was observed for high power levels ($\gtrsim$ 5-10 watts/cm^2) in the

emitter pulse. Boiling at the surface of the heater was indicated as one possible cause of the breakdown. Rogers suggested that an alternate explanation may be the existence of a limiting critical relative velocity, w_c, on the order of ~ 2.5 m/sec (corresponding to $w_c/C_{20} \approx 0.12$).

Using a somewhat different technique, Cummings (1973, 1976) produced shock waves in LHeII by reflecting a conventionally-generated gasdynamic shock from the saturated vapor-liquid interface. The subsequent increase in both pressure and temperature at the interface resulted in the simultaneous creation of coupled first- and second-sound shocks in the liquid. Arrival time measurements indicated qualitative agreement between observed and theoretically-predicted wave trajectories.

I.C Objectives of the Present Investigation

This research project refines and extends the initial measurements made by Cummings (1973, 1976). The experiment involves an investigation of the flow field produced by a one-dimensional gasdynamic shock which propagates through saturated helium vapor and subsequently reflects from the upper surface of a column of LHeII. The shock reflection results in pressure and temperature jumps at the vapor-liquid interface which generate coupled first- and second-sound shocks in the liquid.

From an analytical standpoint, gaseous helium, including the saturated vapor, is accurately modelled as an ideal gas; consequently, the shock jump relations for the incident and reflected gasdynamic shocks are solved explicitly knowing only the shock Mach number. The well-defined jumps in the gas provide initial conditions for the production of shocks in the liquid. Beginning with the Mach number of the incident gasdynamic shock, wave trajectories in the liquid are computed using the shock jump relations for an ideal gas, the Khalatnikov model for weak shocks in LHeII, and the matching conditions for pressure and velocity at the vapor-liquid interface. The theoretical trajectories are then compared to experimental observations. Such a comparison serves to check the validity of the Khalatnikov model and to reveal effects related to heat- and mass-transfer processes occurring at the vapor-liquid interface.

The present study is designed to produce accurate, repeatable measurements of the wave trajectories (from arrival time data) and estimates of the temperature jumps associated with finite-amplitude first- and second-sound waves. To accomplish this dual purpose, superconducting thin-film gages have been developed and applied to the detection of temperature changes in the shock-induced flow field. The high sensitivity and excellent frequency response of these films yield significant improvements in repeatability of the arrival time data. The thin-film gages also provide expanded measurement capabilities which include observation of additional details of the flow field, sensitive operation in the vicinity of the λ-transition, and implementation of a new level detection scheme. On the basis of static calibrations, the thin-film voltage records permit the estimation of dynamic, wave-related temperature jumps. Such records also provide evidence of a LHeII-LHeI phase transition caused by sufficiently strong first-sound shocks for initial saturation conditions close to the λ-transition.

II. EXPERIMENTAL APPARATUS AND PROCEDURE

II.A Cryogenic Shock Tube

The one-inch diameter cryogenic shock tube, shown in Figure 5, is used to generate the experimental flow field (Liepmann, Cummings, and Rupert, 1973; Cummings, 1973, 1974). The shock tube is mounted vertically with the test section immersed in a cryogenic fluid--in this case LHeII. Helium test gas introduced into the shock tube condenses at the bottom of the test section until the temperature and pressure match the saturation values of the surrounding LHeII bath. This condensation process is permitted to continue until the desired liquid level is achieved in the test section--usually 2-10 cm. After establishing the required test conditions, the driver is clamped against the test section--thereby sealing the test section with the flexible diaphragm (0.001" Mylar). The driver is then rapidly pressurized until the diaphragm bursts as it is forced against the knife-edges.

To enhance the repeatability of run conditions, improved methods of temperature control have been adopted for both the test section and driver of the shock tube. The test temperature (and pressure) are controlled in the usual manner by fixing the saturated vapor pressure of the LHeII bath at the required operating point. In the past, this was accomplished by manually adjusting (and readjusting) valve settings in the vacuum pumping line; however, for the present experiment a condom regulator has been installed to automatically maintain

the desired bath pressure. Using this method, the typical scatter in test temperatures for a set of runs at the same nominal test condition is a few millidegrees.

As in the original work by Cummings, the driver temperature is regulated by a heating tape. Previously, the power input to this heater was controlled manually by adjusting (and readjusting) the supply voltage by means of a variable transformer. For the present experiments, an automatic controller has been designed and used in a closed-loop configuration to maintain the driver wall temperature (as monitored by a glass bead thermistor five inches above the diaphragm) at a constant, specified value--normally 300^{o}K. When the temperature indicated by the monitoring thermistor drops below the specified value, a triac (Motorola, MAC10-4) in series with the heating tape is switched from a blocking to a conducting state, thereby supplying power to the heater.

II.B Instrumentation

II.B.1 Bath Conditions

The saturated vapor pressure of the LHeII bath is measured using an electronic manometer (Datametrics, Type 1014 Barocel; sensor range = 100 mm Hg). The pressure reading is converted to temperature using the 1958 ^{4}He temperature scale.

The liquid level in the bath is determined by a vertical-axis capacitance probe formed by two concentric stainless steel tubes. The total capacitance of the coaxial tubes varies with the liquid depth since the dielectric constants of the vapor and liquid are significantly different. This probe forms one arm of a capacitance bridge that is driven by a low frequency (20 kHz) oscillator. A change in liquid level produces a bridge unbalance voltage which is amplified and rectified, then displayed on a panel meter. The output voltage is a linear function of the liquid depth and, when properly calibrated, provides a continuous, accurate indication of the level. This detection technique eliminates both the heat dissipation and uncertainty characteristic of the formerly-used resistance ladders. Design details of the capacitance probe and the associated electronics are described by Vrba (1971).

II.B.2 Driver and Test Section Initial Conditions

The driver temperature is determined from the resistance of the two wall-mounted thermistors located ¼ inch and 5 inches, respectively, above the diaphragm. These thermistors

are securely embedded in an epoxy coating (Devcon ST) which adheres well to the inner wall of the driver. The driver pressure (at diaphragm burst) is obtained by visual observation of the maximum indicator deflection of a combination pressure-vacuum gage.

The vapor pressure above the condensed LHeII in the test section is measured using a second electronic manometer. The repeatability of test conditions is assured by monitoring the analog voltage output of this manometer with a six-digit voltmeter (Hewlett-Packard, Model 3450A Multi-Function Meter).

II.B.3 Detector Arrays

Wave-related temperature and pressure changes in the shock-induced flow field are sensed by detectors located at different heights above and below the free surface of the condensed liquid in the test section. Two types of temperature-sensitive elements are used. Side-mounted carbon-card detectors are used to measure the arrival of the incident and reflected gasdynamic shocks. Superconducting thin-film gages have been developed to measure either the arrival of the incident shock in the vapor or the arrival of the various finite-amplitude waves in the liquid. In addition, pressure-sensitive piezoceramic gages have been fabricated and are employed to trigger the electronic recording instrumentation following the passage of either the incident gasdynamic shock or the initial first-sound shock.

The design of a piezoceramic gage is illustrated in Figure 6. The sensitive portion of this gage is a 0.010-inch thick piezoceramic disk (Gulton Industries, Inc., G-1408) which is soldered directly to the upper surface of a brass rod. Contact to the opposite electrode of the disk is provided by a soldered copper lead. The upper portion of the assembly is potted in an epoxy casting resin (Emerson & Cuming, Inc., Stycast 2850FT). At cryogenic temperatures, the thermal expansion of this resin has been found to closely match that of brass (Hamilton, Greene, and Davidson, 1968). The resin also offers high thermal conductivity and good thermal shock characteristics. No cracking or debonding of the resin has been observed after repeated cycling to LHeII temperatures.

Details of a carbon-card gage are shown in Figure 7. The sensitive element of this detector is a small strip of carbon card (IRC, 400 ohms per square) which is mounted on the side of a brass tube. Electrical contact is accomplished by means of two 0.001-inch diameter copper leads which are attached to opposite ends of the strip using conducting silver paint. These small leads are in turn attached to larger main leads which pass down the center of the support tube. The upper portion of the completed assembly is potted in the same epoxy casting resin used for the piezoceramic gage.

The superconducting gages consist of granular aluminum films produced by evaporation in an oxygen atmosphere.

Depending on the desired detector geometry, two types of glass substrate have been used. Side-mounted gages, shown in Figure 8, are deposited in the form of a ladder on a section of borosilicate-glass microscope slide. Top-mounted gages, shown in Figure 9, are deposited on the polished tips of tapered, 4-mm diameter pyrex rods. For the side-mounted gages, evaporated copper leads are deposited prior to the granular aluminum films. The leads for the top-mounted gages are strips of fired gold paint (Hanovia Division, Engelhard Industries) on opposite sides of the rod.

The superconducting gages afford major improvements in frequency response and sensitivity over previous shock-tube detectors. Sensitivities as high as 0.1 to 1.0 $V/^{o}K$ and frequency response on the order of 1.0 MHz have been achieved. The high sensitivity of the present gages is evidenced in Figure 10 which shows the voltage drop across a film (at constant current) as a function of temperature. Each curve on this graph represents the superconducting transition for a different value of externally-applied magnetic field. By increasing the magnetic field, the transition is biased to lower temperatures. For a given set of shock tube runs, the external magnetic field is adjusted such that the mid-transition point of the films corresponds to the desired initial test temperature and pressure. For the film calibration shown in Figure 10, the mid-transition sensitivity varies from 0.13 $V/^{o}K$ for the highest transition temperature

to 0.039 V/^{o}K for the lowest transition temperature. Additional details relating to the fabrication and performance of the granular aluminum films are given in Appendix A.

The final installation arrangement for the side-mounted thin-film gages and the associated external biasing magnet are shown in Figure 11. The instrumentation mount is a solid brass bar with tapered leading edge. A nylon false endwall holds the mount vertically in the shock tube. The thin-film substrate fits in a specially-machined recess such that the exposed surface of the substrate is flush with the front face of the mount. A piezoceramic triggering gage is held in a circular pocket on the sloping rear face of the bar. The cross-sectional area of the bar represents a 13% blockage of the test section. The biasing magnet consists of a split pair of coils mounted on a steel yoke. These coils fit snugly around the outside of the test section and are oriented such that the magnetic field vector is perpendicular to the plane of the superconducting films. The coils are each wound with one-half pound (~1000 ft.) of #28 copper wire, and the pair produces a field of 2000 Gauss/Amp.

The installation arrangment for the top-mounted thin-film gages is shown together with the accompanying external biasing solenoid in Figure 12. In all, four superconducting gages are used in conjunction with one piezoceramic triggering gage and one side-mounted carbon-card detector. The overall array represents a blockage of 13% of the cross-

sectional area of the shock tube. During operation, the biasing coil fits concentrically around the lower end of the test section such that the magnetic field vector, as before, is perpendicular to the plane of the superconducting films. The solenoid is wound with ~4000 ft. of #25 copper wire and produces a central field of 500 Gauss/Amp. The coil current is held accurately at the required value by using a six-digit voltmeter (Hewlett-Packard, 3450A) to monitor the voltage drop across a series-connected current shunt.

For both the side-mounted and top-mounted detector arrays, the sensitive elements are located from 2 to 7 cm above the false endwall. The location of each element with respect to the endwall is accurately determined using an optical comparator (Kodak, Model 2A Contour Projector) with a micrometer-driven table capable of determining the position in 10^{-4} inch increments. Repeatability of the measurements indicates a position error with respect to the endwall of 0.10%.

II.B.4 Data Gathering and Analysis

The voltage histories of the carbon-card and thin-film gages during their exposure to the shock-induced flow field are recorded on oscillograms for later analysis. These records are made using a group of dual beam oscilloscopes. The time sweep and vertical amplification of each oscilloscope channel are calibrated before and after a set of shock firings. Voltage amplitudes and arrival time data are obtained from the

oscillograms using a machinist's scale (0.010-inch divisions) in conjunction with a low power (10X) microscope. The measurements are corrected for time sweep and amplification errors.

Estimates of the wave-related temperature jumps are achieved by converting the film voltage to temperature using static calibration curves for the thin-film transitions. These calibration curves of film voltage versus saturation pressure are obtained at the beginning of an experiment using an x-y plotter and the analog output of the test section electronic manometer.

II.C Second-Sound Level-Detection Scheme

The highly sensitive superconducting thin films afford the previously unrealized ability to accurately determine the liquid level in the shock tube prior to actually firing the gasdynamic shock. This new level-detection scheme involves the generation of a second-sound pulse at the endwall and the subsequent measurement of the time-of-flight of the pulse from a submerged superconducting film to the free surface and back to the film. Knowledge of the second-sound wave speed and the height of the detector above the endwall then permits straightforward calculation of the liquid level.

The heating element used for the production of the second-sound pulses is a commercially-available thin metallic film deposited on a 0.032-inch thick fiberglass substrate (Filmohm Corporation). The film resistance drops only a few

percent from its rated value of 50 Ω/square as the test section is cooled from room temperature to liquid helium temperatures. The fiberglass substrate material is easily machined, allowing fabrication of 1-inch disks with clearance holes for the detector mounts. These disks, which are visible in Figures 11 and 12, are cemented to the nylon false endwalls. Electrical leads are attached to the opposite edges of a heating element using indium solder.

Heater power is supplied by a pulse generator (Rutherford Electronics Co., Model B7B). Power dissipation levels in the heater during a pulse are typically 4-5 watts/cm^2, although values have ranged from 2.7 to 16.9 watts/cm^2. The second-sound wave speed used for computing the level is corrected for finite-amplitude effects using data presented by Cummings, Schmidt, and Wagner (1978).

The required time-of-flight measurements are obtained from oscillograms. Figure 13 shows a typical pair of oscilloscope traces produced during a level-detection run. In this case, the free surface of the liquid is 43.6 mm above the endwall; film #3 is 37.8 mm above the endwall; and film #4 is 34.4 mm above the endwall. The passages of the upward-travelling pulse and the returning reflection are clearly evident in each trace.

Agreement between level estimates obtained simultaneously from two separate films implies a position error with respect to the endwall of less than 1.0%.

In the course of applying the above-described level-detection scheme, it has been observed that high-amplitude heater inputs generate both first- and second-sound pulses which are converted to ordinary sound at the vapor-liquid interface. The resultant acoustic pulses are detected in the vapor by a superconducting film. These observations are described more fully in Appendix B.

III. EXPERIMENTAL RESULTS AND DISCUSSION

III.A Detector Response

Initial measurements of shock arrivals in LHeII were made using the side-mounted thin-film gages. As in earlier work by Cummings (1973, 1976), oscillograms of gage voltage histories clearly displayed the arrival of the incident first-sound and second-sound shocks, as well as the arrival of the gas-liquid interface. In addition, the gage response indicated the previously unmeasured arrival of the reflected first-sound shock and re-reflected expansion in LHeII. Unfortunately, the finite width (~0.25 mm) of the side-mounted films resulted in broadening of the risetime associated with second-sound wave fronts to ~10 μsec.

The top-mounted thin-film gages were developed to eliminate the signal broadening and possible boundary layer effects associated with side-mounted gages. Typical output from a top-mounted detector array following the actual firing of a gasdynamic shock is shown in Figures 14 and 15.

The upper traces in Figure 14 show the response of two superconducting gages which were initially above the liquid surface to the passage of the incident gasdynamic shock. Similar traces at faster sweep rates show risetimes less than 0.3 μsec, indicating a thin-film frequency response in excess of 1.0 MHz. The large temperature jump (18-80^{o}K) produced by the incident shock drives the film temperature well above the sensitive transition region, rendering the exposed films

useless for the detection of additional flow field details. As demonstrated by the bottom trace in Figure 14, the less sensitive carbon-card detector responds to the passage of both the incident and reflected gasdynamic shocks.

The oscillograms shown in Figure 15 correspond to the output of two superconducting films initially located below the liquid surface. In Figure 15a, the arrival of the incident first-sound shock at films #3 and #4 is indicated by discontinuities in the respective oscilloscope traces. By simultaneously monitoring the output of films #3 and #4 with a second oscilloscope operated at a reduced sweep rate (100 μsec/div), additional flow field details are recorded in Figure 15b. The film #3 output indicates the sequential arrival of the incident first-sound shock, second-sound shock, reflected first-sound shock, and re-reflected expansion. Film #4, positioned closer to the endwall than film #3, indicates the sequential arrival of the incident first-sound shock, reflected first-sound shock, re-reflected expansion, and second-sound shock. The detector signals qualitatively verify theoretical predictions that the temperature <u>decreases</u> through the first-sound shocks and <u>increases</u> through the second-sound shock and the expansion.

III.B Arrival Time Measurements

III.B.1 x-t Diagrams

The x-t diagram shown in Figure 16 illustrates the trajectories of finite-amplitude waves produced by reflection of the incident gasdynamic shock at the vapor-liquid interface. In this diagram, the position of a wave, x, is plotted as a function of time, t. Wave trajectories are represented by the solid lines; the location of the gas-liquid interface is indicated by the dashed line. The reciprocal slopes of these lines give the corresponding velocities. The origin of the x-t coordinates is defined such that x = 0 is the position of the shock-tube endwall; x = L is the initial liquid depth; and t = T is the arrival time of the incident gas shock (velocity = U_S) at the liquid surface.

Interaction of the incident shock with the liquid surface results in a reflected gasdynamic shock with velocity U_R, and generates two transmitted shocks which propagate into the liquid. One of these transmitted shocks is a first-sound, or pressure, shock with velocity $C_1(0)$; the other is a second-sound, or temperature, shock with velocity $C_2(6)$. Compression of the liquid by the first-sound shock results in a center-of-mass velocity, u_6, which is evidenced by the motion of the gas-liquid interface.

The first-sound shock is reflected from the solid endwall and returns through the liquid with velocity $C_1(6)$. At

the free surface, this wave is re-reflected as an expansion in the liquid (characteristic velocities = $C_1(7) \rightarrow C_1(8')$), and produces a transmitted gasdynamic shock with velocity U_T. The reflected and re-reflected first-sound waves interact with the second-sound shock and produce changes in the center-of-mass velocity.

III.B.2 χ-τ Diagrams

Oscillograms similar to those shown in Figures 14 and 15 are taken at a variety of liquid depths for a fixed incident shock strength and specified initial saturation pressure and temperature. Arrival time measurements obtained from these photographs are then presented on a single wave diagram for each initial saturation state by use of the similarity parameters χ and τ defined as

$$\chi = \frac{L - x}{L}$$

$$\tau = \frac{t - T}{L} \quad (\mu sec/cm),$$

where

x = detector height above endwall (cm)

t = arrival time (μsec)

L = initial liquid depth (cm)

T = arrival time of incident gasdynamic shock at liquid surface (μsec).

Using the pulse technique described earlier, the liquid depth, L, is determined prior to each shock tube firing. The arrival time, T, of the incident shock at the liquid surface is cal-

culated using L and a time-of-flight measurement of either the velocity of the incident gasdynamic shock, U_S, or the velocity of the transmitted first-sound shock, $C_1(0)$.

Accurate (χ,τ) data have been compiled for the following seven initial test temperatures and pressures:

$T_1 = T_0$ (^oK)	$p_1 = p_0$ (Torr)
1.522	4.00
1.665	7.48
1.751	10.4
1.832	13.9
1.989	23.0
2.031	26.0
2.095	31.0

χ-τ diagrams for these cases are shown in Figures 17a-g. Data for all seven cases have been obtained using the top-mounted detector array. Each χ-τ diagram represents arrival time data generated by 43-79 shock tube firings. One firing typically yields data at five discrete values of χ, corresponding to the locations of the four superconducting gages and the single carbon-card detector. Arrival time information at many different values of χ is obtained by varying the liquid depth, L, from one run to the next. Excellent repeatability of the arrival time measurements is evident in each χ-τ diagram.

III.C Wave Velocities

III.C.1 Theoretical Flow Field Analysis

Cummings (1973) outlined a computational procedure which is used in the present work to theoretically predict wave velocities and fluid properties in the different regions of the shock-induced flow field. This one-dimensional model assumes that the gas (including the saturated vapor) exhibits ideal behavior in all flow regions. The measured Mach number of the incident gasdynamic shock is used as input to the computations. Surface evaporation effects, dissipative mechanisms, and changes in liquid temperature are neglected. The first- and second-sound waves are assumed to be uncoupled and noninteracting. The propagation of a first-sound shock is computed using Khalatnikov's finite-amplitude theory. The theoretical velocity of a second-sound shock in a particular region is taken to be the vector sum of the small-amplitude second-sound velocity, corrected for the region pressure, plus the local center-of-mass velocity. Matching conditions applied to the problem require that the pressure and particle velocity be continuous across the gas-liquid interface ($p_5 = p_6$; $u_5 = u_6$).

III.C.2 Experimental Velocity Measurements

Linear, least-squares fits to the arrival time data yield values for the various wave velocities in those instances where sufficient measurements exist. The R.M.S. deviation in

velocities obtained by this scheme is typically on the order of one to two percent for the cases examined. The results of the linear fitting process are shown in Tables 1 and 2a-g where the experimental velocities are compared to theoretical predictions for the seven test cases. Table 2h is a summarized comparison of theoretical and experimental velocities for all seven cases. The theoretical analysis also yields estimates, shown in Tables 3a-g, for the pressure, temperature, and density in the different regions of the flow field.

Referring to Table 1, the Mach number of the incident gas shock ranges from $\bar{M}_S = \bar{U}_S/a_1 = 13.0$ for the case $T_1 = 1.522^oK$, to $\bar{M}_S = 6.23$ for the case $T_1 = 2.031^oK$. The observed incident shock velocities are 2-13% lower than values predicted using the ideal shock tube equation. This discrepancy shows approximate agreement with the experimental results of Cummings (1973) who observed shock velocities in saturated helium vapor which were 8-18% lower than theoretical predictions. Cummings suggested that such non-ideal performance may possibly be related to the finite shock formation distance.

Fluid which has been processed by the incident gasdynamic shock is in region 2 of the flow field. Recalling that the critical pressure for helium is $p_c = 2.25$ Atm., the reduced pressure in region 2, $p_{r_2} = p_2/p_c$, varies from 0.46 to 0.96 for the cases examined. In Figure 18, the compressibility factor, $Z = \frac{p}{\rho RT}$, of cryogenic helium is plotted as a function of temperature for several values of pressure. From this

plot, compressibility effects are clearly negligible for region 2 since the reduced temperature, $T_{r_2} = T_2/T_c$, is much greater than unity--varying from 3.8 to 16. The Reynolds number of the shock-induced flow in region 2 is extremely high--typical values lie between 10^6 and 10^7, based on the test section diameter. The high Reynolds number capabilities of the cryogenic shock tube are discussed in Appendix C, along with other possible techniques of applying cryogenic helium to high Reynolds number research.

Cummings (1973, 1976) reported values for the reflected shock velocity, U_R, which were ~15% larger than those predicted from the observed M_S. As seen in Tables 2a-h, the reflected shock velocity measured in the present experiments is an average of ~19% higher than the theoretical prediction. In fact, experimental values of U_R are an average of 11% larger than ideal values calculated for reflection from a solid endwall ($u_5 = 0$). Measurements of U_R imply an equivalent piston velocity in region 5 on the order of $u_5 = 30$ m/sec in a direction <u>opposite</u> to the apparent interface motion. Considering a typical interface velocity of 10 m/sec, the measurements suggest a discontinuity in particle velocity at the gas-liquid interface of 40 m/sec and a corresponding pressure discontinuity, $\Delta p = p_5 - p_6$, on the order of 1 - 2 Atm.

Although the reduced pressure in region 5 of the flow field is on the order of $p_{r_5} = 2.5 - 5$, compressibility

effects should be negligible in this region since the reduced temperature is on the order of 8 - 36 for the cases examined. However, compressibility effects are undoubtedly significant in the transition zone which separates gas (region 5) from liquid (region 6). In this zone, where the pressure exceeds the critical value and the temperature varies from supercritical values in region 5 to subcritical values in region 6, strongly nonequilibrium processes involving heat- and mass-transfer effects should occur. The nature of the transition zone is perhaps best indicated by the phase diagram shown in Figure 19, which illustrates the calculated fluid states in regions 2, 5, and 6 of the shock-induced flow field. The reduced temperature of the fluid varies through the transition zone from $T_{r_6} \sim 0.4$ on the liquid side to $T_{r_5} \sim 20$ on the gas side. As seen earlier in Figure 18, compressibility effects are important where $T_r \approx 1$.

A possible explanation for strengthening of the reflected gasdynamic shock is mass addition due to vaporization of the liquid. To estimate this effect, assume that all heat which diffuses from the gas into the liquid in the time interval t-T is used to evaporate liquid. Since the heat flux from the gas to the liquid is proportional to $(t-T)^{-\frac{1}{2}}$, the evaporating fluid will act as an advancing piston with velocity proportional to $(t-T)^{-\frac{1}{2}}$. Taking representative values for density, thermal conductivity, and specific heat,

this simplified model yields the following results:

t-T (sec)	Heat Flux (watts/cm^2)	Piston Velocity (m/sec)
10^{-10}	10^4	10^2
10^{-8}	10^3	10
10^{-6}	10^2	1
10^{-4}	10	10^{-1}

In the present experiments, measurements of the reflected shock arrival time have been made for $\tau \simeq 20$ μsec/cm, which corresponds to a characteristic time scale of $(t-T) \simeq 10^{-4}$ second. One-dimensional vaporization effects on this time scale are clearly too small to explain the experimental results for U_R.

Instability of the shock-loaded liquid surface may represent an alternate explanation for a large piston velocity in region 5. Taylor (1950) has investigated the instability of a liquid surface which is given an initial disturbance and subsequently accelerated in a direction perpendicular to its plane. For the present problem, the incident gasdynamic shock accelerates the liquid surface to a final mean velocity of roughly 10 m/sec in a time $t_r \simeq 10^{-9}$ second, where t_r = shock reflection time. Acceleration of the surface is zero before and after the reflection process. Applying Taylor's theory and assuming a worst-case example for which the initial disturbance amplitude is one-tenth the disturbance wavelength, calcu-

lations predict a maximum instability velocity of 5 m/sec relative to the mean surface velocity. This result is within an order of magnitude of the 40-m/sec relative velocity implied by the experimental values of U_R.

Although the reflected gas shock is apparently stronger than expected, measured values of the incident pressure shock velocity, $C_1(0)$, are slightly lower than theoretical estimates based on Khalatnikov's analysis and the observed M_S (see Tables 2a-h). The agreement between experimental and predicted values of $C_1(0)$ is best (within 2%) for the four lowest test temperatures, and is within 5% for all cases. The present experimental values of $C_1(0)$ correspond to a Mach number of $M_1 = C_1(0)/C_{10}(0) = 1.12 - 1.24$.

Sturtevant (1976) has obtained numerical solutions of the full nonlinear two-fluid jump conditions for the case in which the relative velocity, w, upstream of the shock is zero. As in the case of Khalatnikov's analysis, the nonlinear solution also employs standard second-order expansions of thermodynamic variables in terms of w. Considering the incident pressure shock, one may compare results of the nonlinear solution obtained for $T_0 = 1.80^{\circ}K$ with the present experimental results for $T_0 = 1.832^{\circ}K$. On the basis of the strength of the incident gas shock ($M_S = 7.92$), a pressure of $p_5 = p_6 = 7.7$ Atm. is computed. Given this value, the nonlinear solution predicts a pressure shock velocity of $C_1(0) = 250$ m/sec, compared to a predicted velocity $C_1(0) = 275$ m/sec from the Khalatnikov

theory and a measured velocity $C_1(0) = 273$ m/sec. If the measured value of U_R is used in conjunction with the nonlinear solution, values of $p_5 = p_6 = 8.6$ Atm. and $C_1(0) = 253$ m/sec are predicted. To achieve $C_1(0) = 273$ m/sec, the nonlinear solution requires a pressure of $p_6 \doteq 15$ Atm.

Referring to Tables 2a-h, other arrival time measurements in the liquid also indicate velocities which differ from the theoretical predictions. The reflected pressure shock velocity, $C_1(6)$, is always lower than the theoretical value and exhibits decreasing agreement with the theory as the initial test temperature and pressure are increased. The velocity of the leading characteristic of the re-reflected expansion, $C_1(7)$, also tends to be significantly lower than expected. The center-of-mass velocity, u_6, behind the incident first-sound shock is obtained from the arrival time measurements by determining the point of intersection of the reflected first-sound (χ,τ) data with the re-reflected expansion (χ,τ) data. The experimental values of u_6 are 30-58% lower than the theoretical estimates for the cases examined.

Due to the large scatter in his second-sound data, Cummings (1973) was unable to draw reliable conclusions concerning the velocity of the temperature shock. Implementation of superconducting gages in the present experiments has eliminated this problem. Measurements of the temperature shock velocity, $C_2(6)$, are 10-23% lower than theoretical

values. Measured and predicted values of $C_2(6)$ show decreasing agreement as the initial test temperature and pressure are increased. On the basis of earlier assumptions, the shock velocity $C_2(6)$ is given by

$$C_2(6) = C_{20}(p_6, T_6) + u_6 \doteq C_{20}(p_6, T_0) + u_6 \ ;$$

therefore, low experimental values of $C_2(6)$ tend to corroborate the low experimental values of u_6.

Comparisons of the present arrival time data to theoretical predictions are shown graphically in Figures 17a-g where the calculated wave trajectories are plotted together with experimental data. These diagrams clearly depict the trends described above. In the liquid, the arrival times of the interface and the various finite-amplitude waves are later than predicted; in the gas, the arrival time of the reflected shock is earlier than predicted. Agreement between theoretical and experimental arrival times is improved somewhat for the liquid if the measured value of $C_1(0)$ is used as input to the flow field calculations instead of the measured M_S. However, this technique yields estimates for both U_S and U_R which are significantly lower than the measured values.

Another possible reason for the discrepancy between experimental results and theoretical predictions for wave arrival times may be related to geometry effects associated with the detector array. All arrival time data points recorded in Figures 17a-g have been obtained using the top-mounted detector array. However, one experiment has been performed

using the side-mounted detector array at an initial temperature of $T_0 = 1.788^{\circ}K$. Arrival time data from this experiment show exactly the same trend toward late wave arrivals in the liquid. In fact, data from the side-mounted array is virtually indistinguishable from that obtained using the top-mounted array for the case $T_0 = 1.751^{\circ}K$. As mentioned earlier, both the side-mounted and top-mounted detector arrays represent a blockage of 13% of the cross-sectional area of the shock tube. Whitham (1974, pp. 270-272) has theoretically considered the interaction of a shock wave with a finite area change. On the basis of this theory, interaction of the incident gasdynamic shock with a 10% area reduction should result in a 2% increase in U_S and U_R for the cases considered here. This predicted increase is not sufficient to account for the experimentally observed values of U_R which are ~19% higher than expected.

III.D Shock-Induced LHeII-LHeI Phase Transition

The initial condition for each set of (χ,τ) measurements and the state of the liquid subsequent to the passage of each pressure wave are best illustrated by the phase diagram shown in Figure 20. Each run starts with the liquid-vapor system in equilibrium along the saturated vapor curve. The incident pressure shock raises the pressure of the liquid to p_6, the reflected pressure shock increases the pressure still further to $p_7 \doteq 2p_6$, and the re-reflected expansion reduces the pressure to p_8. To lowest order, it is assumed that there is no temperature change across these waves.

For initial conditions close to the λ-transition, it is apparent from the phase diagram that the pressure jump across either the incident pressure shock or reflected pressure shock can be sufficient to cause a change in phase of the liquid from LHeII to LHeI. This predicted change in phase has been experimentally evidenced by detector outputs indicating the absence of a temperature shock in the wake of a sufficiently strong pressure shock. For the cases $T_0 = 1.989$ and $2.031^{\circ}K$, shown in Figures 17e and 17f, temperature shocks have been observed only in region 6 of the flow field. For the case $T_0 = 2.095^{\circ}K$, shown in Figure 17g, the (χ,τ) measurements fail to reveal the existence of a temperature shock in region 6. This result is significant and indicates that a transition from LHeII to LHeI occurs as a result of the passage of the incident pressure shock.

III.E Shock-Induced Temperature Jumps and Relative Velocities

On the basis of static calibrations similar to that shown in Figure 10, the thin-film voltage records permit the estimation of dynamic, wave-related temperature jumps. The resultant values of ΔT may in turn be used to calculate the magnitude of the relative velocity, w.

Experimental temperature-jump and relative-velocity estimates for the incident first-sound shocks are shown in Table 4. Values of ΔT vary from -0.012 to -0.059°K for the cases investigated. These results are within a factor of two of theoretical values for a first-sound wave calculated from the relation

$$\Delta T \doteq \frac{\alpha T}{C_h} u_6 \, C_1(0) = \frac{\alpha T}{\rho C_h} \Delta p$$

(Lifshitz, 1944). The corresponding relative velocity may be expressed to first order in the temperature jump as

$$w = v_n - v_s \doteq \frac{\rho s}{\rho_n C_{10}} \Delta T \; ;$$

thus, the experimental values of ΔT correspond to values of w = -0.09 to -0.44 m/sec for the incident pressure shock.

As seen in Table 5, temperature-jump estimates for the incident second-sound shocks indicate values of ΔT = 0.011 to 0.037°K. In the case of temperature shocks, the relative velocity is given by

$$w = \frac{\rho s}{\rho_n C_{20}} \Delta T$$

(Khalatnikov, 1952, 1965). Thus, the present measurements of ΔT correspond to w = 2-3 m/sec for the temperature shocks. These values of w are very close in magnitude to estimated limiting values of w = 2.5 - 3.8 m/sec which were obtained for the case of temperature shocks produced near S.V.P. by a thin-film heating element (Rogers, 1979). Such values of w are two orders of magnitude larger than those reported for pure counterflow in cylindrical channels (e.g., see Dimotakis, 1974). The heat flux associated with a second-sound wave can be expressed as

$$q = \rho s T v_n = \rho_s s T w \ ;$$

hence, the present estimates of w = 2-3 m/sec correspond to q = 10-30 watts/cm^2.

IV. FUTURE EXPERIMENTS

The cryogenic shock tube has proved to be a useful device for the investigation of low-temperature hydrodynamic phenomena. Observations made during the course of the present experiments suggest several interesting possibilities for further study.

Optical techniques should provide valuable information concerning fluid behavior in the vicinity of the gas-liquid interface following reflection of the incident gasdynamic shock. In particular, spark shadow or schlieren photographs can be used to examine interface properties as well as shock propagation in the gaseous phase, finite-amplitude first- and second-sound waves in LHeII, and wave interactions.

An alternative technique for exploring the nature of a shock-induced LHeII-LHeI phase transition could involve the annihilation of a beam of high-frequency second sound which is generated and sensed by an emitter-detector pair. An arrangement of this type may also prove valuable for measurements of second-sound attenuation in shock-induced counterflow.

Observation of the phase diagram also indicates the possibility of firing gasdynamic shocks of sufficient strength to drive the state of the fluid across the melting line into the solid region from either the LHeII or LHeI region. Experiments of this nature would involve straightforward modification of the present apparatus to achieve somewhat higher values of

driver pressure, p_4, than the present range of 4-5 Atm. For p_6 to exceed the melting pressure, initial estimates indicate required values of p_4 greater than 30 Atm. for $T_0 = T_1 = 2.10^{\circ}K$, or greater than 45 Atm. for $T_0 = 1.65^{\circ}K$. If the reflected pressure shock is instead relied upon to produce values of p_7 that surpass the melting pressure, the minimum requirement for p_4 drops to roughly 10 Atm. Since the pressures and temperatures associated with solid helium are relatively low, liquid helium is a promising candidate for potential studies of shock-induced liquid-solid condensation.

V. CONCLUSIONS

The experimental work reported here demonstrates the development of instrumentation and techniques suitable for making accurate and repeatable measurements of shock arrival times and estimates of wave-related temperature jumps in LHeII.

Arrival time measurements exhibit consistent discrepancies between theoretical predictions and experimental results for u_6 and the wave trajectories. These discrepancies may be related to shortcomings of Khalatnikov's second-order theory or to phenomena associated with the gas-liquid interface. A simplified one-dimensional model for vaporization at the interface fails to account for the observed strength of the reflected gasdynamic shock. Data from the liquid suggest that the propagation velocity and jumps in particle velocity associated with first-sound waves of a specified strength Δp are smaller than those predicted using the Khalatnikov theory. This result is consistent with the observation of reflected gas shocks which are stronger than expected.

Measurements of the temperature jump produced by the incident first-sound shock show approximate agreement with predictions derived from the "acoustic" theory by retaining terms of order αT. Experimental values for the temperature jump across the coupled second-sound shock imply corresponding relative velocities on the order of $w = 2.5$ m/sec.

The present experimental data also indicate that a phase transition from LHeII to LHeI can be produced by sufficiently strong first-sound shocks for initial test conditions close to the λ-transition.

APPENDIX A

SUPERCONDUCTING GRANULAR ALUMINUM FILMS

A.1 Superconducting Bolometers

The electrical resistivity of certain metals, alloys, and compounds vanishes as the temperature is reduced below a "critical" or "transition" temperature, T_c, which has a different characteristic value for each substance. Such materials are referred to as superconductors and are said to be in the superconducting state for temperatures below T_c where their resistivity vanishes. At higher temperatures these materials revert to the "normal" state of nonzero resistivity.

The drop in resistance of a superconductor from the normal value, R_n, to zero actually occurs over a narrow range of temperature. The critical temperature will be defined here as the point where the resistance is $\frac{1}{2} R_n$. Changes in resistance may be observed by monitoring the voltage drop across the superconductor produced by a constant D.C. bias current, I_o. By carefully recording the voltage drop as a function of temperature, the superconductor may be calibrated as a sensitive thermometer. The sensitivity of this thermometer, or bolometer, is given by the slope of a plot of voltage drop, V, versus temperature, T:

$$\frac{dV}{dT} = I_o \frac{dR}{dT} ,$$

where R is the thermometer resistance. The usefulness of

this thermometric technique is generally restricted to the region of the superconducting transition where the resistance is a strong function of temperature.

In recent years, several investigators have employed thin films of various superconductors operated in the region of their superconducting transitions as bolometers for the investigation of hydrodynamic phenomena in LHeII. Notarys (1964) used films of the compound Au_2Bi and layered tin-on-gold films to detect high frequency (up to 25 MHz) second sound. Tin-on-gold films were also employed by Laguna (1975, 1976) for the detection of low amplitude (10^{-8}°K), high frequency (100 kHz - 1.2 MHz) second sound. More recently, Cummings, Schmidt, and Wagner (1978) and Rogers (1979) used the same type of layered film to measure the velocity (from arrival time data) and waveform of second-sound shock waves. Fraser (1969) used granular aluminum films to both generate and detect third sound in helium films adsorbed on a glass substrate. Granular aluminum films were also used by Buchholz, Brandt, and Wiechert (1971) to measure the reflection coefficient of second-sound waves incident on the free surface of LHeII. In the above-mentioned investigations, the restriction of high detector sensitivity to a narrow temperature range was typically overcome by producing magnetic fields strong enough to reduce the transition temperature from its zero-field value to the desired operating point. Sufficiently strong fields were generated either externally or by increasing the bias current through the film.

A.2 Advantages of Granular Aluminum Films

Granular aluminum thin films have been selected for use in the present experiments on the basis of several intrinsic advantages. The bonding of a metal to glass is believed to occur by chemical reaction of the metal with the glass surface (e.g., see Holland, 1970, pp. 98-101). Poor adhesion of gold (a so-called "noble" metal) to glass has been evidenced in the past by occasional detachment of the layered tin-on-gold films from glass substrates. On the other hand, aluminum, which readily forms oxides, reacts strongly with a clean glass surface and adheres very well--a property which is highly desirable in the somewhat hostile shock-tube environment.

The aluminum films derive an additional advantage from their high bulk resistivity which permits fabrication in compact geometries. The normal resistance of a 1250 $\mathring{A}$ tin-on-gold film is approximately $\frac{1}{2}\Omega$/square, corresponding to a resistivity of 6.25 $\mu\Omega$-cm, whereas the normal resistance of a 250 $\mathring{A}$ granular aluminum film is on the order of 10Ω/square, corresponding to a resistivity of $25\mu\Omega$-cm. Thus, for a given film width and thickness, a tin-on-gold film must be roughly four times longer than an aluminum film to achieve the same net resistance.

The sensitivities of the tin-on-gold and granular aluminum films are comparable--characteristic values lie between 0.1 and 1.0V/^{o}K. However, it is of interest to note that

this range of sensitivity is reached in the case of the tin-on-gold films using a bias current of I_o = 1.0 mA (current density = 1.1 x 10^4 A/cm^2), compared to a bias current of 50 μA (current density = 800 A/cm^2) for the granular aluminum films. Considering typical film dimensions, these bias currents lead to power dissipation levels of roughly 5 x 10^{-3} watts/cm^2 for the tin-on-gold films and 2 x 10^{-5} watts/cm^2 for the granular aluminum films. On this basis, local probe heating effects are a factor of 250 lower for the aluminum films.

A.3 Fabrication Procedure for Granular Aluminum Films

Bulk aluminum has a superconducting transition temperature of T_c = 1.2°K, a value which is at the lower end of the temperature regime of interest for most hydrodynamic investigations of LHeII. Fortunately, the transition temperatures of evaporated aluminum films can be "enhanced" (shifted to higher temperatures) by introducing impurities, such as oxygen, during evaporation (Abeles, Cohen, and Cullen, 1966; Cohen and Abeles, 1968). The enhanced transition temperature of a film evaporated in an oxygen atmosphere is a consequence of the formation of small metal grains bounded by metal oxide. The oxide grain boundaries also result in high normal resistivities, high critical magnetic fields, and stabilization of T_c by prevention of grain growth and recrystallization. Grain size and transition temperature are strongly dependent on the oxygen pressure maintained

during evaporation.

Before an evaporation, the substrate is inspected for microscopic scratches and then thoroughly cleaned. The cleaning procedure is a four-step process involving sequential five-minute immersions in ultrasonically-excited baths of chromic-sulfuric acid, distilled water, acetone, and ethyl alcohol. After the final step, the substrate is blown dry using compressed freon.

The 250 Å-thick aluminum films are deposited on the substrate in the form of narrow (0.25-mm wide) strips by evaporating a measured amount of high purity aluminum wire to completion through a mask. The substrate fits snugly against the mask which is mounted 12 cm above the evaporation source. A 0.010-inch thick molybdenum boat (R.D. Mathis Co.) is used as a source. Following installation of the boat, mask, and substrate in the vacuum chamber, the pressure is initially reduced to 5×10^{-6} Torr using a diffusion pump. This step is important since residual gases (such as water vapor) in the system can affect the properties of evaporated films (e.g., see Caswell, 1961a,b).

Next, with the diffusion pump still operating, high-purity oxygen gas is introduced into the system through an inlet valve which is adjusted until the chamber pressure stabilizes at the desired nominal value--generally 0.5 to 4.0×10^{-4} Torr. Oxygen is permitted to flow through the system for several minutes to purge any residual contaminants.

With the oxygen still flowing, the evaporation is then performed by holding the source current at 45 Amps for 30 seconds. Since the aluminum acts as a getter, the oxygen pressure in the chamber drops sharply as evaporation commences. The chamber pressure before and during the evaporation is monitored using a discharge vacuum gage (Consolidated Vacuum Corporation, Type GPH-100A). During the evaporation, the pressure is recorded by an x-y plotter (operated in time-sweep mode) using the analog output of the discharge gage. These plotter records indicate that the pressure drops 50-80% as evaporation starts, then gradually increases while the filament is held at high temperature, and finally returns quickly to the nominal oxygen pressure when the current is shut off.

A.4 Properties of Granular Aluminum Films

A.4.a Edge Effects

The initial sets of thin films produced by the above-discussed procedure exhibited superconducting transition characteristics which were both inconsistent and poorly suited to the intended application. The observed transitions extended over a broad temperature range--indicating low sensitivity--and showed irregular and generally unrepeatable discontinuities and changes in slope which would preclude temperature estimates based on film voltage. In addition, the voltage drop across the films was often marked by fluctuations. These fluctuations attained their maximum

amplitudes in regions of the transition where the mean sensitivity, dV/dT, was highest.

These problems were ultimately found to arise from edge effects associated with the granular aluminum films. Such effects are discussed in the thin-film literature (e.g., see Rose-Innes and Rhoderick, 1978; Strongin, Kammerer, and Paskin, 1965). The edges of films evaporated through a mask are never truly sharp. Instead, they tend to be tapered (i) because the mask is never in perfect contact with the substrate, and (ii) because the hot evaporated atoms wander somewhat on the substrate surface before settling in fixed locations. The critical magnetic field of a thin film is dependent on film thickness--thinner films have higher critical magnetic fields. Superconductivity ceases when the temperature-dependent critical magnetic field is exceeded; therefore, portions of the tapered edge of a film can be superconducting at net bias currents for which the bulk of the film is normal. Thus, the broad transitions displayed by films with edges can be attributed to the distribution of thicknesses in the edge region. Experimentation has demonstrated that removal of the tapered edges of the granular aluminum films results in sharp, smooth, and repeatable transitions. This trimming operation is performed under a microscope using a scribe mounted on a three-axis positioner with micrometer drive. The effects of edge trimming are shown graphically in Figure 21 where the actual transitions

of a particular film are shown for untrimmed, partially-trimmed, and fully-trimmed edges.

A.4.b Oxygen Pressure Effects

As mentioned above, the transition temperature, T_c, depends heavily on the oxygen pressure maintained during evaporation. During the course of the present work, evaporations have been performed at several different oxygen pressures, and records have been kept of the transition temperatures of the resultant films. Figure 22 is a plot of the observed transition temperature at $I_o = 50\mu A$ as a function of the nominal oxygen pressure at the start of evaporation, P_{O_2}. Each point corresponds to the mean transition temperature for a group of films (typically 5) which were deposited simultaneously. The "error" bars indicate the range of actual transition temperatures within a particular group. Higher transition temperatures are clearly a consequence of higher oxygen pressures--a result which agrees with the observations of Cohen and Abeles (1968). The scatter of transition temperatures within individual groups is small enough ($\sim 20 \times 10^{-3}{}^{o}K$) to guarantee that all films can be simultaneously biased for nearly mid-transition operation at a given shock-tube test temperature.

A.4.c Magnetic Field Biasing

For the representative film calibration shown earlier in Figure 10, magnetic field biasing is seen to result in a broadening of the superconducting transitions. The bolometer

sensitivity for a given bias current, I_o, is thus considerably degraded for higher field strengths. If necessary, the initial sensitivity can be regained by increasing the bias current. However, this increase is limited to values less than a maximum current at which the transition becomes unstable as different regions of the film spontaneously undergo transitions at slightly different temperatures--resulting in a "staircase" transition.

The critical magnetic field strength perpendicular to the plane of the films, $H_{c_\perp}$, is plotted as a function of the experimentally measured shift in transition temperature, $\bar{T}_c - T$, in Figure 23 where data are shown for three groups of films. Each group has a different mean critical temperature, $\bar{T}_c$. The bulk of the data shown is for films #11-15 ($\bar{T}_c = 1.879^oK$), and a linear fit to the data indicates a slope of 961 Gauss/^oK. Linear fits on the limited data for films #6-9 ($\bar{T}_c = 2.108^oK$) and films #16-20 ($\bar{T}_c = 1.645^oK$) indicate slopes of 1460 Gauss/^oK and 579 Gauss/^oK, respectively. As expected, films with higher critical temperatures require larger magnetic fields for biasing.

In actuality, the dependence of the critical magnetic field on temperature is better approximated by parabolas of the form

$$H_{c_\perp} = H_{o_\perp}\left[1 - \left(\frac{T}{\bar{T}_c}\right)^2\right] ,$$

where $H_{o_\perp}$ is the critical field at absolute zero. Knowing the characteristic values of $H_{o_\perp}$ and T_c for a particular superconductor, the critical field can be calculated at a given temperature. Conversely, if T_c is known together with values of $H_{c_\perp}$ at different temperatures, then $H_{o_\perp}$ can be estimated by fitting the parabolic relation to the data. This procedure has been followed using the same data shown in Figure 23. The results are shown in Figure 24 where the value of $H_{o_\perp}$ for each group of films is plotted as a function of the nominal oxygen pressure, P_{O_2}, at the start of the vacuum deposition of that group. The available data indicate a fairly linear relation for $H_{o_\perp} = H_{o_\perp}(P_{O_2})$.

A.4.d Sensitivity

The zero-field mid-transition sensitivity of the present top-mounted films at the standard experimental bias current of 50μA ranges from 0.1 to 1.0V/^{o}K. Sensitivities as high as 8V/^{o}K have been attained using the longer side-mounted films.

APPENDIX B

CONVERSION OF HEATER-GENERATED FIRST- AND SECOND-SOUND PULSES AT A LIQUID-VAPOR INTERFACE

Both first- and second-sound waves incident on a liquid-vapor interface yield ordinary acoustic waves in the vapor. The reflection and conversion of first sound may be viewed in terms of classical acoustic theory. On the other hand, second-sound pulses cause fluctuations in temperature at the liquid surface, resulting in enhanced vapor emission and the subsequent production of ordinary sound.

Acoustic waves generated in saturated helium vapor by incident second sound have been experimentally detected by a number of observers using either microphones or resistance thermometers (e.g., see Lane, Fairbank, and Fairbank, 1947; Pellam, 1948, 1949; Hunter and Osborne, 1969). Pellam (1948, 1949) and Hofmann, Keck, and Schubert (1970) have also employed microphones to investigate first sound which was initiated in the liquid by heater pulses on the order of 10-100 mW/cm^2. Using optical techniques, Gulyaev (1970) also observed heater-generated first- and second-sound pulses in LHeII, as well as the conversion of these pulses to ordinary sound at the liquid surface.

In the present experiment, superconducting thin-film detectors are used to sense the passage of heater-generated first- and second-sound waves in the liquid and the coupled acoustic waves in the vapor. The top-mounted detector array

(Figure 12) is used for these measurements. The nominal operating point is $T_0 = 2.031^{\circ}K$, corresponding to a saturated vapor pressure of 26 Torr. Under these conditions, the small-amplitude first- and second-sound velocities are 225 and 15.6 m/sec, respectively, and the acoustic velocity in the vapor is 84 m/sec. Power dissipation in the heater is 16.9 watts/cm^2 during the $\sim$40-μsec pulses.

Trajectories of the waves produced by a single heater pulse are best illustrated by the χ-τ diagram shown in Figure 25. The normalized coordinates of this diagram are identical to those described in the text (e.g., see section III. B. 2). The heater (located at $\chi = 1.0$) is pulsed at "time" $\tau = 0$ to produce a first-sound wave (velocity = C_1) and a second-sound wave (velocity = C_2). Since $C_1 \doteq 14.4C_2$, the first-sound pulse completes seven round trips from the heater to the liquid surface ($\chi = 0$) and back to the heater before the second-sound pulse reaches the interface. An acoustic wave (velocity = a_1) is created in the vapor each time a first- or second-sound wave reflects from the interface.

Experimental evidence for this process is given by the oscillograms shown in Figure 26. The liquid level is successively lower for the three runs 85, 103, and 117. For run 85, film 1 is 3.0 mm <u>above</u> the free surface and film 4 is 5.4 mm <u>below</u> the surface. The film 4 output clearly shows the arrival of both the upward-travelling and reflected sec-

ond-sound wave. Careful examination of the film 4 trace also shows small-amplitude precursor signals corresponding to the multiply-reflected first-sound wave. The film 1 output for run 85 shows the passage of seven acoustic waves in the vapor produced by multiple reflection of the first-sound pulse, followed by a larger acoustic pulse produced by arrival of the second-sound wave at the liquid surface. All wave arrival times agree with values predicted from Figure 25.

For run 103, both films are above the liquid surface, and the traces are similar. For run 117, the films are even farther above the liquid surface, and the traces appear to be "compressed" in time since the liquid occupies a much smaller fraction of the distance from the heater to the detecting elements.

From these oscillograms, it is apparent that signals corresponding to ordinary sound pulses in the vapor are comparable in magnitude regardless of whether they were produced by reflection of a first- or a second-sound wave at the liquid-vapor interface. Furthermore, the amplitude of signals received in the vapor is comparable to that indicated for the second-sound pulse in the liquid. For the case of ordinary sound generated by second-sound reflection at the interface, Pellam (1949) and Osborne (1962) have also noted that the temperature jump associated with the transmitted ordinary sound is similar in amplitude to the jump produced in the liquid by the incident second-sound pulse. The large

strength implied for the heater-generated first-sound waves in the present experiment is probably due to vaporization at the heating element since the power dissipation level exceeds typical values quoted for the initiation of boiling (e.g., see Broadwell and Liepmann, 1969; Gulyaev, 1970). Estimation of the true temperature discontinuity associated with the acoustic waves in the vapor is complicated by the saturated helium film (thickness $\approx$ 200 Å) which covers detectors located above the vapor-liquid interface.

APPENDIX C

NOTES ON THE APPLICATION OF CRYOGENIC HELIUM TO HIGH REYNOLDS NUMBER RESEARCH

The Reynolds number, Re, is a measure of the relative magnitude of inertia and viscous forces in a given flow situation. This dimensionless parameter is defined by the relation

$$Re = \frac{\rho u d}{\mu} = \frac{\rho a M d}{\mu} \quad ,$$

where

ρ = fluid density

a = sound speed

M = Mach number

d = characteristic length

μ = viscosity .

Changes in pressure and temperature influence the Reynolds number to the extent that the characteristic values of ρ, a, and μ are altered. For a gas, a and μ are independent of pressure to first order, whereas ρ is directly proportional to pressure. Consequently, increases in pressure can be used to increase the Reynolds number. On the other hand, ρ, a, and μ are all heavily dependent on the temperature, T :

$$\rho \propto T^{-1}$$

$$a \propto T^{\frac{1}{2}}$$

$$\mu \propto T^{\omega}, \quad \tfrac{1}{2} < \omega < 1 \ .$$

From these considerations, for given values of M and d, the dependence of Re on temperature is given by

$$Re \propto T^{-(\frac{1}{2}+\omega)} \quad .$$

Thus, the Reynolds number is clearly increased by operating at substantially reduced temperatures. Two types of cryogenic test facilities may be considered for high Reynolds number investigations: short-duration, blow-down devices (e.g., shock tube or Ludweig tube); or continuous, closed-cycle tunnels.

In the case of the cryogenic shock tube, a high Reynolds number flow is produced by passage of the incident gasdynamic shock through initially undisturbed test gas. Letting subscripts '1' and '2', respectively, denote conditions in the regions ahead of and behind the propagating shock, the Reynolds number of the shock-induced flow in region 2 may be written as

$$Re = \frac{\rho_2 u_2 d}{\mu_2} = \frac{\gamma d p_1}{a_1 \mu_2} \frac{\left(\frac{u_2}{a_1}\right)\left(\frac{p_2}{p_1}\right)}{\left(\frac{T_2}{T_1}\right)} \quad ,$$

where

$$p = \rho RT$$

$$\gamma = C_p/C_v$$

$$d = \text{test section diameter.}$$

The ratios u_2/a_1, p_2/p_1, and T_2/T_1 are easily computed in terms of the shock Mach number, M_S. The viscosity, μ_2, is determined from the calculated properties in region 2

using tabulated thermodynamic data (e.g., see McCarty, 1972). In experiments performed to date, M_S has been varied by changing the test pressure, p_1, while maintaining constant values of p_4 (driver pressure), T_4 (driver temperature), and T_1. Using the ideal shock tube equation and assuming that the driver and test gases are the same, Re_2 is given by

$$Re_2 = f(M_S, T_1, T_4, p_4, \gamma) .$$

The above relation can be used to plot Re_2 as a function of M_S for given values of T_1, T_4, p_4, and γ. This method has been used to construct Figure 27 for the cryogenic shock tube with helium driver and test gases. The solid lines represent ideal shock tube performance based on the experimentally measured values of T_1, T_4, and p_4. Data points are shown to indicate experimental values of M_S and the corresponding values computed for Re_2. As the test temperature is reduced, shock-tube performance approaches the ideal calculation. Lower test temperatures dramatically increase the range of available Reynolds numbers and shock Mach numbers. For low initial test pressure, values of $M_S = 40$ have been obtained; for high initial test pressure, values of $Re_2 = 10^6$-10^7 per inch are achieved.

An alternative approach to high Reynolds number research with cryogenic helium may involve the construction of a closed-circuit tunnel as shown in Figure 28. The working fluid may be either gaseous or liquid helium. The potential

capabilities of this technique are best revealed by an illustrative cycle analysis. Assume that the desired conditions in the test section (1) are given by

$$\left.\begin{aligned} p_1 &= 1 \text{ Atm.} \\ T_1 &= 3^{\circ}K \end{aligned}\right\} \longrightarrow \text{liquid helium}$$

$$M_1 = 1.4 \quad .$$

The test section Reynolds number based on these specifications is 10^8 per cm. A working cycle designed to achieve these requirements is shown on the h-s diagram (enthalpy vs entropy) shown in Figure 29. The fluid undergoes isentropic expansion from the stagnation chamber (0) to the test section (1); hence, $s_0 = s_1$. For the present example, it is assumed that the fluid passes through a normal shock at the diffuser entrance (2'). The overall flow of the fluid from the stagnation chamber to the end of the diffuser (2) may be viewed as an adiabatic throttling (Joule-Thomson) process; thus, $h_2 = h_0$. The diffuser is followed by an isentropic compression (process 2-3) for which $s_2 = s_3$. Finally, the fluid is returned to the initial stagnation state by passage through an isobaric heat exchanger ($p_0 = p_3$).

Similar cycle calculations have been performed assuming test section conditions with helium at pressures exceeding the critical pressure. Reynolds number capabilities comparable to the above-quoted figure of 10^8 per cm are predicted.

The investigation of high Reynolds number flows is closely related to turbulence research. All flows are

turbulent at sufficiently high Reynolds numbers. The largest scales of turbulent motion are set by the characteristic dimensions of the experimental apparatus. The smallest scale of turbulent motion is the Kolmogorov microscale, η , which is given by

$$\eta = \left(\frac{\nu^3}{\varepsilon}\right)^{\frac{1}{4}}$$

where $\nu = \frac{\mu}{\rho}$ = kinematic viscosity

ε = dissipation rate (per unit mass).

By relating the dissipation rate to the length and velocity scales of the large-scale turbulence, one obtains

$$\varepsilon \sim \frac{\bar{u}^3}{d}$$

where $\bar{u}$ = mean velocity

d = characteristic test section dimension .

Thus, the ratio of the smallest to the largest turbulent length scales may be written as

$$\frac{\eta}{L} \sim \left(\frac{\nu^3}{\bar{u}^3 L^3}\right)^{\frac{1}{4}} = Re^{-3/4} .$$

The separation between the limiting scales of turbulent motion clearly increases for increasing Reynolds number. By assuming a characteristic test section dimension of 1 cm and taking the nominal test conditions considered earlier for a closed-circuit LHe tunnel (p_1 = 1 Atm, T_1 = 3°K, M_1 = 1.4), the corresponding Kolmogorov microscale is on the order of

100 Å. This value is a factor of 10^6 times smaller than the overall flow dimensions.

From simple dimensional considerations, the power required to operate a tunnel cycle is given by

$$P_{req'd} = \frac{\pi}{8} Re^2 M \frac{\mu^2 a}{\rho} ,$$

where all quantities are evaluated at the test section conditions. Assuming a test section diameter of 3.6 cm, the power required for the illustrative LHe cycle discussed earlier is 2.2 MW (3000 H.P.). It is interesting to compare this value to that required for the National Transonic Facility (N.T.F.) which will employ cryogenic nitrogen as a working fluid. Assuming test section conditions of M = 1.4, p = 1 Atm, and T = 100°K, the N.T.F. will achieve a Reynolds number of 10^8 per meter at a power input of 200 MW (260,000 H.P.). Thus, from a power requirement standpoint, the advantages of cryogenic helium as a working fluid are obvious.

This brief discussion indicates the great potential advantages to be derived from the application of cryogenic helium to high Reynolds number studies. Helium is also a promising candidate for the investigation of flow-induced critical-point phenomena, high shock Mach numbers (without ionization effects), and even supersonic liquid flow.

REFERENCES

1. Abeles, B., Cohen, R.W., and Cullen, G.W. 1966 Phys. Ref. Letters 17, 632.

2. Broadwell, J.E., and Liepmann, H.W. 1969 Phys. Fluids 12, 1533.

3. Buchholz, F.I., Brandt, D., and Wiechert, H. 1971 Phys. Letters 35A, 471.

4. Caswell, H.L. 1961a J. App. Phys. 32, 105.

5. Caswell, H.L. 1961b J. App. Phys. 32, 2641.

6. Cohen, R.W., and Abeles, B. 1968 Phys. Rev. 168, 444.

7. Cummings, J.C. 1973 Ph.D. Thesis, Calif. Inst. of Tech.

8. Cummings, J.C. 1974 J. Fluid Mech. 66, 177.

9. Cummings, J.C. 1976 J. Fluid Mech. 75, 373.

10. Cummings, J.C., Schmidt, D.W., and Wagner, W.J. 1978 Phys. Fluids 21, 713.

11. Dessler, A.J., and Fairbank, W.M. 1956 Phys. Rev. 104,6.

12. Dimotakis, P.E. 1974 Phys. Rev. A 10, 1721.

13. Fraser, J.C. 1969 Ph.D. Thesis, U.C.L.A.

14. Gulyaev, A.I. 1967 JETP Letters 5, 325.

15. Gulyaev, A.I. 1970 Sov. Phys. JETP 30, 34.

16. Hamilton, W.O., Greene, D.B., and Davidson, D.E. 1968 Rev. Sci. Inst. 39, 645.

17. Hofmann, A., Keck, K., and Schubert, G.U. 1970 Z.Physik 231, 177.

18. Holland, L. 1970 Vacuum Deposition of Thin Films, Chapman and Hall, London.

19. Hunter, G.H., and Osborne, D.V. 1969 J. Phys. C (Solid St. Phys.) 2, 2414.

20. Khalatnikov, I.M. 1952 Zh. Eksp. Theor. Fiz. 23, 253.

REFERENCES (continued)

21. Khalatnikov, I.M. 1965 Introduction to the Theory of Superfluidity, Benjamin, New York.

22. Laguna, G.A. 1975 Ph.D. Thesis, Calif. Inst. of Tech.

23. Laguna, G.A. 1976 Cryogenics 16, 241.

24. Landau, L. 1941 J. Phys. U.S.S.R. 5, 71.

25. Landau, L.D., and Lifshitz, E.M. 1959 Fluid Mechanics, Pergamon, London.

26. Lane, C.T., Fairbank, H.A., and Fairbank, W.A. 1947 Phys. Rev. 71, 600.

27. Liepmann, H.W., Cummings, J.C., and Rupert, V.C. 1973 Phys. Fluids 16, 332.

28. Lifshitz, E. 1944 J. Phys. U.S.S.R. 8, 110.

29. London, F. 1938a Nature 141, 643.

30. London, F. 1938b Phys. Rev. 54, 947.

31. Maynard, J. 1976 Phys. Rev. B 14, 3368.

32. McCarty, R.D. 1972 NBS-TN-631.

33. Notarys, H.A. 1964 Ph.D. Thesis, Calif. Inst. of Tech.

34. Osborne, D.V. 1951 Proc. Phys. Soc. Lond. 64, 114.

35. Osborne, D.V. 1962 Proc. Phys. Soc. Lond. 80, 103.

36. Pellam, J.R. 1948 Phys. Rev. 74, 841.

37. Pellam, J.R. 1949 Phys. Rev. 75, 1183.

38. Putterman, S.J. 1974 Superfluid Hydrodynamics, North-Holland, Amsterdam.

39. Rogers, P.L. 1979 A.E. Thesis, Calif. Inst. of Tech.

40. Rose-Innes, A.C., and Rhoderick, E.H. 1978 Introduction to Superconductivity, 2nd Ed., Pergamon, New York.

REFERENCES (continued)

41. Strongin, M., Kammerer, O.F., and Paskin, A. 1965 Phys. Rev. Letters 14, 949.

42. Sturtevant, B. 1976 Bul. Amer. Phys. Soc. 21, 1223.

43. Taylor, G. 1950 Proc. Roy. Soc. Lond. 201, 192.

44. Vrba, J. 1971 Cryogenics 11, 313.

45. Whitham, G.B. 1974 Linear and Nonlinear Waves, John Wiley & Sons, New York.

Table 1. Incident Gasdynamic Shock Velocity

p_1 (Torr)	T_1 (^oK)	$\frac{p_4}{p_1}$	Number of (χ,τ) Points	Experimental $\bar{U}_S$ (m/sec)	R.M.S. Deviation (m/sec)	$\frac{\bar{U}_{S_{exp't}}}{U_{S_{ideal}}}$	$\bar{M}_{S_{exp't}}$
4.00	1.522	843	54	940.	7.	.98	13.0
7.48	1.665	396	53	697.	10.	.88	9.17
10.4	1.751	345	27	670.	24.	.87	8.60
13.9	1.832	234	102	631.	7.	.92	7.92
23.0	1.989	140	55	540.	6.	.91	6.50
26.0	2.031	119	56	523.	3.	.92	6.23
31.0	2.095	114	58	556.	8.	.98	6.52

Table 2a. Comparison of Experimental & Theoretical Velocities

$T_1 = T_0 = 1.522^{\circ}K$

$p_1 = p_0 = 4.00$ Torr

$M_S = 13.0$

Velocity	Number of (χ,τ) Points	Experimental Value (m/sec)	R.M.S. Deviation (m/sec)	Theoretical Value (m/sec)	$\frac{(\ )_{exp't}}{(\ )_{theory}}$
U_R	22	542.	17.	455.	1.19
$C_1(0)$	134	269.	0.4	271.	.99
$C_1(6)$	109	276.	1.4	312.	.89
$C_1(7)$	107	267.	3.4	319.	.84
$C_2(6)$	36	31.2	0.3	34.8	.90
$C_2(7)$	2	22.5	---	17.2	1.31
$C_2(8)$	11	13.3	0.9	3.5	3.76
$u_5 = u_6$	---	10.6	---	16.2	.66
$C_2(6) - u_6$	---	20.6	---	18.6	1.11

Table 2b. Comparison of Experimental & Theoretical Velocities

$T_1 = T_0 = 1.665^{o}K$

$p_1 = p_0 = 7.48$ Torr

$M_S = 9.17$

Velocity	Number of (χ,τ) Points	Experimental Value (m/sec)	R.M.S. Deviation (m/sec)	Theoretical Value (m/sec)	$\frac{(\ )_{exp't}}{(\ )_{theory}}$
U_R	15	353.	6.4	336.	1.05
$C_1(0)$	217	261.	0.9	266.	.98
$C_1(6)$	170	276.	2.6	305.	.91
$C_1(7)$	139	262.	4.6	311.	.84
$C_2(6)$	65	27.7	0.3	33.8	.82
$C_2(7)$	8	21.5	14.	17.1	1.26
$C_2(8)$	16	14.4	0.8	5.00	2.89
$u_5 = u_6$	---	8.6	---	15.0	.57
$C_2(6) - u_6$	---	19.1	---	18.8	1.02

Table 2c. Comparison of Experimental & Theoretical Velocities

$T_1 = T_0 = 1.751^{o}K$

$p_1 = p_0 = 10.4$ Torr

$M_S = 8.60$

Velocity	Number of (χ,τ) Points	Experimental Value (m/sec)	R.M.S. Deviation (m/sec)	Theoretical Value (m/sec)	$\frac{(\ )_{exp't}}{(\ )_{theory}}$
U_R	23	424.	14.	319.	1.33
$C_1(0)$	145	270.	1.0	272.	.99
$C_1(6)$	124	273.	2.6	316.	.86
$C_1(7)$	117	276.	4.1	322.	.86
$C_2(6)$	44	30.0	0.4	35.8	.84
$C_2(7)$	5	---	---	15.4	---
$C_2(8)$	8	13.8	3.4	1.96	7.04
$u_5 = u_6$	---	12.3	---	17.7	.70
$C_2(6) - u_6$	---	17.7	---	18.1	.98

Table 2d. Comparison of Experimental & Theoretical Velocities

$T_1 = T_0 = 1.832^{o}K$

$p_1 = p_0 = 13.9$ Torr

$M_S = 7.92$

Velocity	Number of (χ,τ) Points	Experimental Value (m/sec)	R.M.S. Deviation (m/sec)	Theoretical Value (m/sec)	$\frac{(\ )_{exp't}}{(\ )_{theory}}$
U_R	40	342.	6.6	299.	1.14
$C_1(0)$	208	273.	0.8	275.	.99
$C_1(6)$	143	250.	2.6	323.	.77
$C_1(7)$	130	329.	7.3	327.	1.01
$C_2(6)$	113	29.1	0.4	36.5	.80
$C_2(7)$	4	---	---	12.5	---
$C_2(8)$	8	16.1	4.2	-0.88	-18.3
$u_5 = u_6$	---	9.96	---	19.5	.51
$C_2(6) - u_6$	---	19.1	---	7.0	1.13

Table 2e. Comparison of Experimental & Theoretical Velocities

$T_1 = T_0 = 1.989^{\circ}K$

$P_1 = P_0 = 23.0$ Torr

$M_S = 6.50$

Velocity	Number of (χ,τ) Points	Experimental Value (m/sec)	R.M.S. Deviation (m/sec)	Theoretical Value (m/sec)	$\frac{(\ )_{exp't}}{(\ )_{theory}}$
U_R	25	282.	9.5	254.	1.11
$C_1(0)$	149	263.	0.4	274.	.96
$C_1(6)$	113	261.	1.5	324.	.81
$C_1(7)$	111	252.	3.2	338.	.75
$C_2(6)$	63	25.6	0.3	33.1	.77
$C_2(7)$	---	---	---	---	---
$C_2(8)$	---	---	---	---	---
$u_5 = u_6$	---	10.2	---	20.8	.49
$C_2(6) - u_6$	---	15.4	---	12.3	1.25

Table 2f. Comparison of Experimental & Theoretical Velocities

$T_1 = T_0 = 2.031^{\circ}K$

$p_1 = p_0 = 26.0$ Torr

$M_S = 6.23$

Velocity	Number of (χ,τ) Points	Experimental Value (m/sec)	R.M.S. Deviation (m/sec)	Theoretical Value (m/sec)	$\frac{(\ )_{exp't}}{(\ )_{theory}}$
U_R	25	308.	7.5	245.	1.26
$C_1(0)$	121	260.	0.6	274.	.95
$C_1(6)$	89	256.	3.6	324.	.79
$C_1(7)$	88	255	5.2	344.	.74
$C_2(6)$	50	23.5	0.5	30.7	.77
$C_2(7)$	---	---	---	---	---
$C_2(8)$	---	---	---	---	---
$u_5 = u_6$	---	11.1	---	21.3	.52
$C_2(6) - u_6$	---	12.5	---	9.39	1.33

Table 2g. Comparison of Experimental & Theoretical Velocities

$T_1 = T_0 = 2.095^{o}K$

$p_1 = p_0 = 31.0$ Torr

$M_S = 6.52$

Velocity	Number of (χ,τ) Points	Experimental Value (m/sec)	R.M.S. Deviation (m/sec)	Theoretical Value (m/sec)	$\frac{(\ )_{exp't}}{(\ )_{theory}}$
U_R	28	314.	10.	256.	1.23
$C_1(0)$	134	276.	0.7	286.	.96
$C_1(6)$	86	253.	4.0	357.	.71
$C_1(7)$	82	311.	9.4	370.	.84
$C_2(6)$	---	---	---	---	---
$C_2(7)$	---	---	---	---	---
$C_2(8)$	---	---	---	---	---
$u_5 = u_6$	---	11.2	---	26.5	.42
$C_2(6) - u_6$	---	---	---	---	---

Table 2h. Summarized Comparison of Theoretical and Experimental Velocities

Velocity	$\frac{( )_{exp't}}{( )_{theory}}$						
	T_0 = 1.522	1.665	1.751	1.832	1.989	2.031	2.095
U_R	1.19	1.05	1.33	1.14	1.11	1.26	1.23
$C_1(0)$	.99	.98	.99	.99	.96	.95	.96
$C_1(6)$	.89	.91	.86	.77	.81	.79	.71
$C_1(7)$	.84	.84	.86	1.01	.75	.74	.84
$C_2(6)$	.90	.82	.84	.80	.77	.77	---
$C_2(7)$	1.31	1.26	---	---	---	---	---
$C_2(8)$	3.76	2.89	7.04	-18.3	---	---	---
$u_5 = u_6$	.66	.57	.70	.51	.49	.52	.42
$C_2(6) - u_6$	1.11	1.02	.98	1.13	1.25	1.33	---

Table 3a. Summary of Theoretical Flow Field Calculations

$T_1 = T_0 = 1.522^{o}K$

$p_1 = p_0 = 4.00$ Torr

$M_S = 13.0$

Region	Pressure (Atm)	Temperature (^{o}K)	Density (g/cm^3)
0	5.27×10^{-3}	1.522	.145
1	5.27×10^{-3}	1.522	1.69×10^{-4}
2	1.10	81.1	6.63×10^{-4}
5	6.29	188.	1.63×10^{-3}
6	6.29	$\sim$1.522	.155
7	14.4	$\sim$1.522	.163
8	6.70	$\sim$1.522	.155
9	6.70	193.	1.69×10^{-3}

Table 3b. Summary of Theoretical Flow Field Calculations

$T_1 = T_0 = 1.665^{\circ}K$

$p_1 = p_0 = 7.48$ Torr

$M_S = 9.17$

Region	Pressure (Atm)	Temperature ($^{\circ}K$)	Density (g/cm^3)
0	9.85×10^{-3}	1.665	.145
1	9.85×10^{-3}	1.665	2.88×10^{-4}
2	1.03	45.2	1.11×10^{-3}
5	5.73	103.	2.70×10^{-3}
6	5.73	$\sim$1.665	.154
7	13.0	$\sim$1.665	.162
8	6.20	$\sim$1.665	.155
9	6.20	107.	2.84×10^{-3}

Table 3c. Summary of Theoretical Flow Field Calculations

$T_1 = T_0 = 1.751^{o}K$

$p_1 = p_0 = 10.4$ Torr

$M_S = 8.60$

Region	Pressure (Atm)	Temperature (^{o}K)	Density (g/cm^3)
0	1.37×10^{-2}	1.751	.145
1	1.37×10^{-2}	1.751	3.82×10^{-4}
2	1.26	42.0	1.47×10^{-3}
5	6.90	94.7	3.55×10^{-3}
6	6.90	$\sim$1.751	.156
7	16.0	$\sim$1.751	.164
8	7.61	$\sim$1.751	.157
9	7.61	98.5	3.77×10^{-3}

Table 3d. Summary of Theoretical Flow Field Calculations

$T_1 = T_0 = 1.832^{\circ}K$

$p_1 = p_0 = 13.9$ Torr

$M_S = 7.92$

Region	Pressure (Atm)	Temperature ($^{\circ}K$)	Density (g/cm^3)
0	1.83×10^{-2}	1.832	.146
1	1.83×10^{-2}	1.832	4.88×10^{-4}
2	1.43	37.6	1.86×10^{-3}
5	7.71	84.1	4.47×10^{-3}
6	7.71	$\sim$1.832	.157
7	18.0	$\sim$1.832	.166
8	8.64	$\sim$1.832	.159
9	8.64	88.0	4.78×10^{-3}

Table 3e. Summary of Theoretical Flow Field Calculations

$T_1 = T_0 = 1.989^{o}K$

$p_1 = p_0 = 23.0$ Torr

$M_S = 6.50$

Region	Pressure (Atm)	Temperature (^{o}K)	Density (g/cm^3)
0	3.03×10^{-2}	1.989	.146
1	3.03×10^{-2}	1.989	7.42×10^{-4}
2	1.59	28.0	2.77×10^{-3}
5	8.24	61.3	6.56×10^{-3}
6	8.24	$\sim$1.989	.158
7*	19.4	$\sim$1.989	.168
8	9.46	$\sim$1.989	.160
9	9.46	64.8	7.12×10^{-3}

*Liquid Helium I

Table 3f. Summary of Theoretical Flow Field Calculations

$T_1 = T_0 = 2.031^{\circ}K$

$p_1 = p_0 = 26.0$ Torr

$M_S = 6.23$

Region	Pressure (Atm)	Temperature ($^{\circ}K$)	Density (g/cm^3)
0	3.42×10^{-2}	2.031	.146
1	3.42×10^{-2}	2.031	8.21×10^{-4}
2	1.63	26.4	3.05×10^{-3}
5	8.45	57.4	7.18×10^{-3}
6	8.45	$\sim$2.031	.158
7*	20.0	$\sim$2.031	.169
8	9.76	$\sim$2.031	.161
9	9.76	60.8	7.83×10^{-3}

* Liquid Helium I

Table 3g. Summary of Theoretical Flow Field Calculations

$T_1 = T_0 = 2.095^{o}K$

$p_1 = p_0 = 31.0$ Torr

$M_S = 6.52$

Region	Pressure (Atm)	Temperature (^{o}K)	Density (g/cm^3)
0	4.08×10^{-2}	2.095	.146
1	4.08×10^{-2}	2.095	9.49×10^{-4}
2	2.16	29.7	3.55×10^{-3}
5	11.0	64.2	8.33×10^{-3}
6*	11.0	$\sim$2.095	.161
7*	27.1	$\sim$2.095	.173
8*	13.0	$\sim$2.095	.165
9	13.0	68.7	9.22×10^{-3}

*Liquid Helium I

Table 4. Temperature Jump and Relative Velocity Estimates for First-Sound Shock Waves

T_0 (^oK)	$\Delta\overline{T}_{exp't}$ (^oK)	R.M.S. Deviation (^oK)	ΔT_{theory} (^oK)	$\frac{\Delta\overline{T}_{exp't}}{\Delta T_{theory}}$	$w_{exp't}$ (m/sec)
1.522	-.012	.002	-.014	.86	-.089
1.665	-.021	.002	-.016	1.31	-.16
1.751	-.035	.005	-.020	1.75	-.26
1.832	-.033	.002	-.023	1.43	-.24
1.989	-.048	.013	-.025	1.92	-.36
2.031	-.059	.014	-.028	2.11	-.44
2.095	-.055	.002	-.043	1.28	---

Table 5. Temperature Jump and Relative Velocity Estimates for Second-Sound Shock Waves

T_0 (^oK)	$\Delta T_{exp't}$ (^oK)	R.M.S. Deviation (^oK)	w (m/sec)
1.522	.033	.011	2.7
1.665	.028	.002	2.3
1.751	.037	.005	3.1
1.832	.031	.007	2.7
1.989	.026	.011	3.1
2.031	.011	.003	1.7

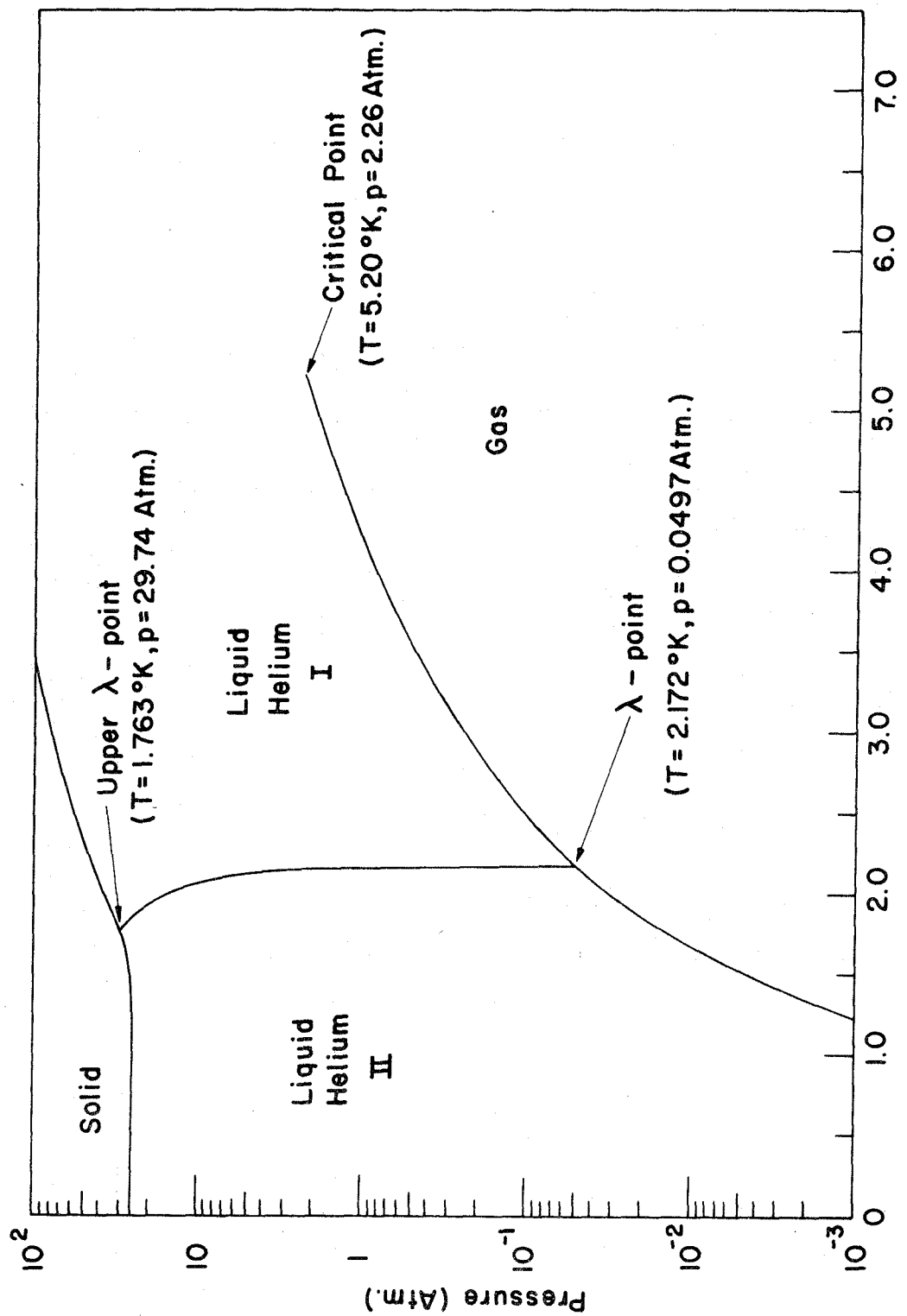

Figure 1. ^{4}He Phase Diagram

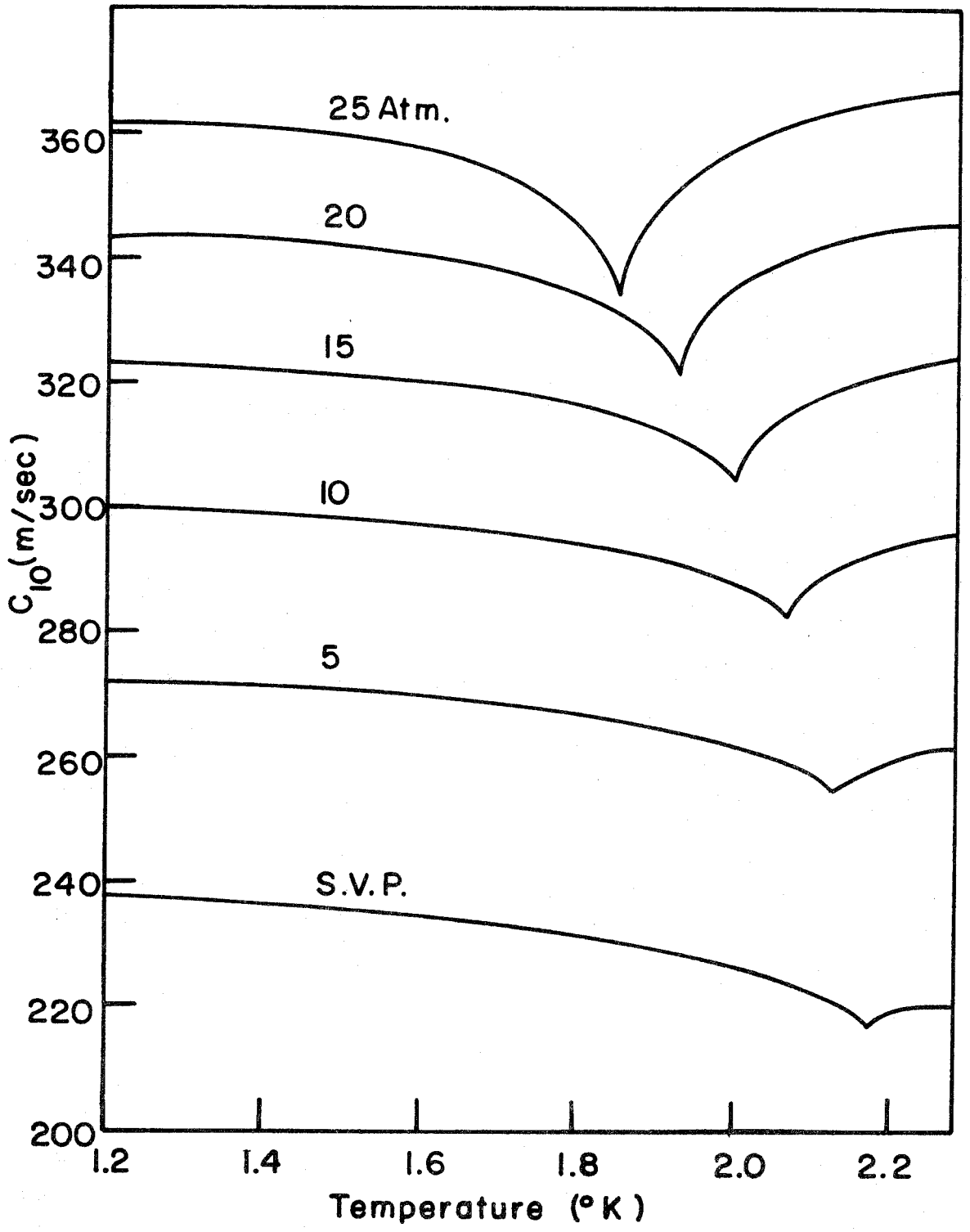

Figure 2. Dependence of First-Sound Velocity on Temperature and Pressure (S.V.P. = Saturated Vapor Pressure)

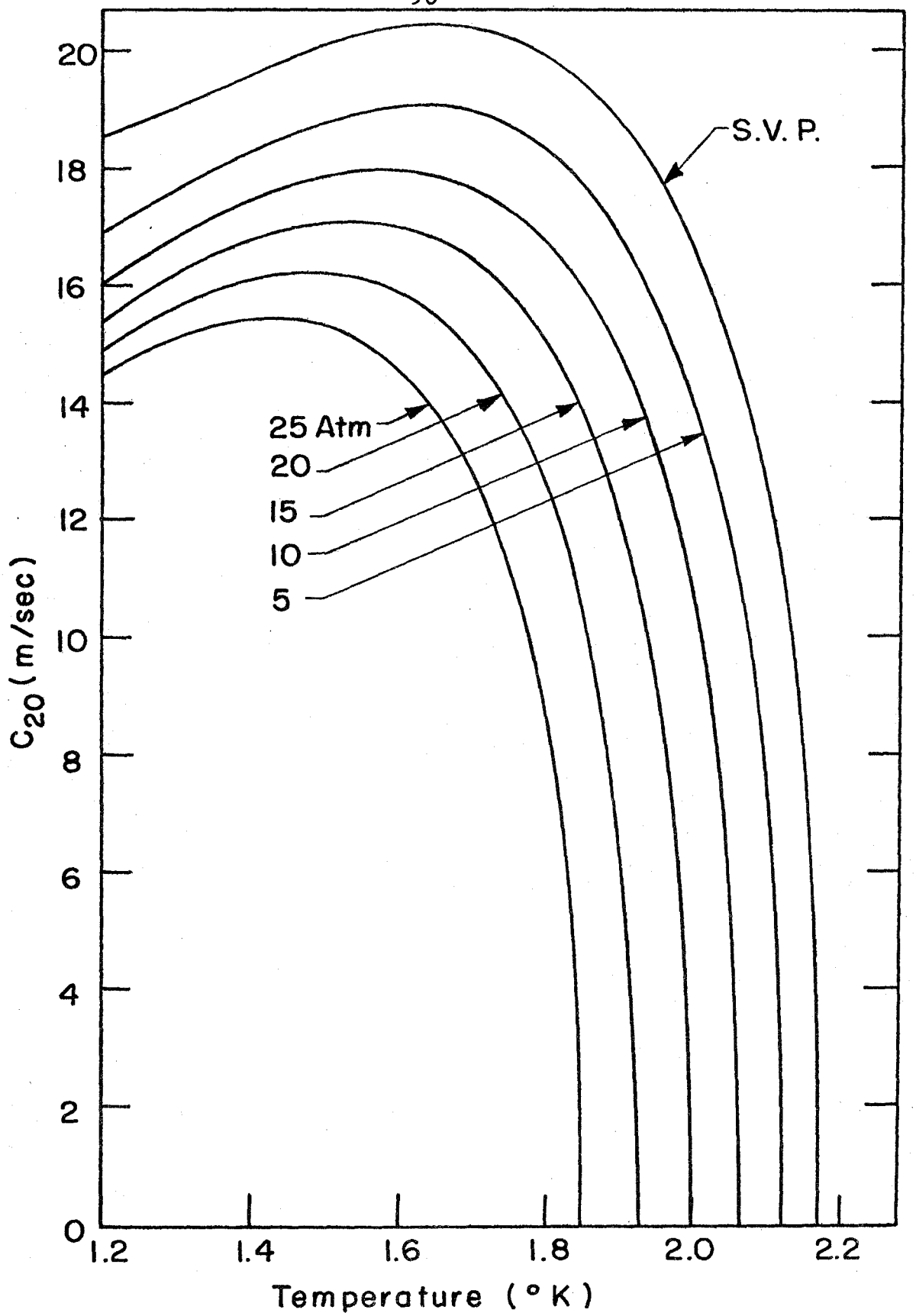

Figure 3. Dependence of Second-Sound Velocity on Temperature and Pressure (S.V.P. = Saturated Vapor Pressure)

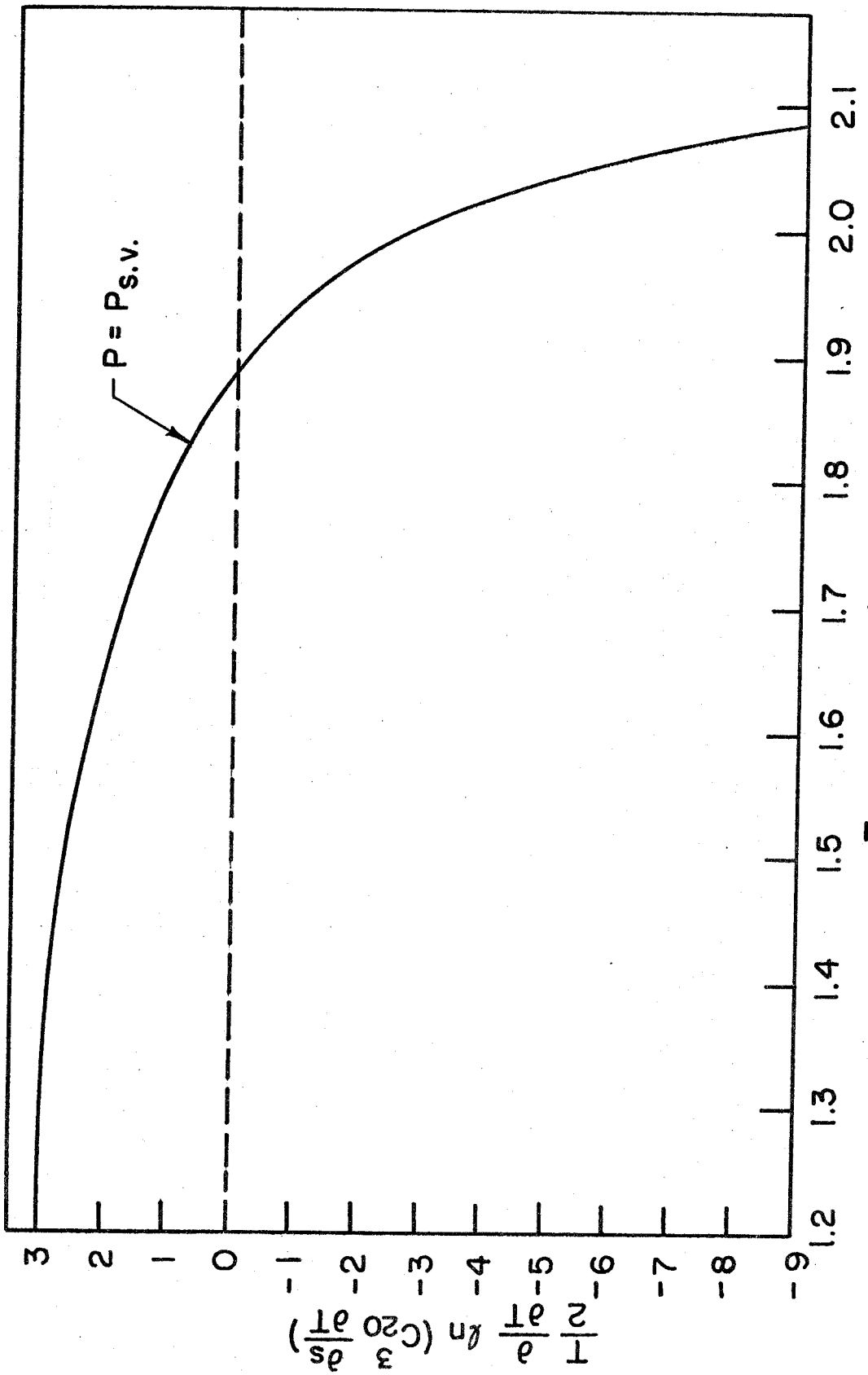

Figure 4. Variation of the Coefficient $\frac{T}{2}\frac{\partial}{\partial T}\ell n\,(C_{20}^{3}\frac{\partial s}{\partial T})$ with Temperature at S.V.P.

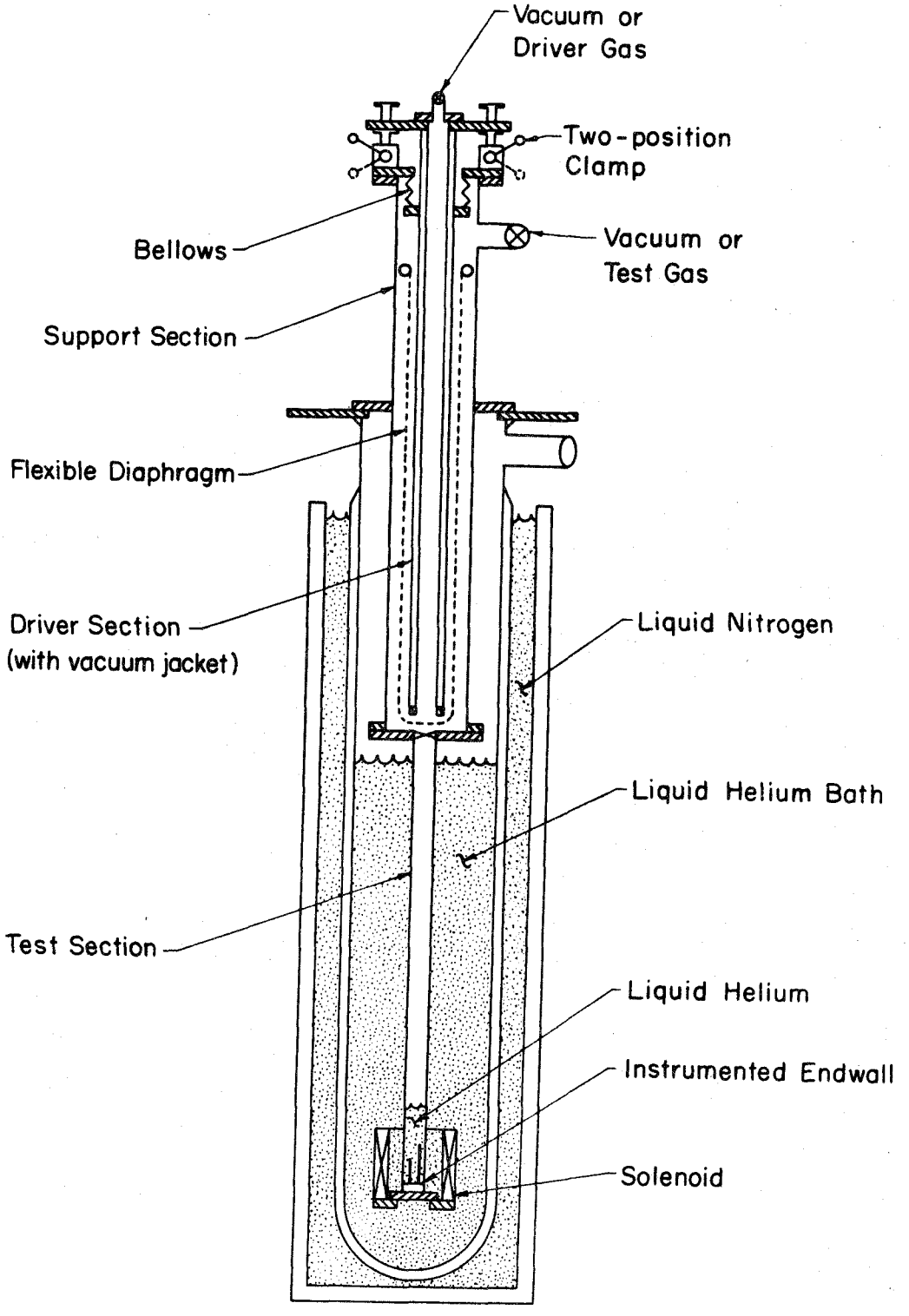

CRYOGENIC SHOCK TUBE ASSEMBLY

Figure 5.

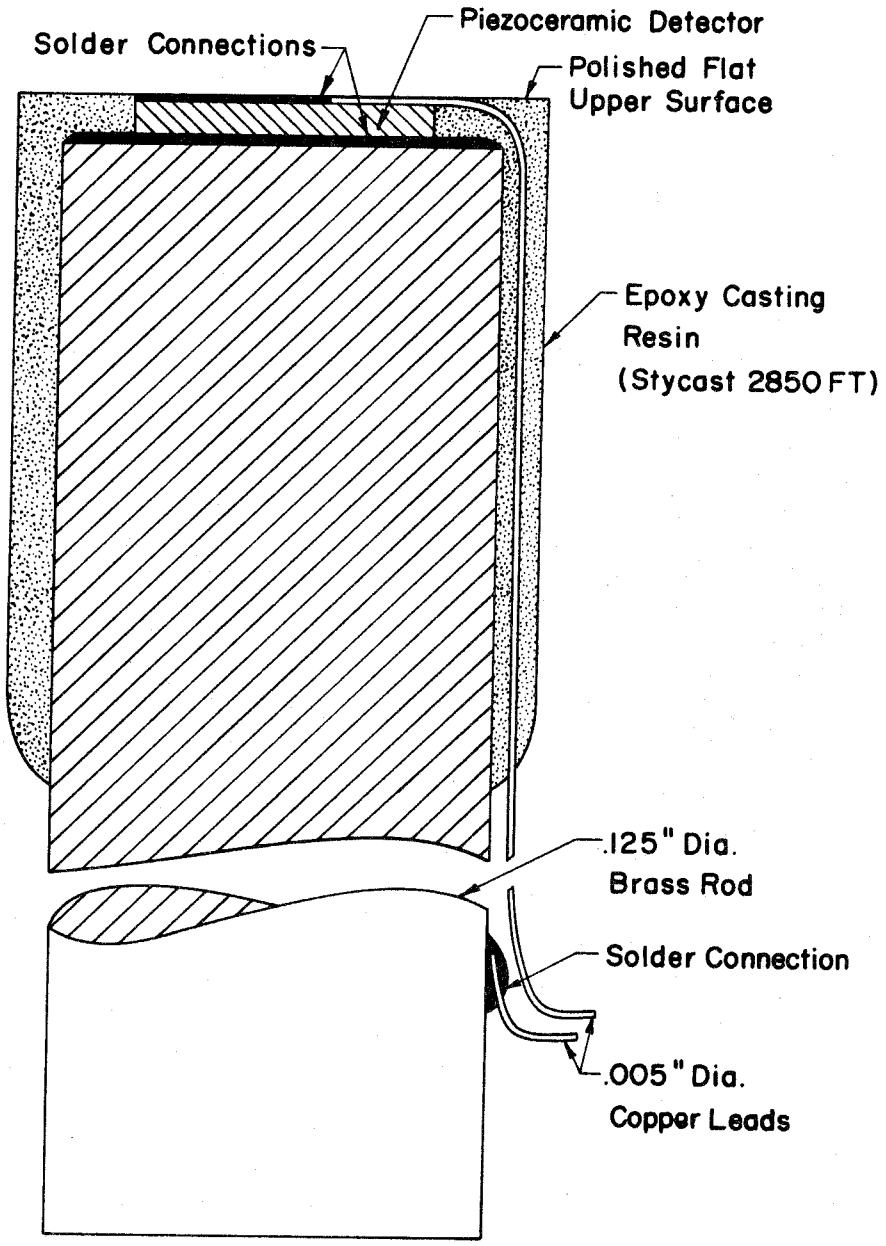

TOP-MOUNTED PIEZOCERAMIC DETECTOR

Figure 6.

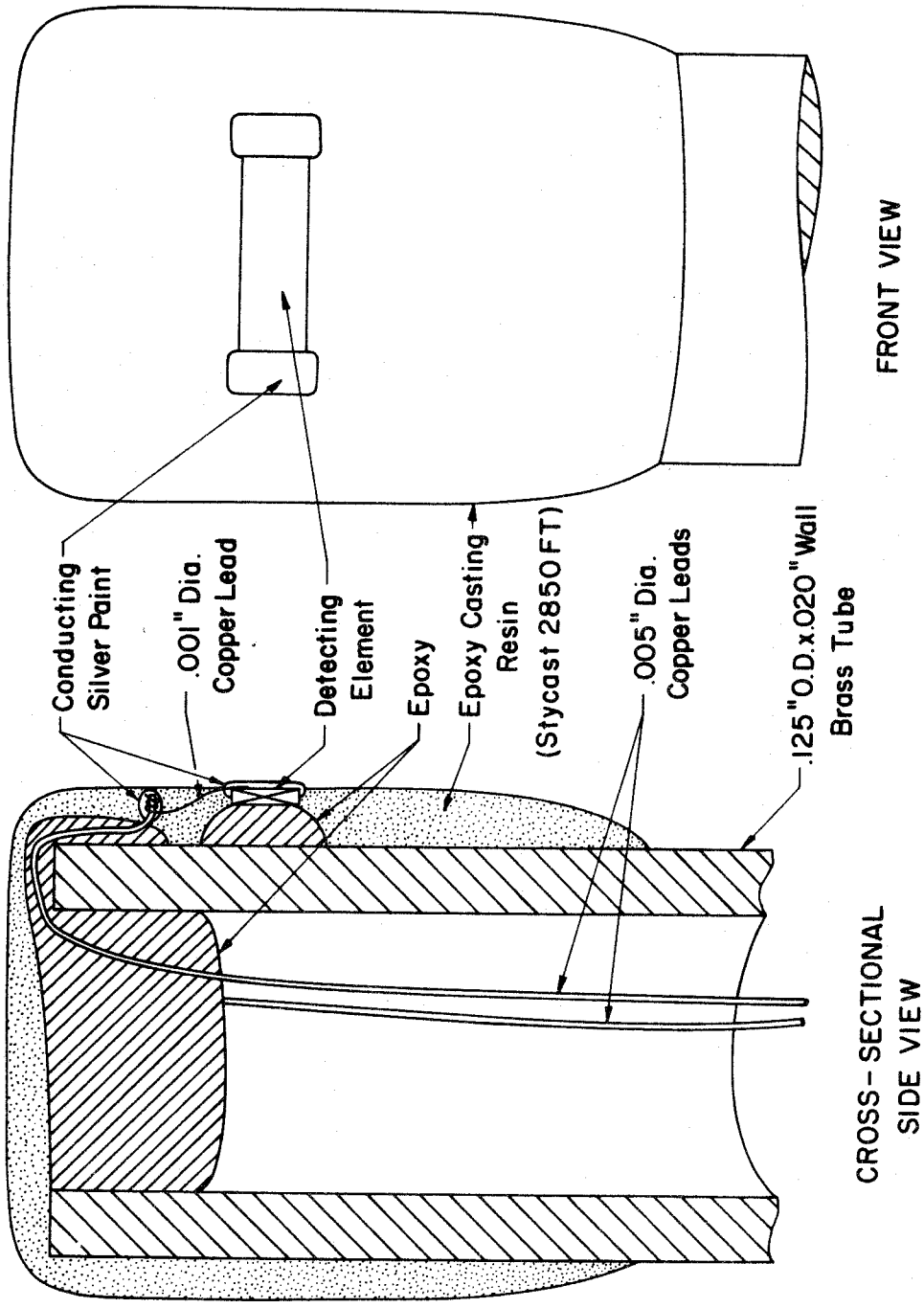

SIDE-MOUNTED CARBON-CARD DETECTOR

Figure 7.

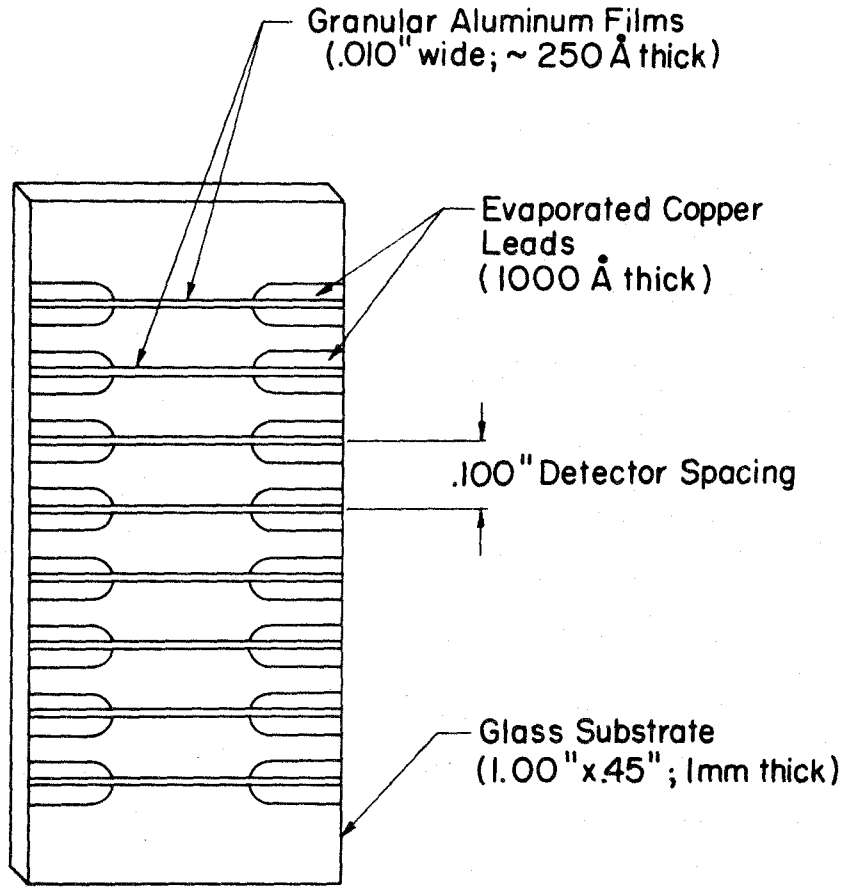

SIDE-MOUNTED SUPERCONDUCTING DETECTORS

Figure 8.

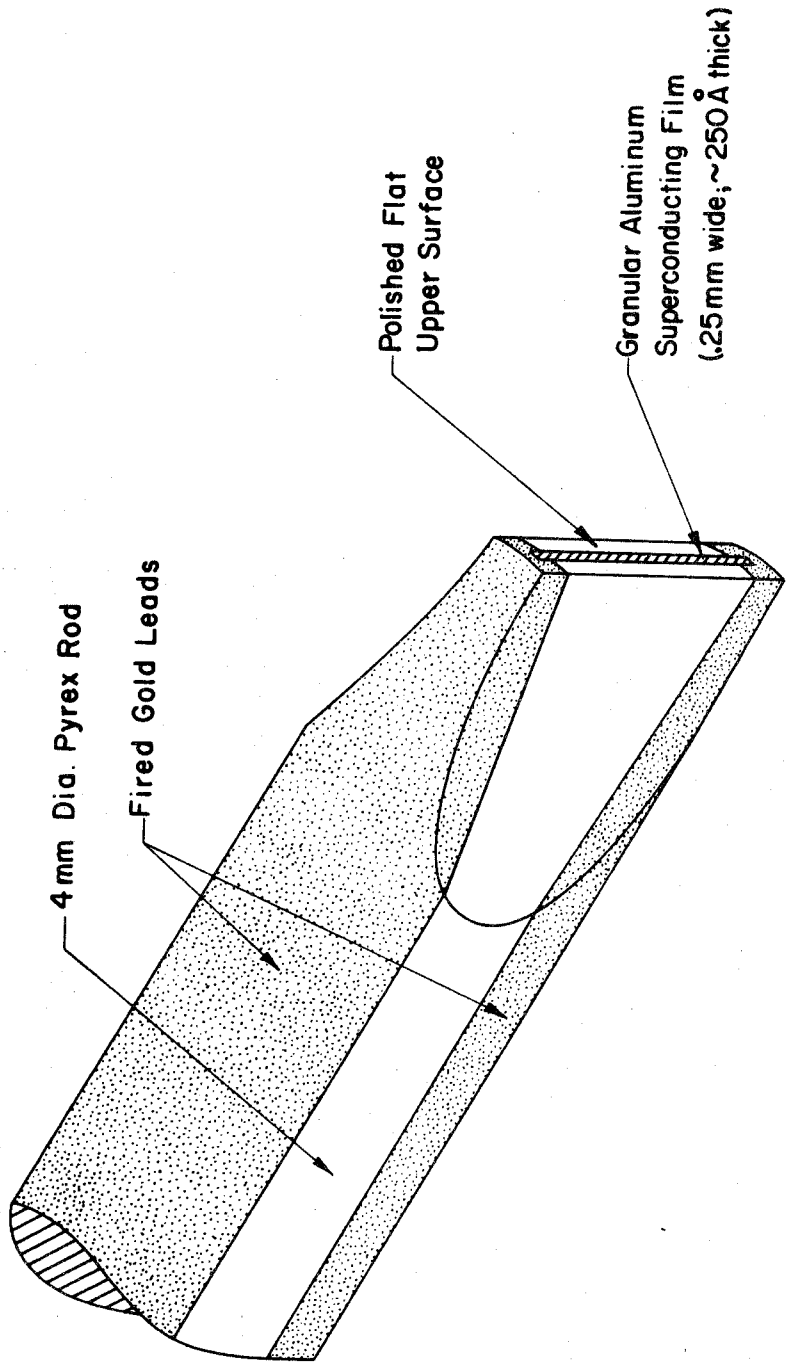

TOP-MOUNTED SUPERCONDUCTING DETECTOR

Figure 9.

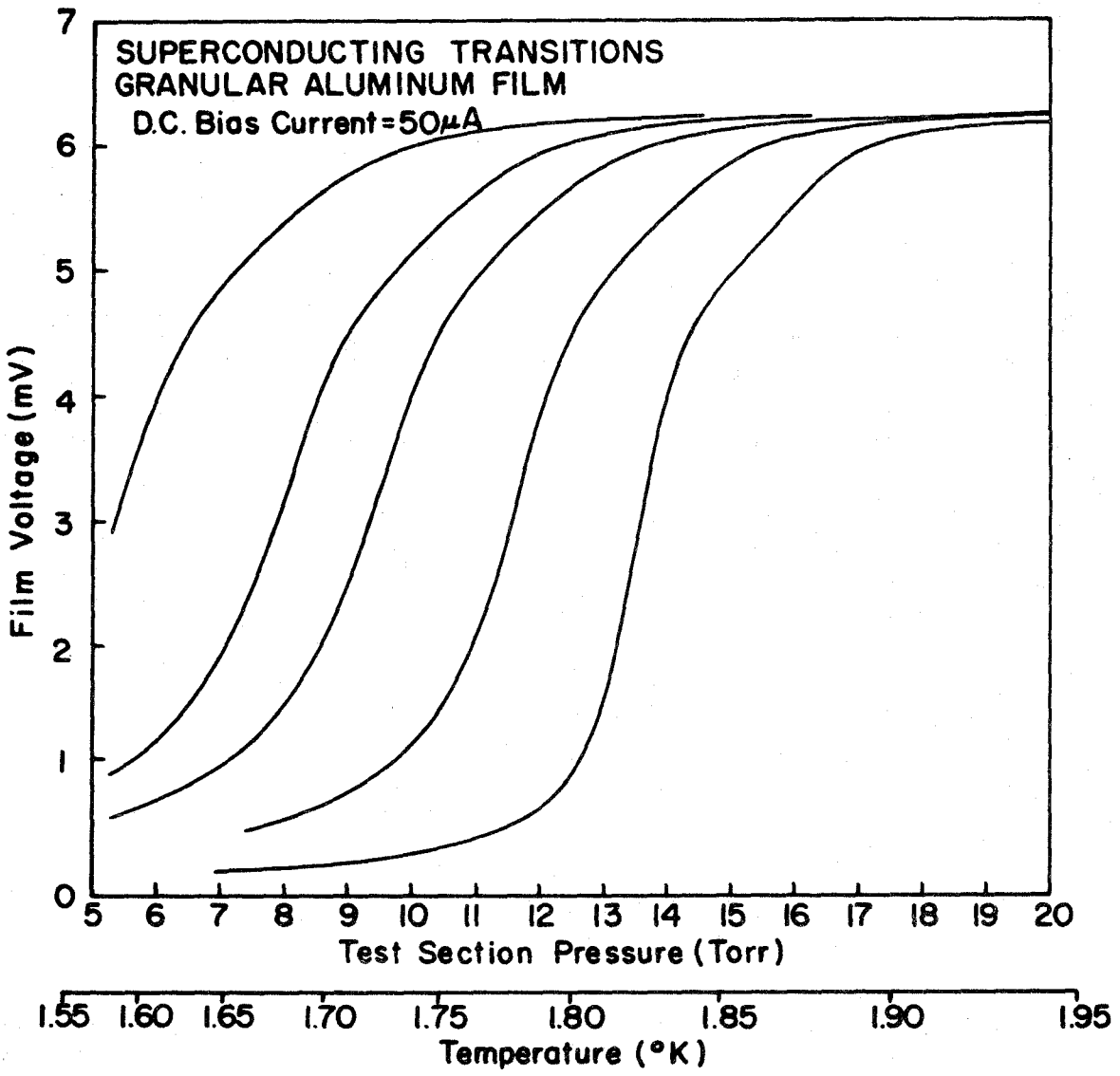

Figure 10. Superconducting Thin-Film Calibration

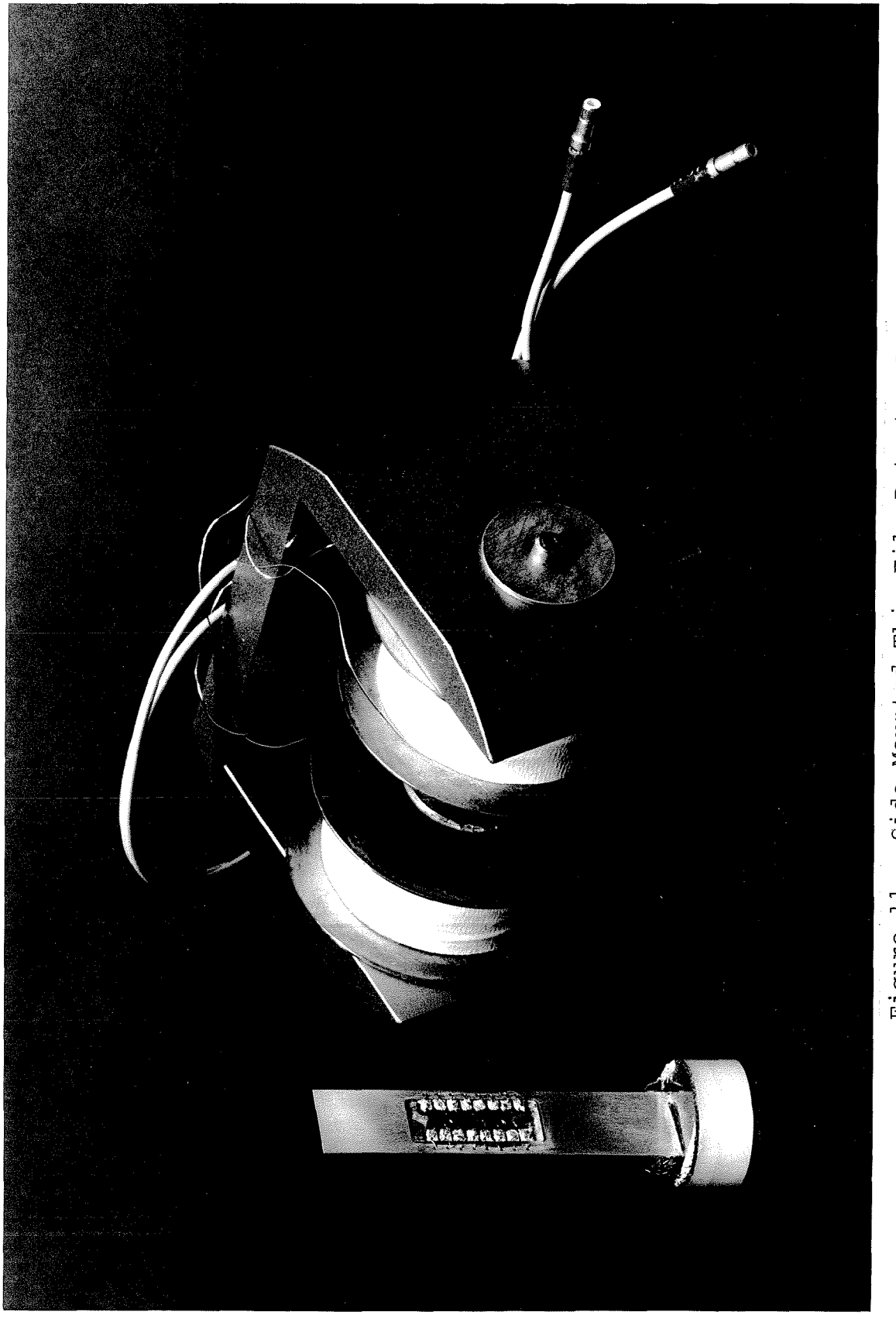

Figure 11. Side-Mounted Thin-Film Detector Array and Biasing Magnet

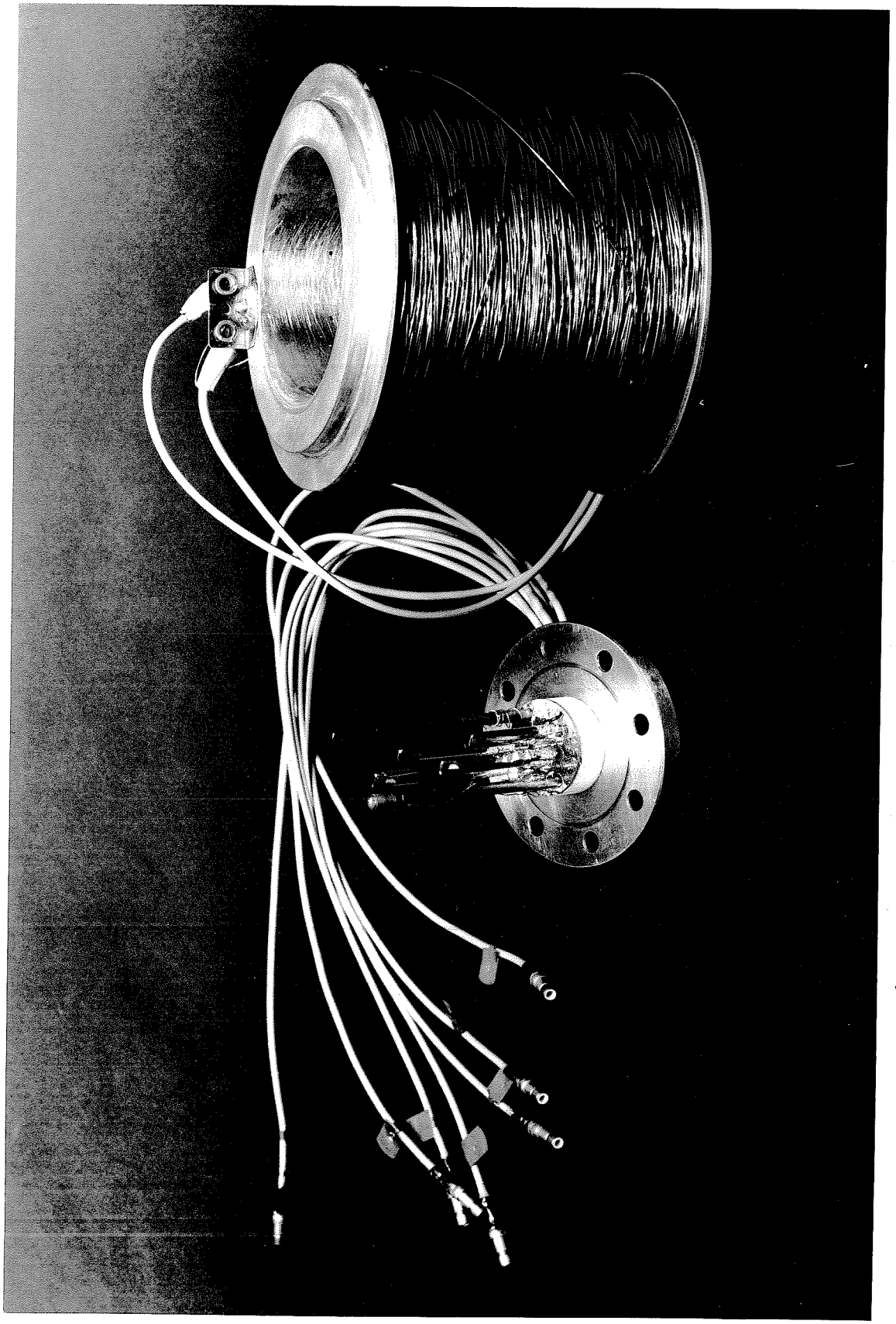

Figure 12. Top-Mounted Thin-Film Detector Array and Biasing Solenoid

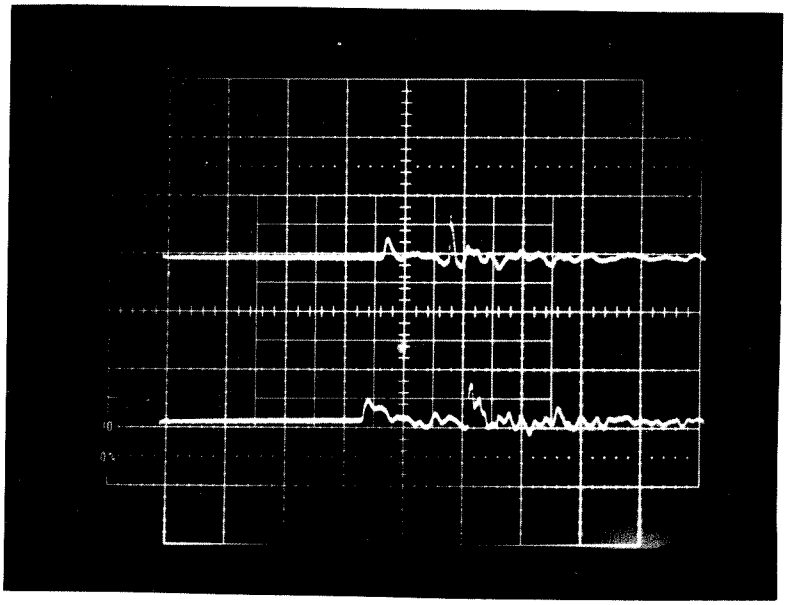

FILM 3
.4mV/div
.5msec/div

FILM 4
.4mV/div
.5msec/div

1/14/78, RUN 55
$P_1 = P_{s.v.} = 7.51$ torr
$T_1 = 1.666°K$

Figure 13. Thin-Film Response to a Second-Sound Level-Detection Pulse

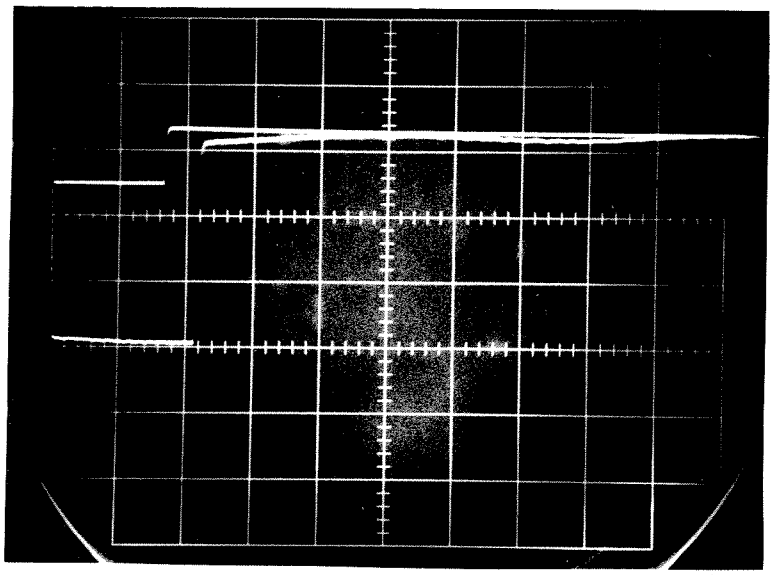

FILM 1
5 mV/div
10 μ sec/div

FILM 2
2mV/div
10 μ sec/div

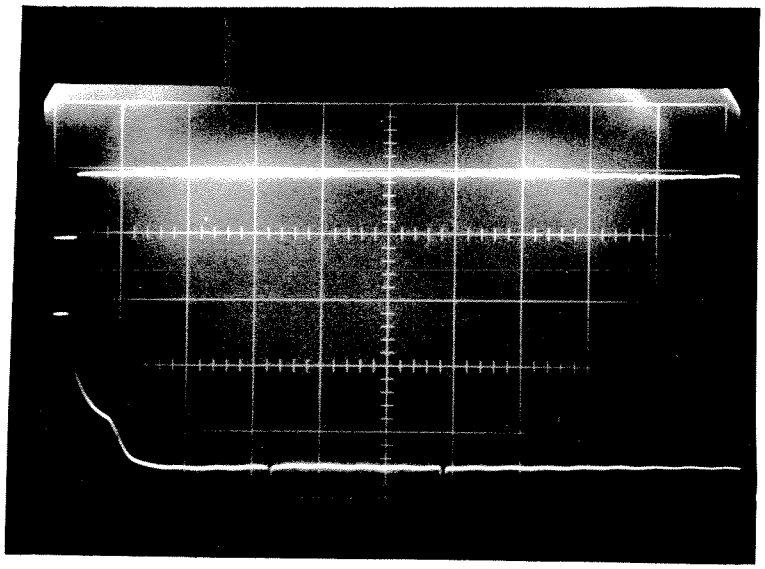

FILM 1
5mV/div
50μ sec/div

CARBON CARD
DETECTOR
.1V/div
50μ sec/div

1/14/78, RUN 56
$P_1 = P_{S.V.} = 7.40$ torr
$T_1 = 1.663\,^{\circ}K$

Figure 14. Detector Response to the Gas Flow Field

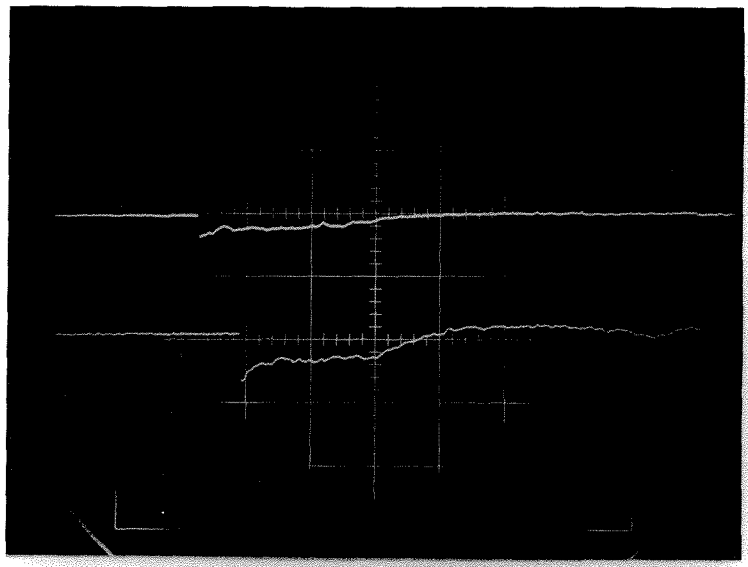

FILM 3
2mV/div
20 μ sec/div

FILM 4
2mV/div
20 μ sec/div

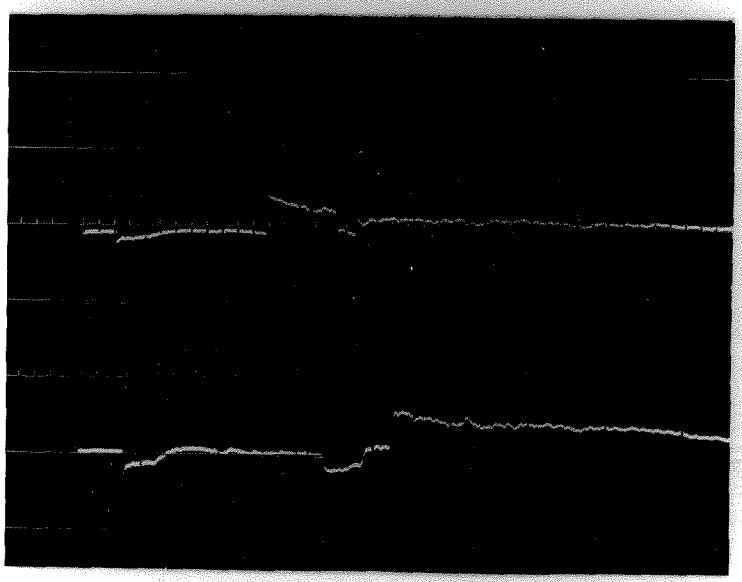

FILM 3
5mV/div
100 μ sec/div

FILM 4
5mV/div
100 μ sec/div

1/14/78, RUN 56
$P_1 = P_{s.v.} = 7.40$ torr
$T_1 = 1.663\ ^\circ K$

Figure 15. Detector Response to the Liquid Flow Field

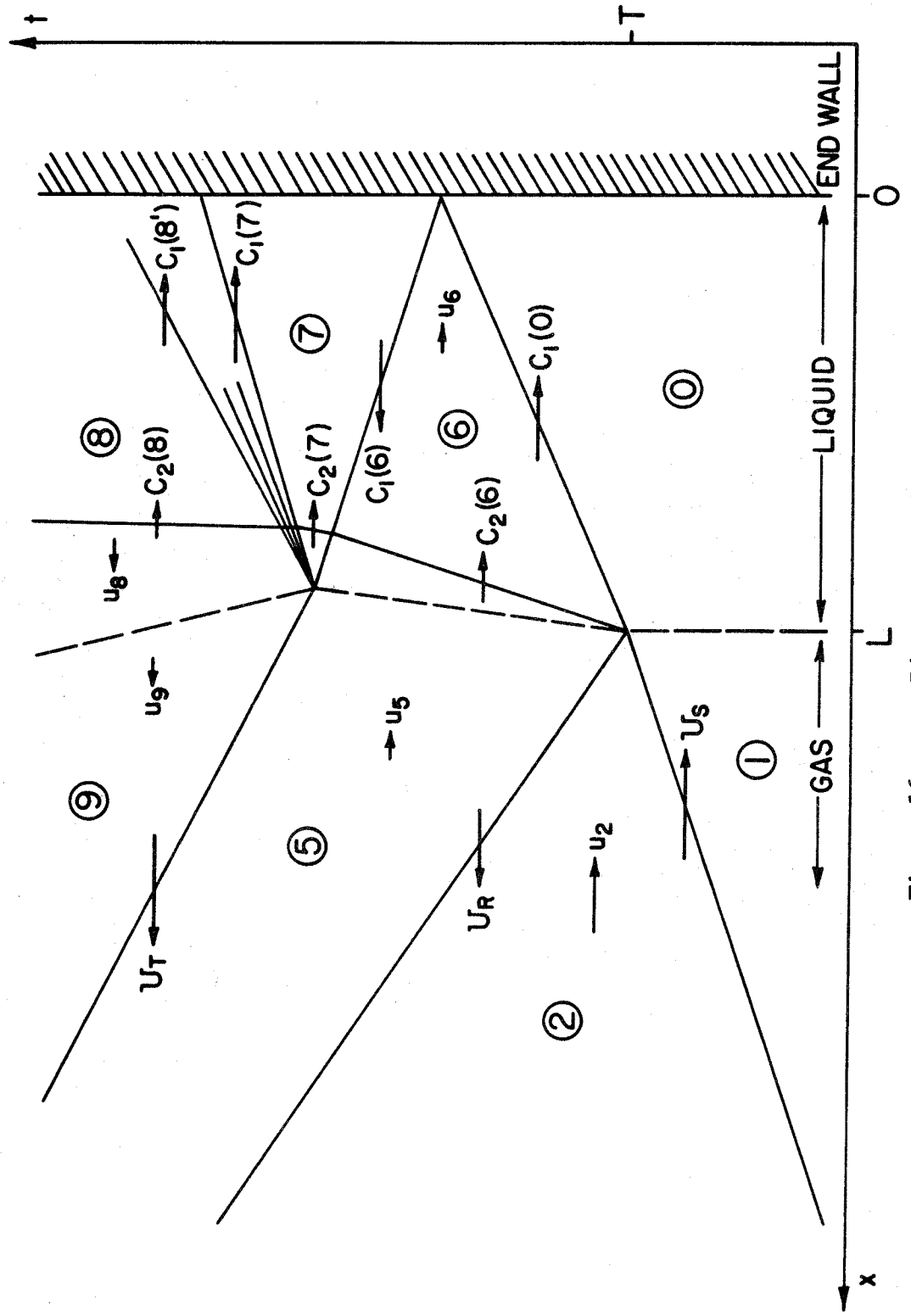

Figure 16. x-t Diagram Notation

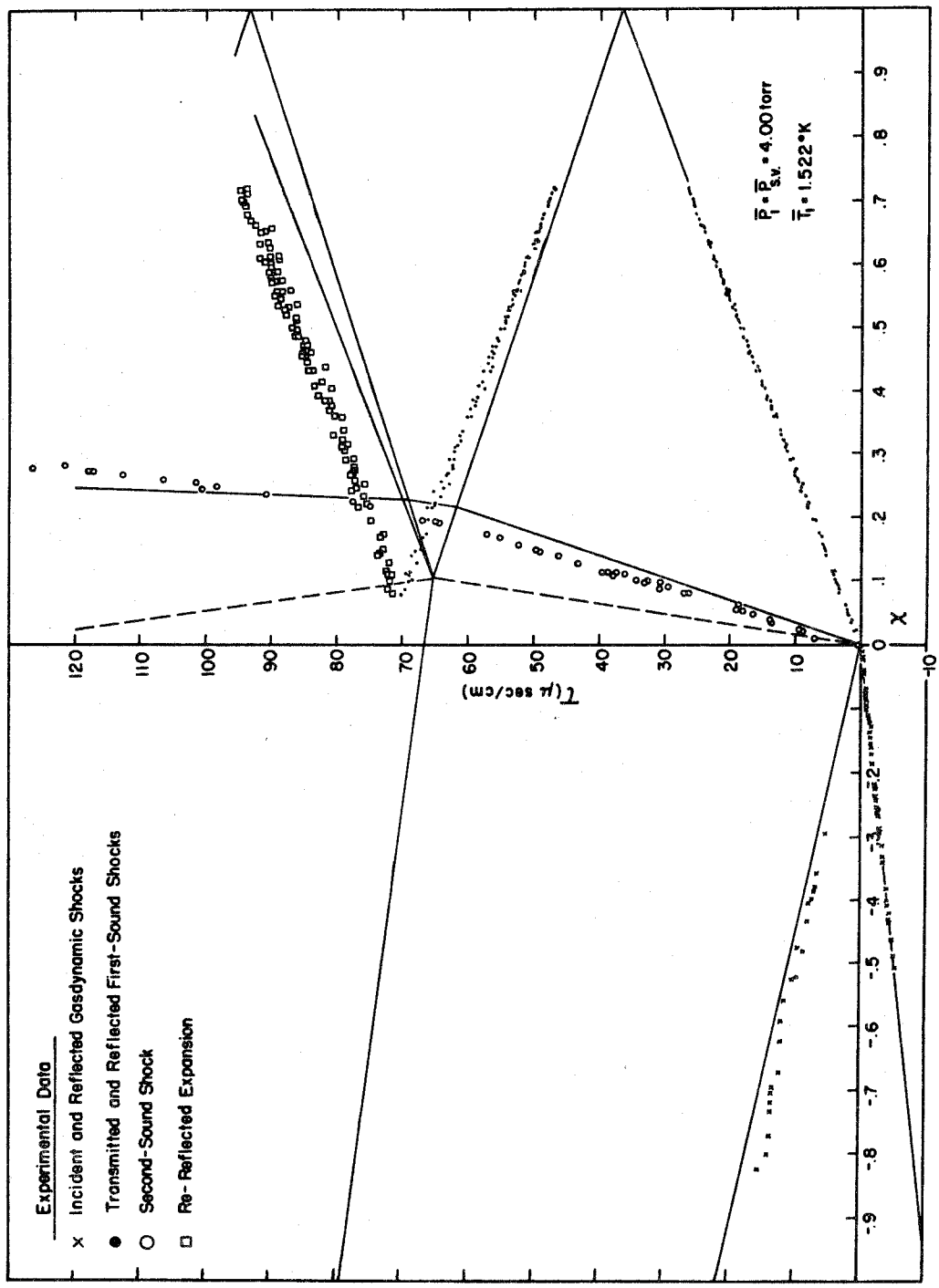

Figure 17a. χ-τ Diagram for $T_0 = 1.522^{\circ}K$

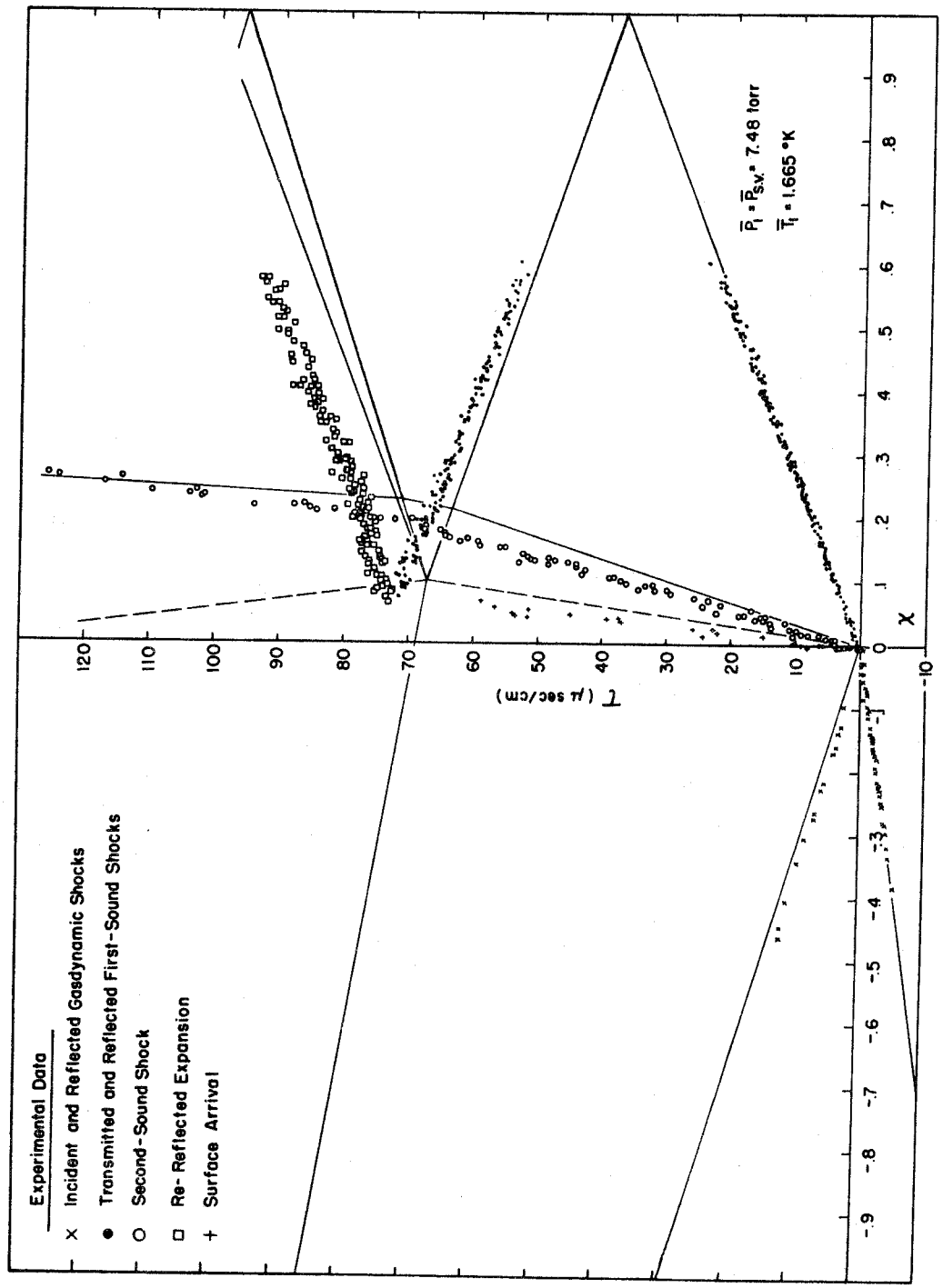

Figure 17b. χ-τ Diagram for $T_0 = 1.665^{\circ}K$

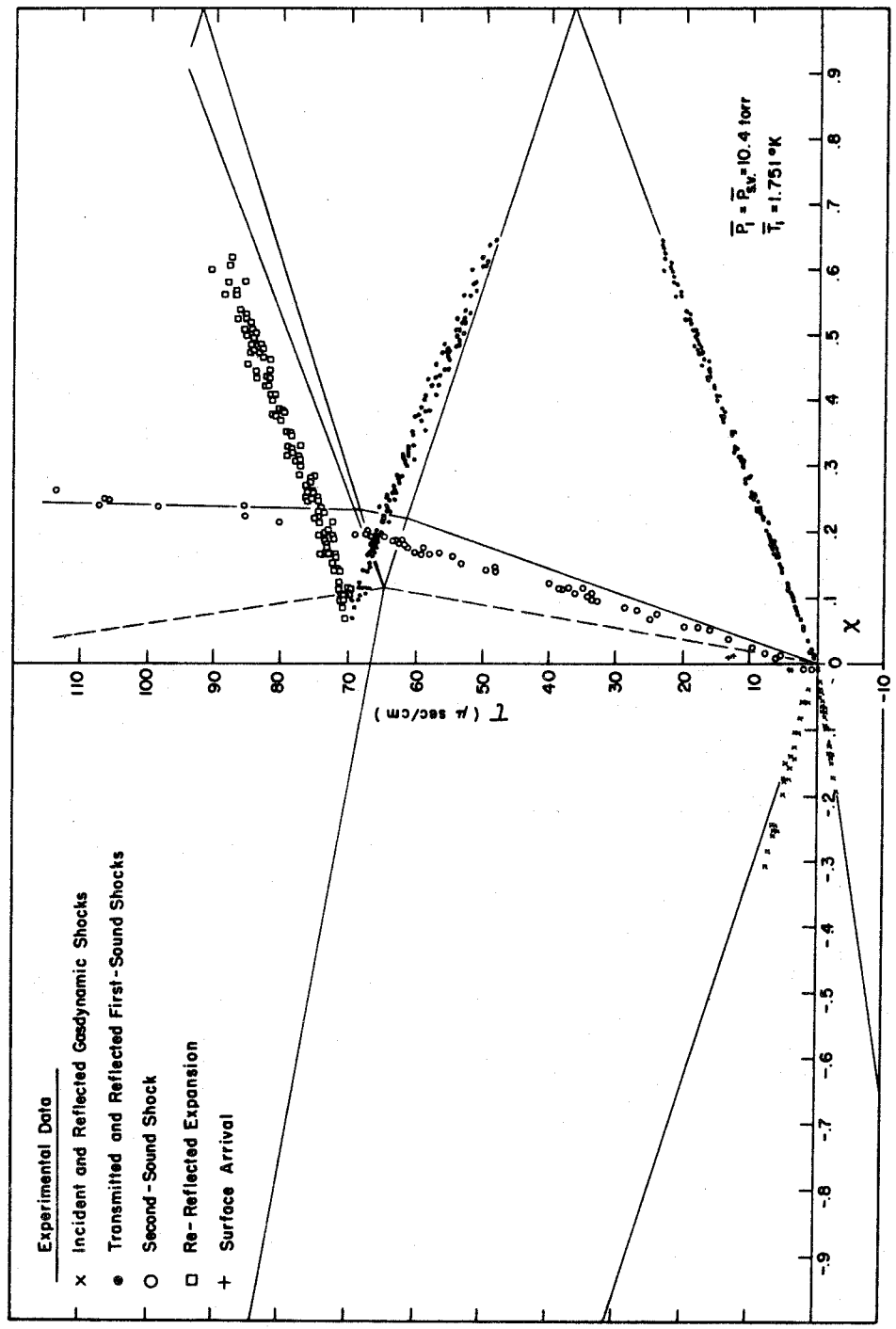

Figure 17c. χ-τ Diagram for $T_0 = 1.751^{\circ}K$

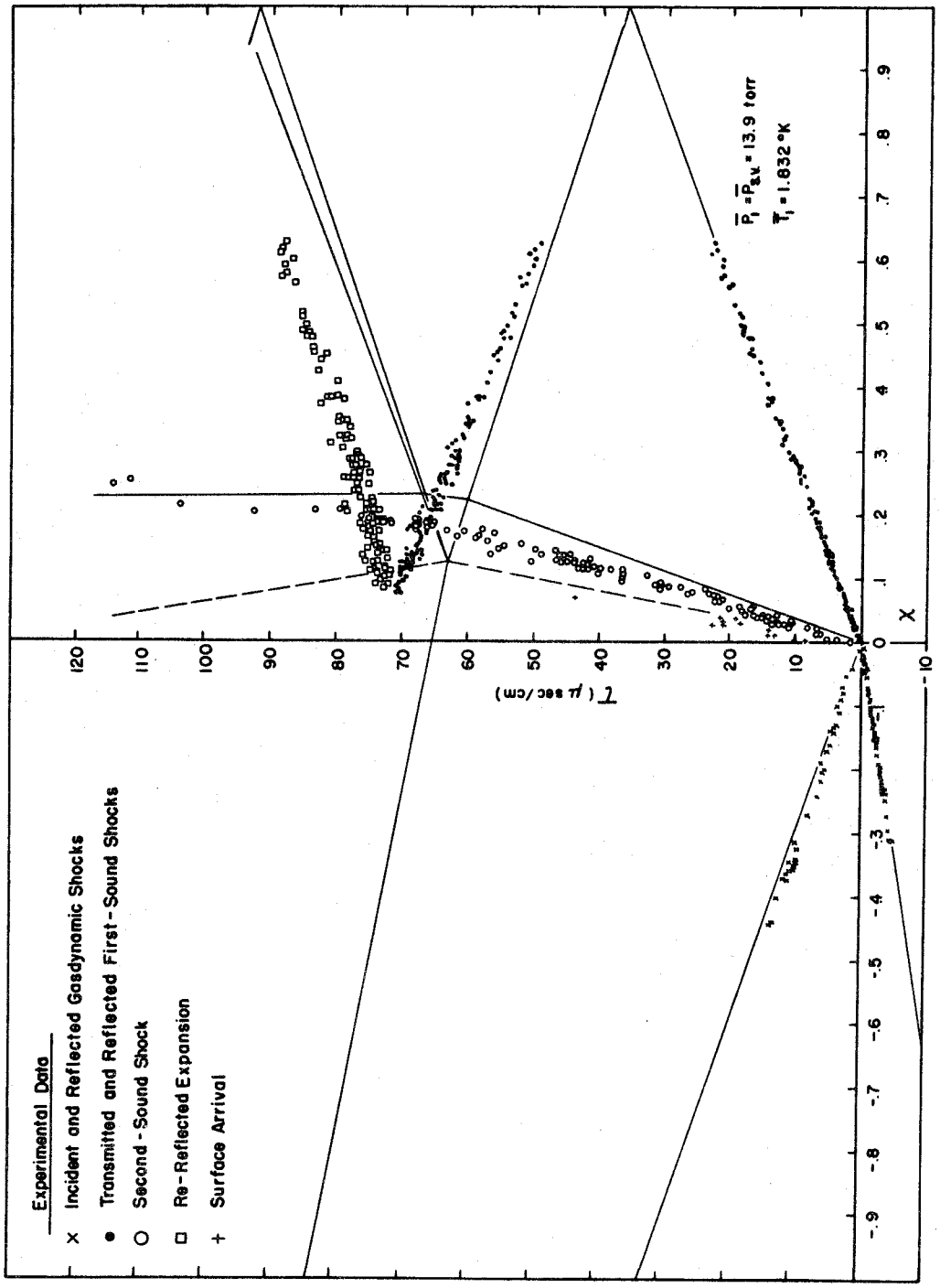

Figure 17d. χ-τ Diagram for $T_0 = 1.832^{\circ}K$

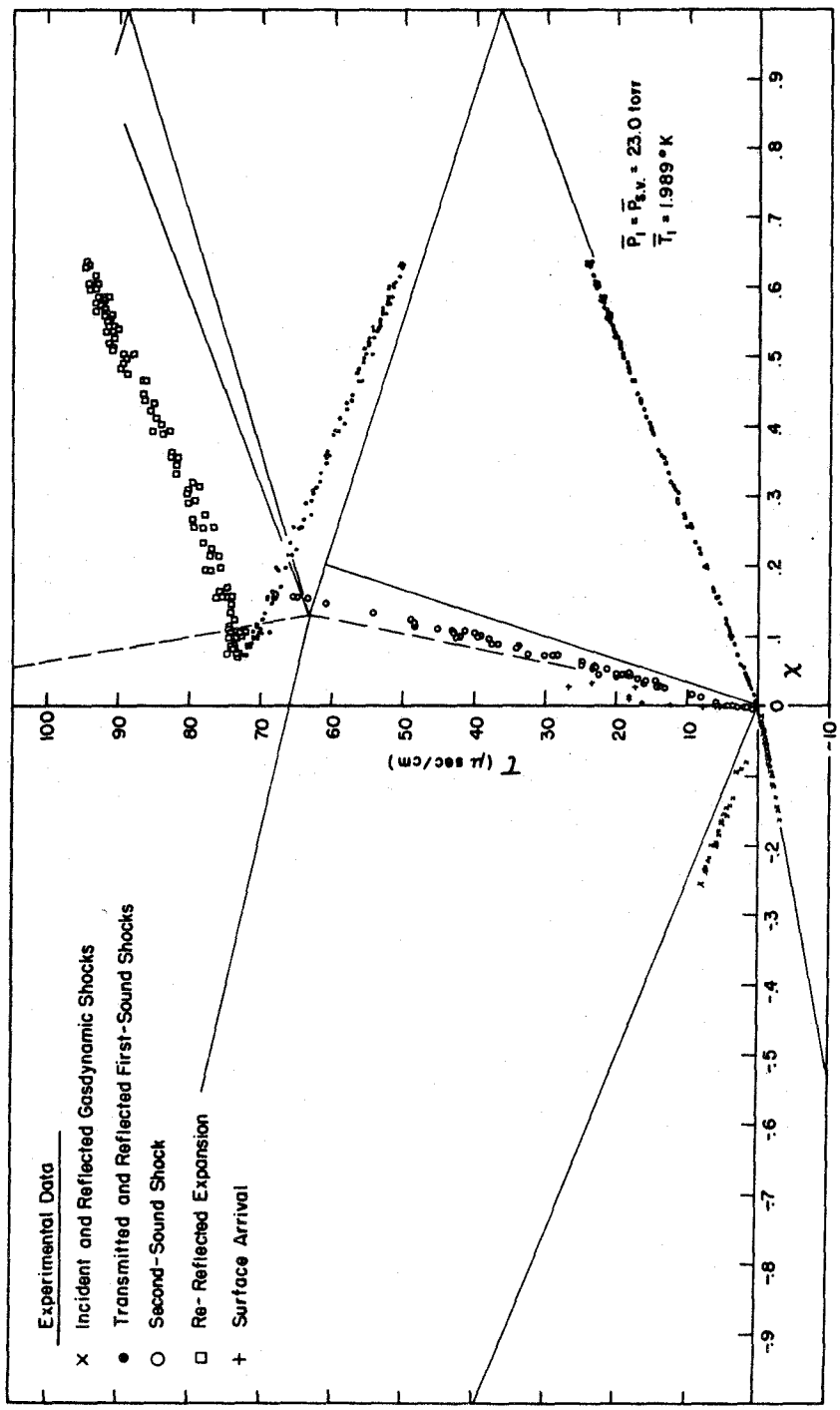

Figure 17e. χ-τ Diagram for $T_0 = 1.989^{\circ}K$

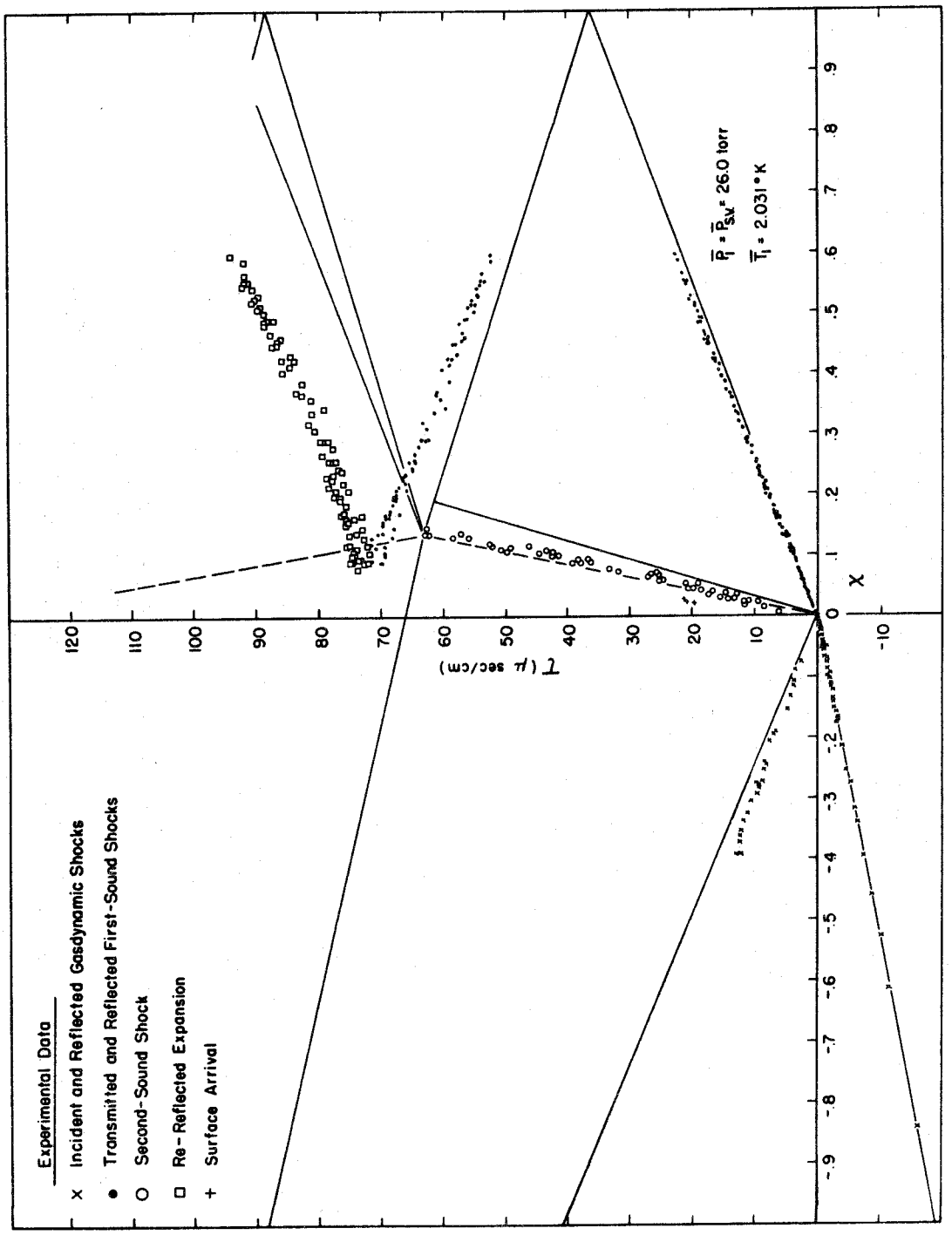

Figure 17f. χ-τ Diagram for $T_0 = 2.031^{o}K$

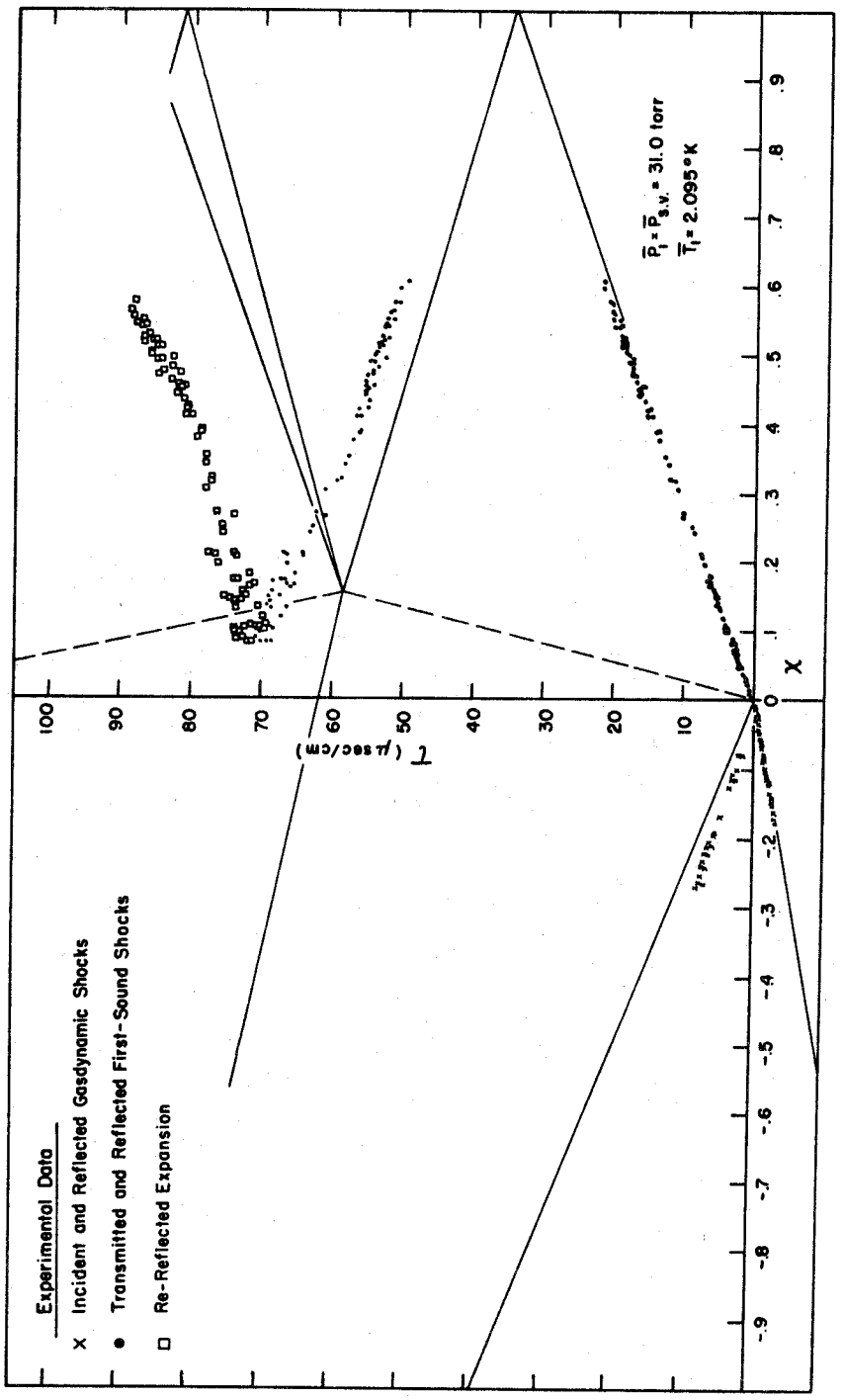

Figure 17g. χ-τ Diagram for $T_0 = 2.095°K$

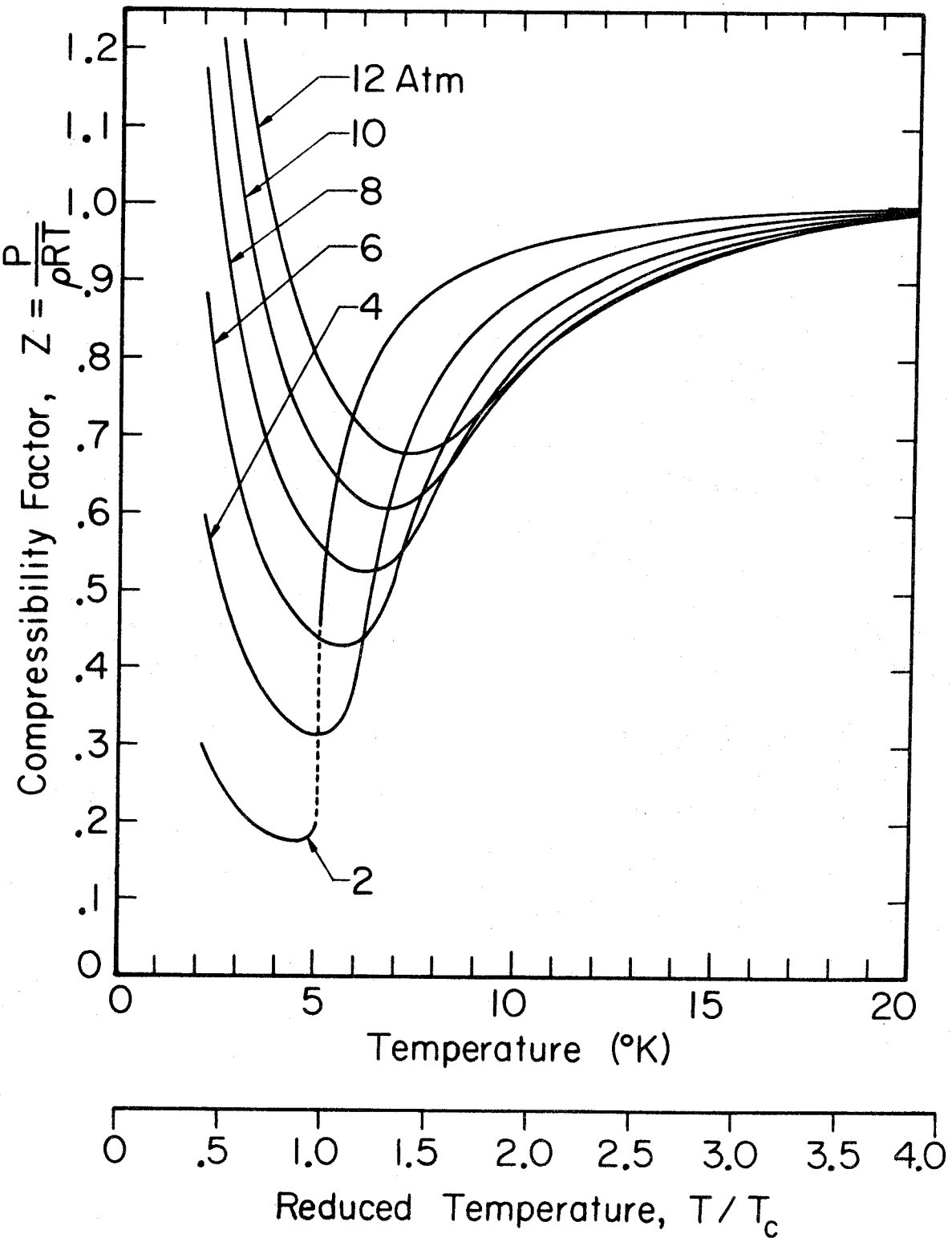

Figure 18. Dependence of Compressibility Factor, $Z = \frac{p}{\rho RT}$, on Temperature and Pressure

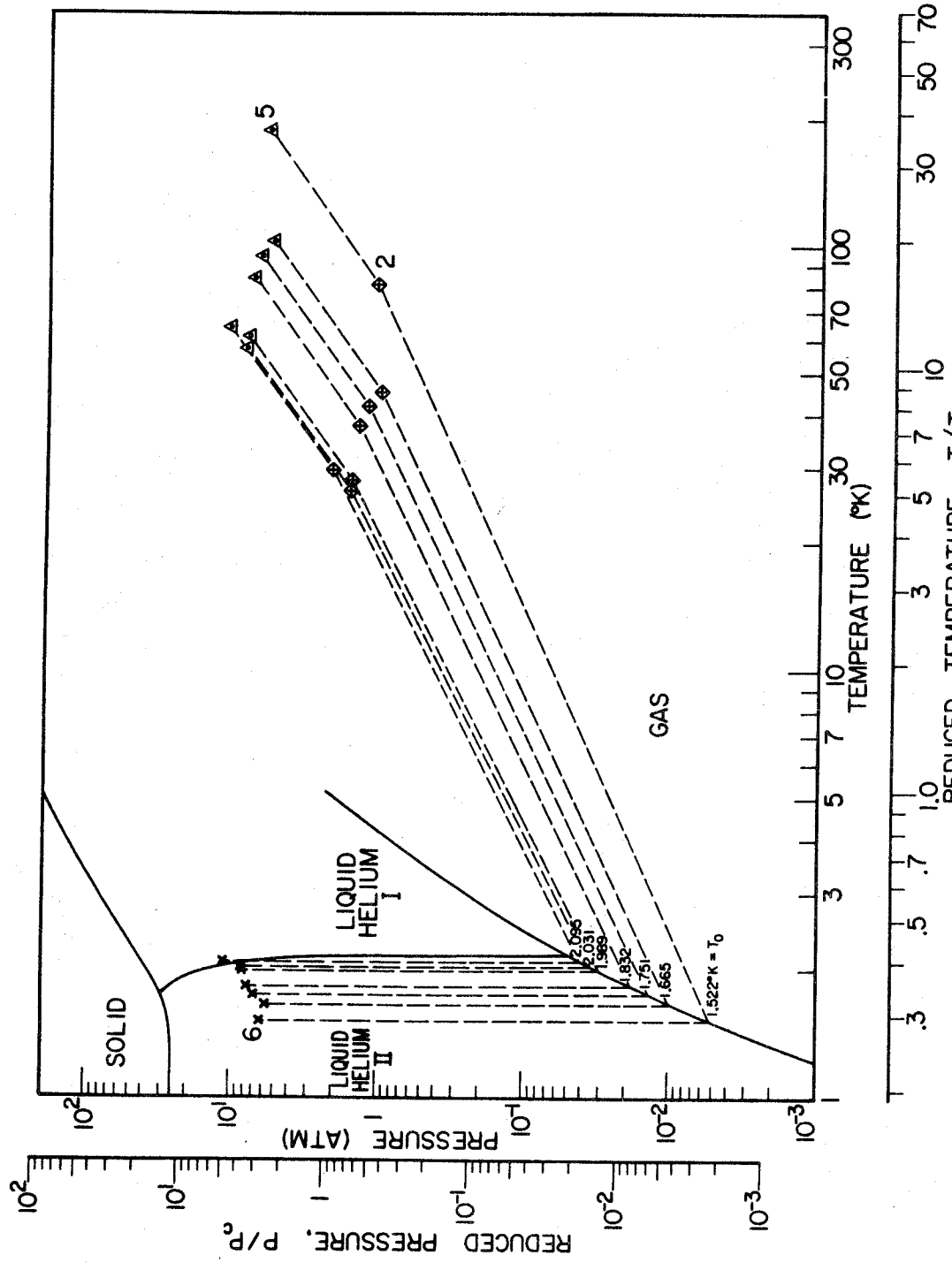

Figure 19. Calculated Fluid States in Regions 2, 5, & 6 of the Shock-Induced Flow Field

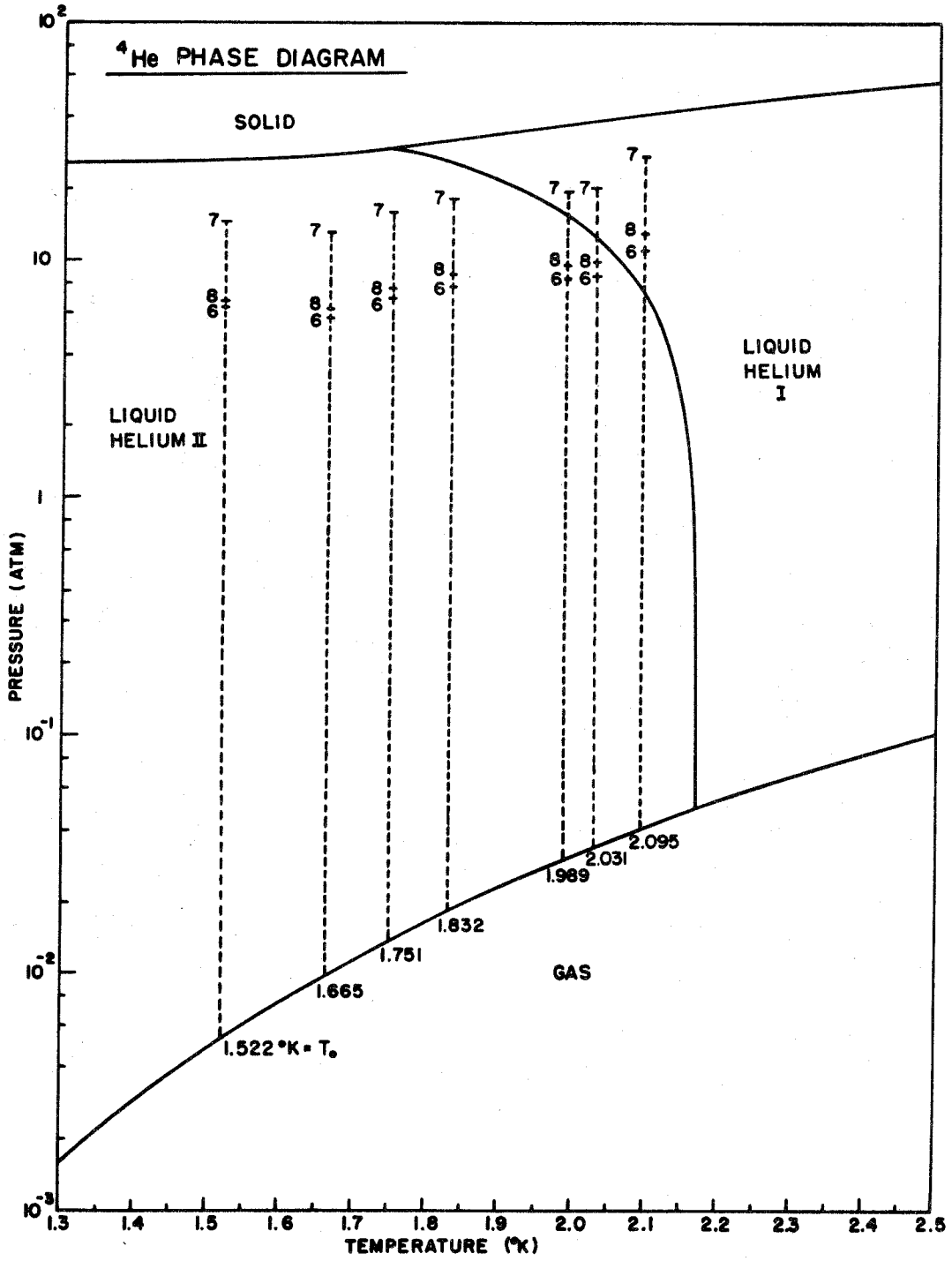

Figure 20. Calculated Liquid States in Regions 6, 7, & 8 of the Shock-Induced Flow Field

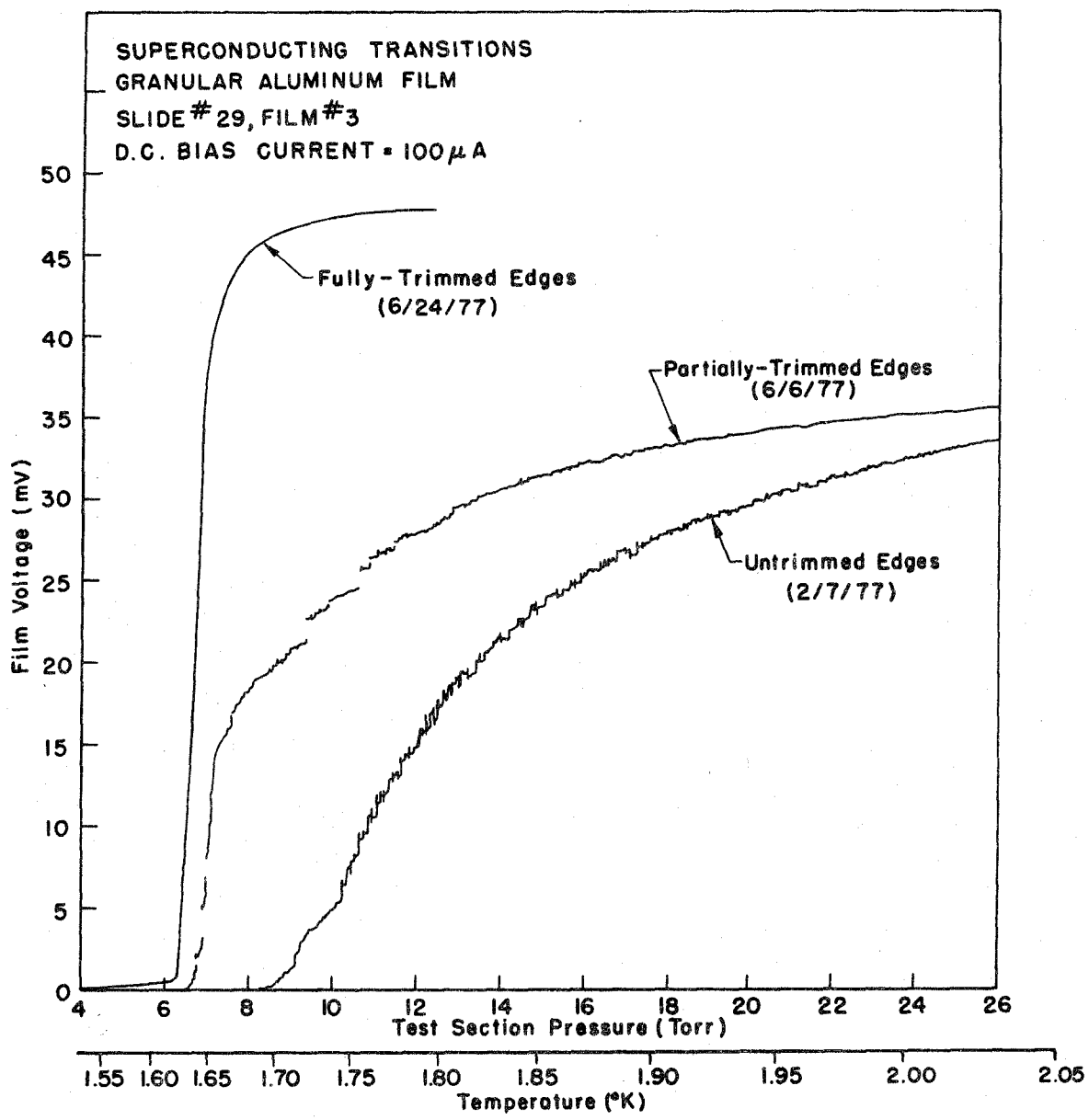

Figure 21. Effects of Edge Trimming on the Superconducting Transition of a Granular Aluminum Film

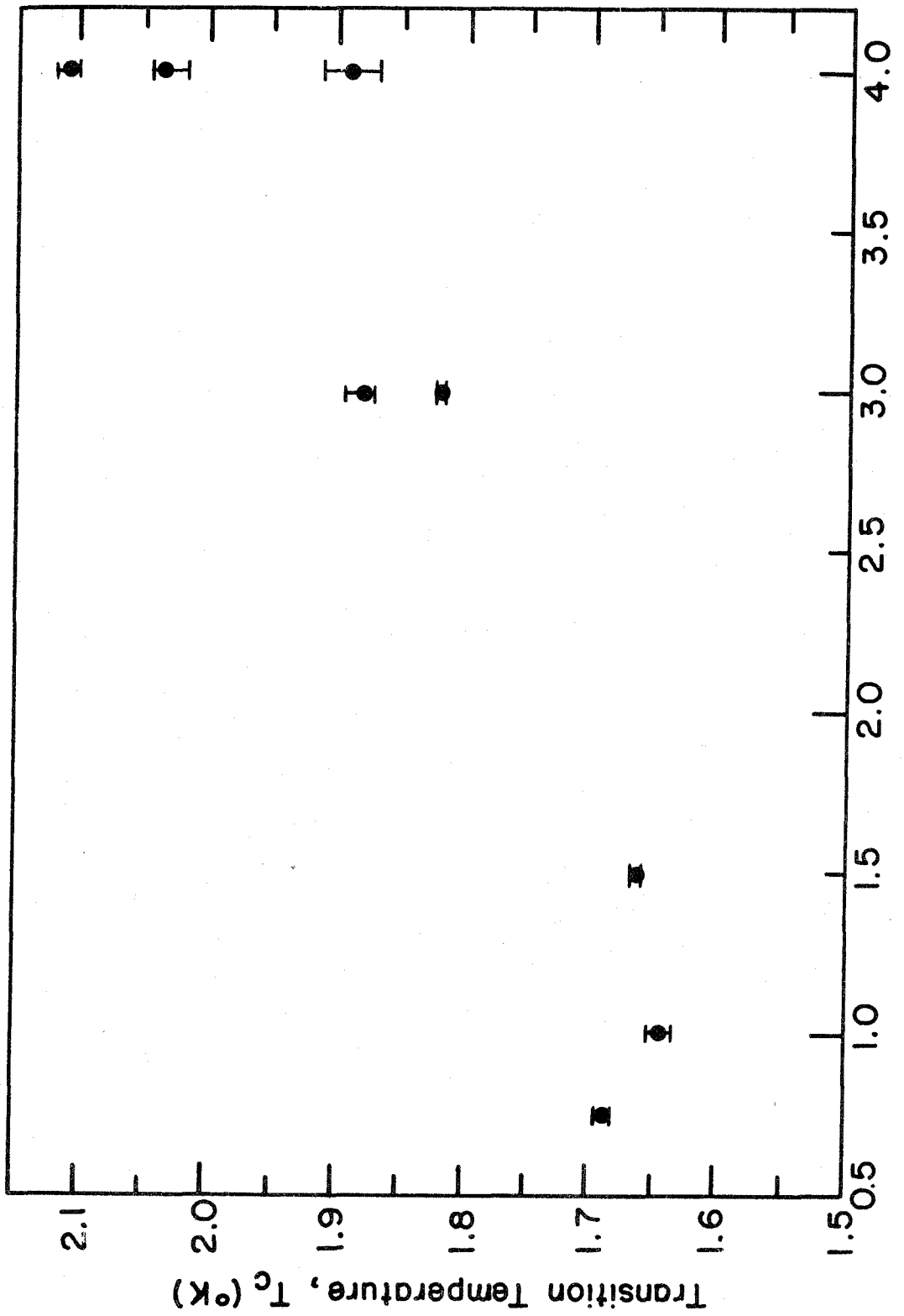

Figure 22. Influence of Initial Oxygen Pressure (during Evaporation) on Thin-Film Transition Temperatures

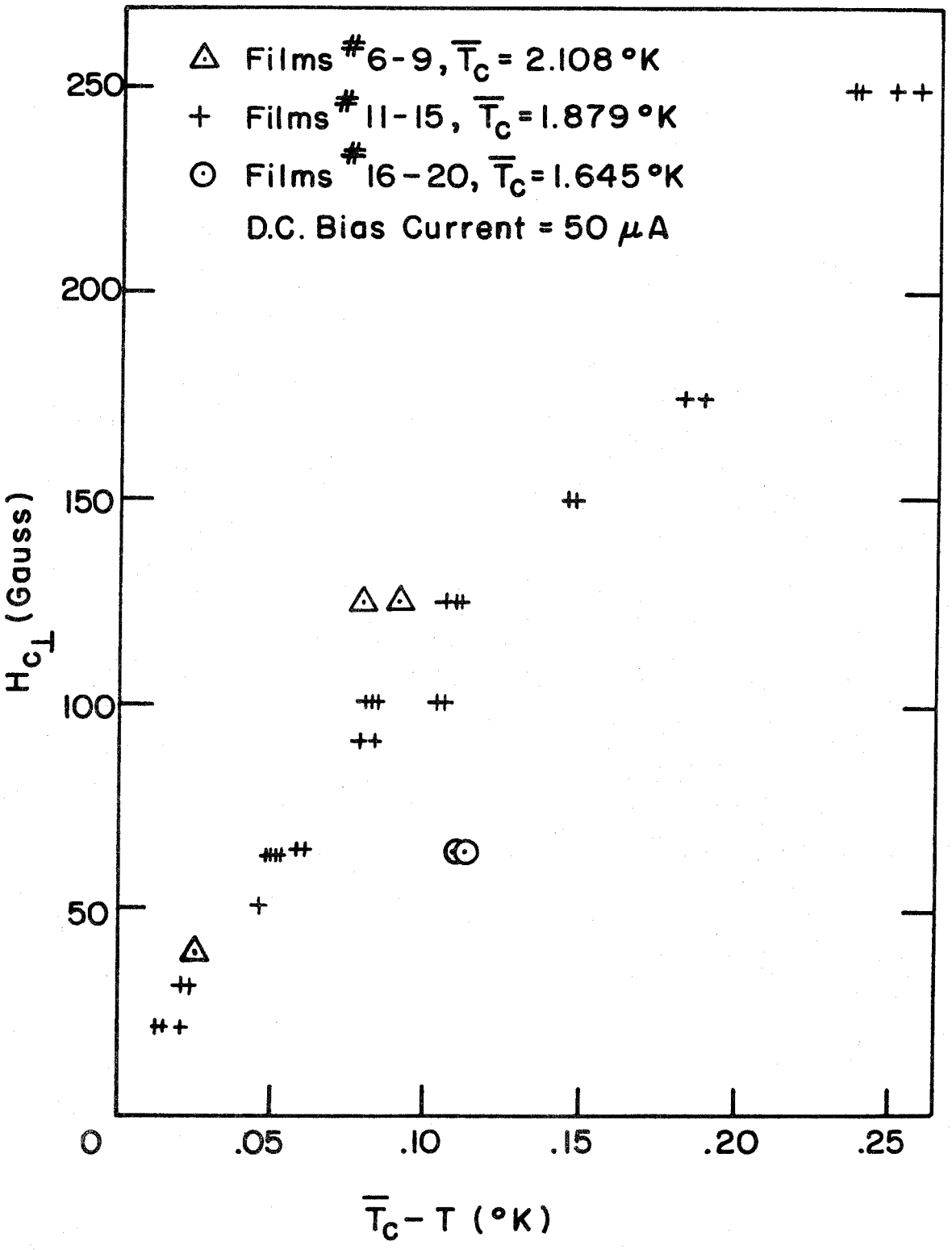

Figure 23. Variation of $H_{c_\perp}$ with Shift in Transition Temperature, $\overline{T}_c$ - T

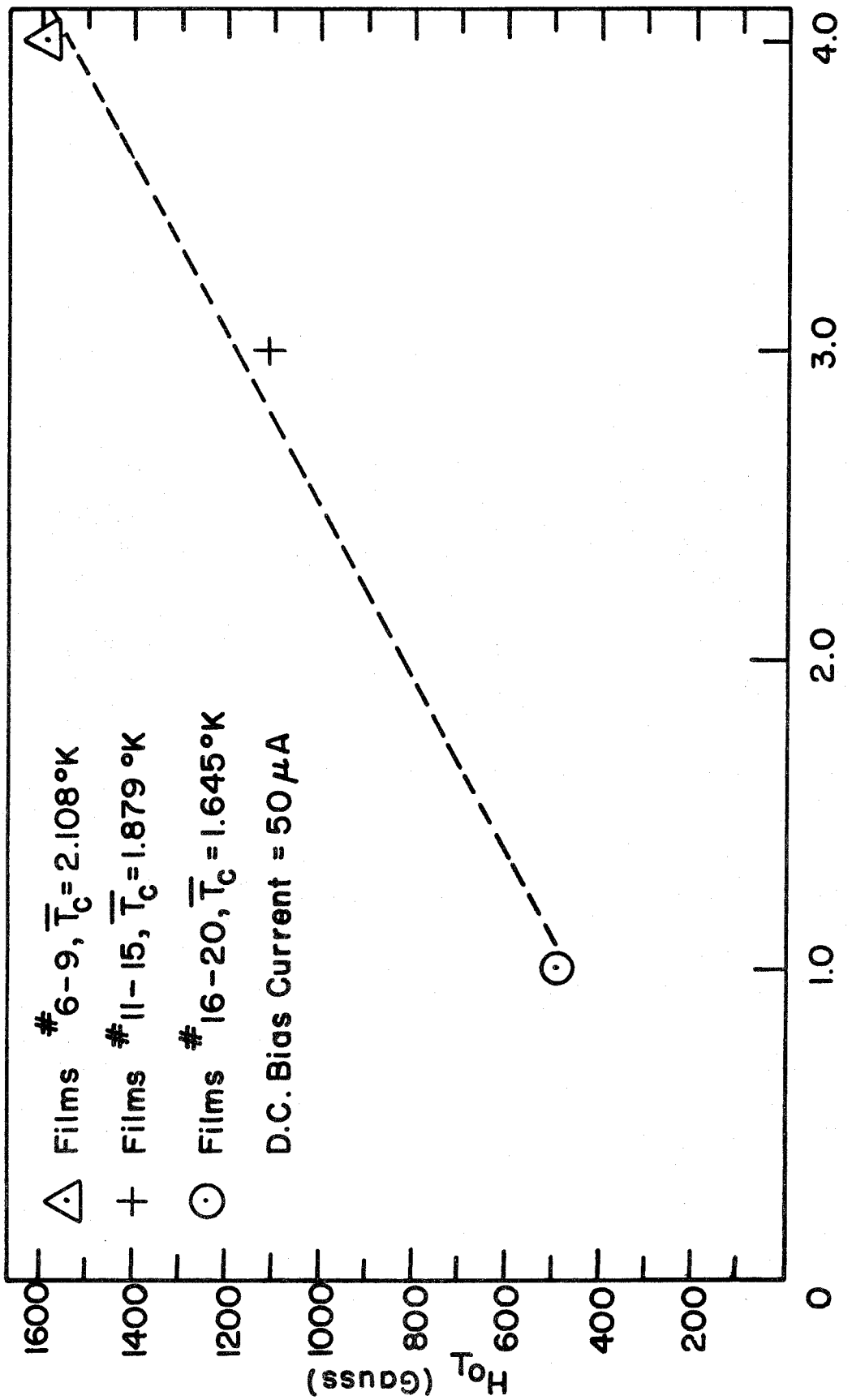

Figure 24. Influence of Initial Oxygen Pressure (during Evaporation) on H_{o_1} of Granular Aluminum Films

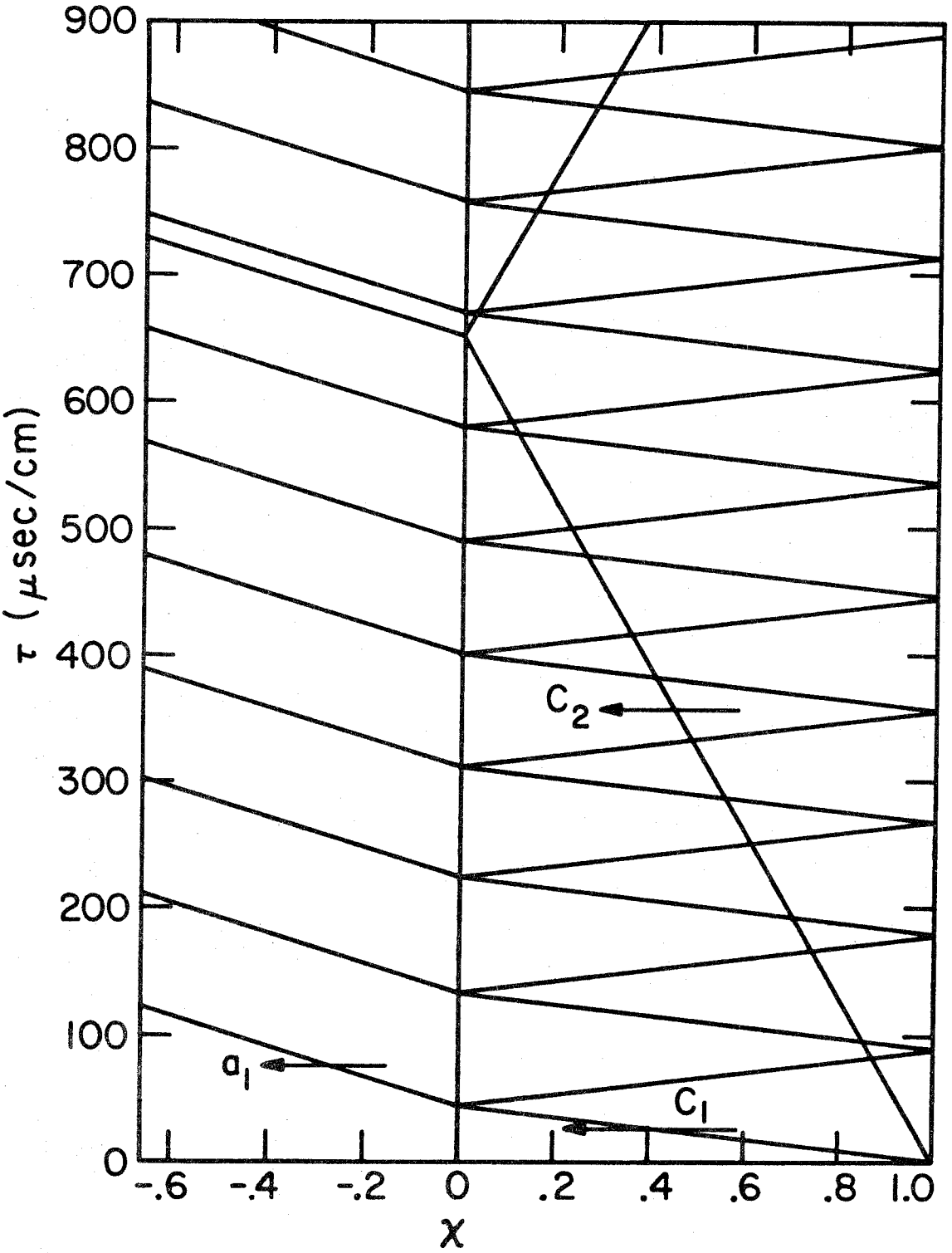

Figure 25. χ-τ Diagram for Heater-Generated Flow Field

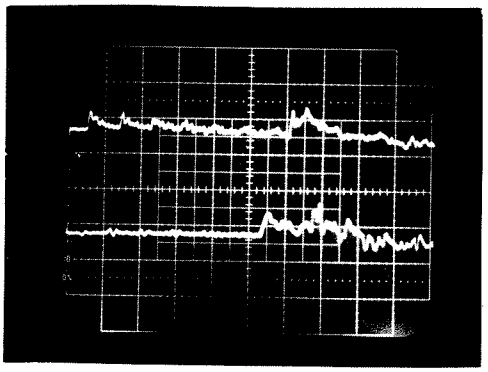

RUN 85

UPPER TRACE – FILM 1

$\chi = -.065$

LOWER TRACE – FILM 4

$\chi = +.116$

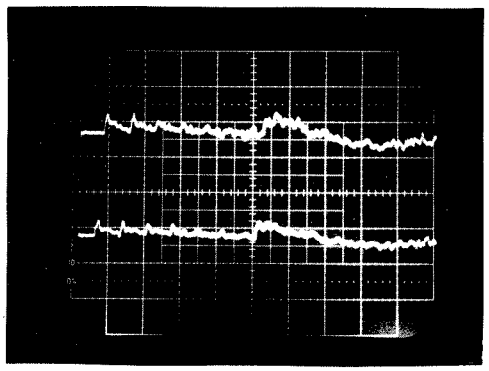

RUN 103

UPPER TRACE – FILM 1

$\chi = -.339$

LOWER TRACE – FILM 4

$\chi = -.112$

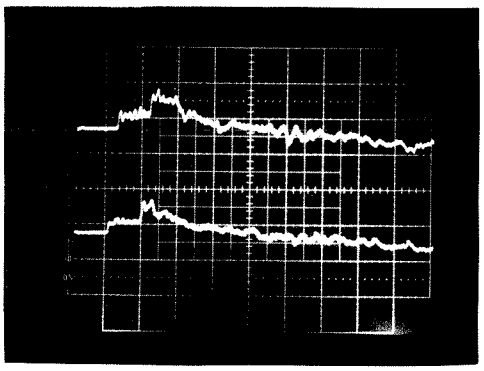

RUN 117

UPPER TRACE – FILM 1

$\chi = -5.20$

LOWER TRACE – FILM 4

$\chi = -4.15$

7/22/78; RUNS 85, 103, 117

$T_0 = 2.031°K$

.4 mV/div vertical; .5 msec div sweep

Figure 26. Detector Response to Heater-Generated Flow Field

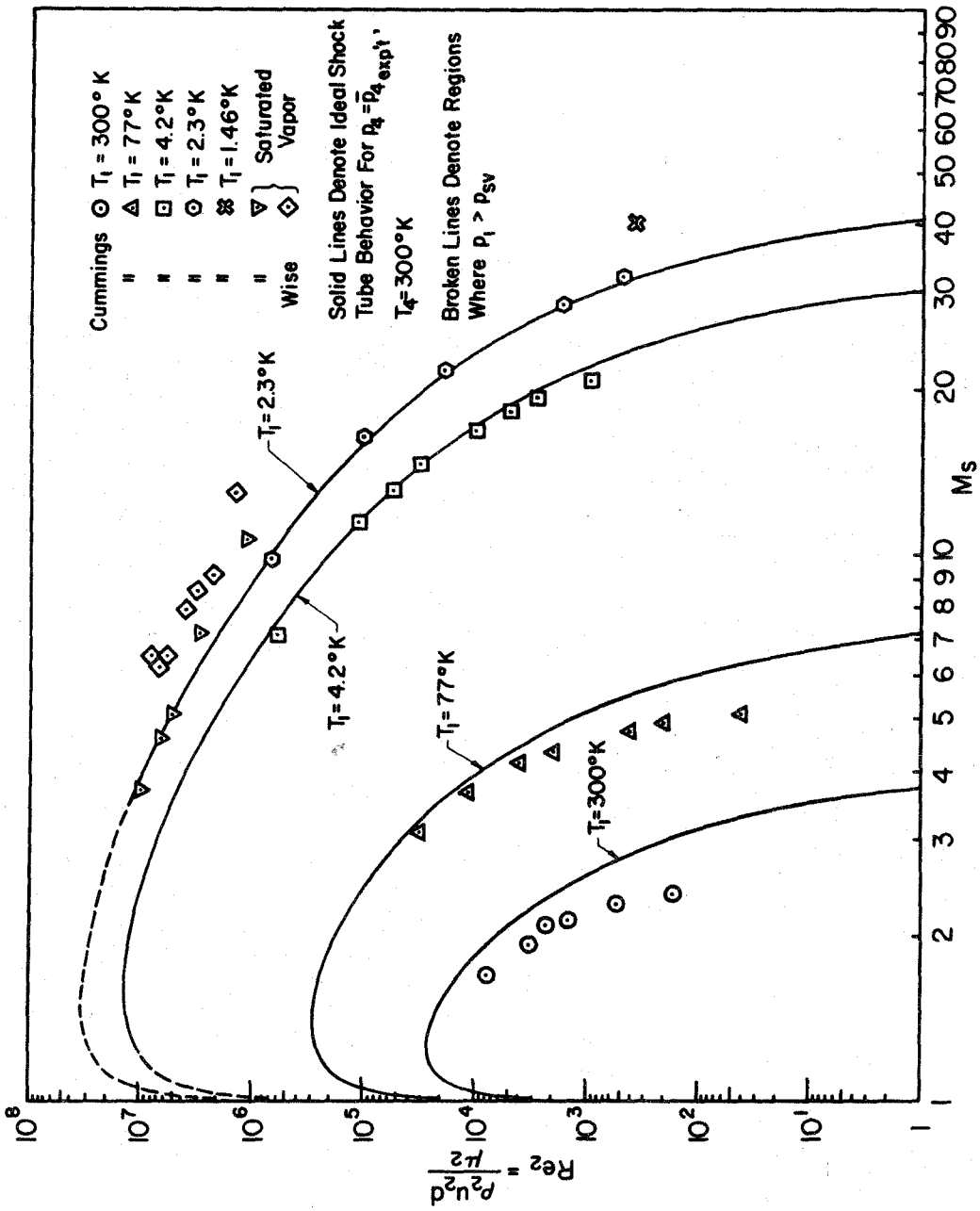
Cummings ⊙ T_1 = 300° K
" △ T_1 = 77° K
" □ T_1 = 4.2° K
" ⊙ T_1 = 2.3° K
" ⊠ T_1 = 1.46° K
Wise ▽ Saturated Vapor
◇
Solid Lines Denote Ideal Shock Tube Behavior For $p_4 = \bar{p}_{4_{exp't}}$
T_4 = 300° K
Broken Lines Denote Regions Where $p_1 > p_{sv}$
T_1 = 2.3° K
T_1 = 4.2° K
T_1 = 77° K
T_1 = 300° K
$Re_2 = \frac{\rho_2 u_2 d}{\mu_2}$
M_s
Re_2 vs M_s–CRYOGENIC SHOCK TUBE

Figure 27.

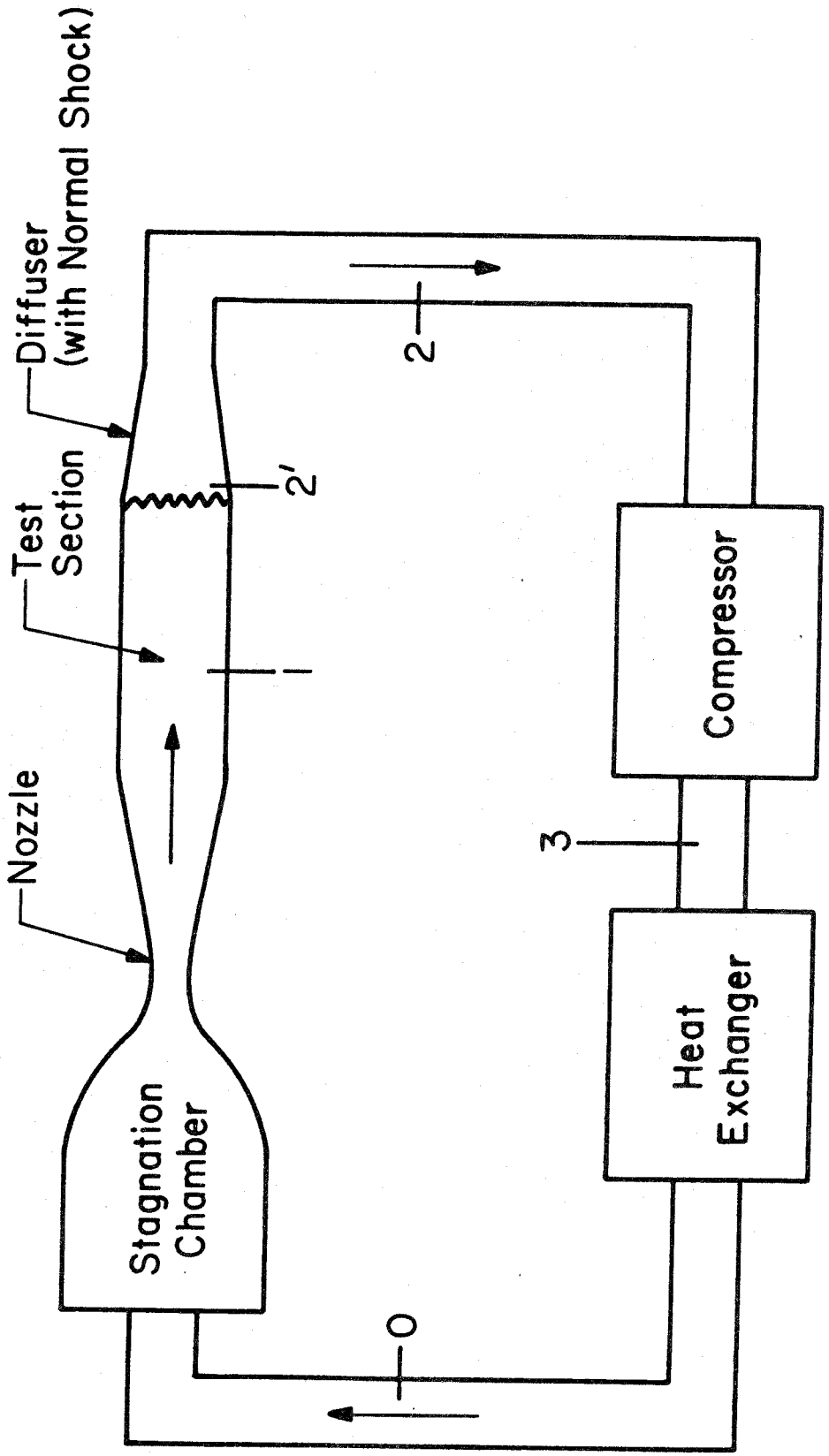

Closed-Circuit Liquid Helium Tunnel

Figure 28.

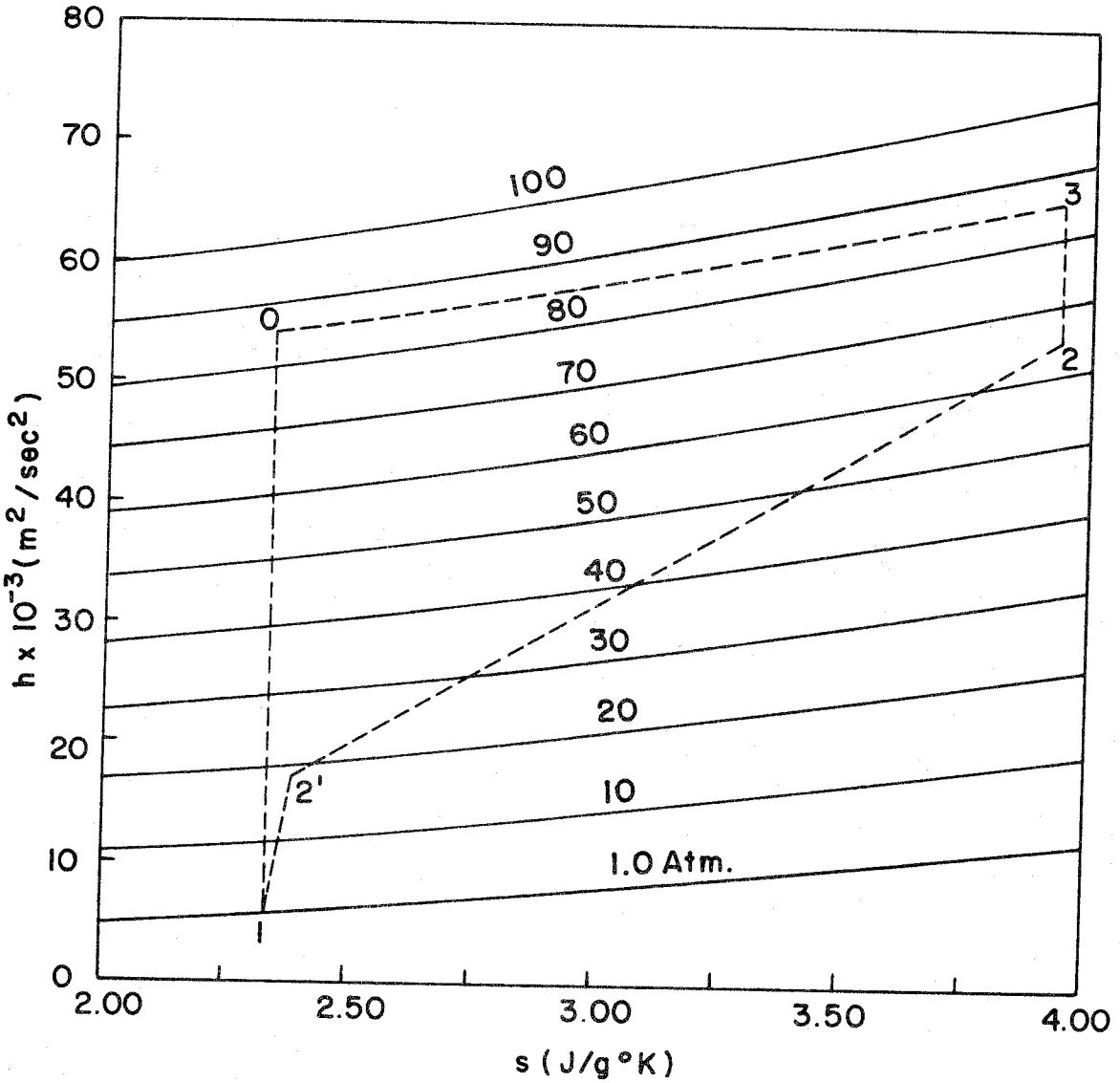

Figure 29. Working-Cycle Analysis for Liquid Helium Tunnel